Bottom-up grown InSb nanowire quantum devices

Document Version:
Publisher's PDF, also known as Version of Record (includes final page, issue and volume numbers)

Please check the document version of this publication:

• A submitted manuscript is the version of the article upon submission and before peer-review. There can be important differences between the submitted version and the official published version of record. People interested in the research are advised to contact the author for the final version of the publication, or visit the DOI to the publisher's website.
• The final author version and the galley proof are versions of the publication after peer review.
• The final published version features the final layout of the paper including the volume, issue and page numbers.

Link to publication

BOTTOM-UP GROWN INSB NANOWIRE QUANTUM DEVICES

SAŠA GAZIBEGOVIĆ

Bottom-up Grown InSb Nanowire Quantum Devices

Proefschrift

ter verkrijging van de graad van doctor aan de Technische Universiteit Eindhoven, op gezag van de rector magnificus prof.dr.ir. F.P.T. Baaijens, voor een commissie aangewezen door het College voor Promoties, in het openbaar te verdedigen op vrijdag 10 mei 2019 om 13:30 uur

door

Saša Gazibegović

geboren te Doboj, Bosnië en Herzegovina

Dit proefschrift is goedgekeurd door de promotoren en de samenstelling van de promotiecommissie is als volgt:

voorzitter: prof. dr. ir. G.M.W. Kroesen
1e promotor: prof. dr. E.P.A.M. Bakkers
copromotor: prof. dr. L.P. Kouwenhoven
leden: prof. dr. F. Roozeboom
                    dr. F.A. Zwanenburg (Universiteit Twente)
                    dr. habil. A. Fontcuberta i Morral (École polytechnique
                    fédérale de Lausanne)
                    prof. dr. N.A.J.M. Sommerdijk
                    prof. dr. C.J. Palmstrøm (University of California
                    Santa Barbara)

Het onderzoek of ontwerp dat in dit proefschrift wordt beschreven is uitgevoerd in overeenstemming met de TU/e Gedragscode Wetenschapsbeoefening.

Mom djedu Aliji.

Contents

1

Chapter

Introduction

1.1 The future of quantum computing

Can we imagine a world where new medical drugs are developed and existing ones become more efficient due to the accurate and fast modeling of billions of molecular interactions at an atomic level? Or that health management is advanced on nearly every level, from diagnosis to treatment? A situation where your data is ultra-protected by some sort of encryption and it cannot be viewed by anyone but the intended receiver? All of this, and much more will be possible with a revolutionary technology, quantum technology. Quantum technology relies on quantum-mechanical principles, such as superposition and entanglement, that would enable unprecedented computing power.

Today researchers spend years and years experimentally comparing the effects of different drugs on a number of diseases to determine the suitable medication. This process can be significantly shortened with quantum computers that have enough computational power to actually envision all possible outcomes. And that some sort of encryption is a quantum encryption, *i.e.*, cryptography, that exploits quantum phenomena to simply transmit a secret key secured over a distance by the fundamental laws of physics.[1] Quantum computing is believed to be the key to tackle important challenges of 21st century by being complementary to classical computing. Although the existing quantum computers are mostly still laboratory experiments we should not forget that just five decades ago the size of the computer was fitting a full room while today's 6-inch phones that fit in our pockets have a 1 trillion-fold increased computing power.[2]

The classical computer that we are using today is simply a calculator that employs sequences of bits, being in one of the two states "0" or "1", "true" or "false", "on" or "off", *etc.*, offered by high and low voltage states of millions of transistors. A quantum computer uses two states as well, two energy levels, however the difference to a classical computer is that it can also be in a superposition of the two energy levels. This quantum version of classical bit is called a qubit. The state of a single qubit is described by its wave function:

$$|\psi\rangle = \alpha |0\rangle + \beta |1\rangle \qquad\qquad (1.1)$$

where α and β are complex numbers representing the amplitude of the quantum state. The wave function consists of a superposition of many computations carried out simultaneously. Quantum computers are a hot topic in the research community today and companies such as Microsoft,[3] Google,[4] IBM,[5] Intel,[6] DWave,[7] IonQ,[8] Baidu,[9] Tencent,[10] Alibaba,[11] *etc.*, are developing different quantum technologies based on semiconductor-based platforms, superconducting circuits, adiabatic, spin states of coupled single-electron quantum dot and single atoms in ion traps. The biggest obstacles towards the realization of working quantum computer are noise and decoherence.[12-14] Decoherence represents undesired interactions between the computer's qubits and the environment. Examples of decoherence are light, sound, vibrations, heat, *etc.*, or even the act of measuring the qubit. Due to the decoherence qubits are fragile and their ability to stay in superposition and/or entanglement is

jeopardized. Decoherence leads to multiple errors in process of quantum computation, hence the information is lost.

To allow for successful quantum computation the qubit should be robust, have a long enough coherence time to run and evolve a calculation of the quantum states.

1.2 Topological quantum computer

An example of more robust quantum hardware employs a topological qubit. The work in this thesis focuses on topological quantum computing where the decoherence issue is avoided by employing non-Abelian state of matter.[14] A topological quantum computation allows for quantum information to be stored and manipulated nonlocally. The elementary particles of a non-Abelian system may appear in a specifically designed condensed matter system, *i.e.*, a topological superconductor, and those particles are known as Majorana quasiparticles. A unique property of these Majorana quasiparticles is that they are their own anti-particles.[15] The central part of the Majorana device is a proximitized quantum nanowire (see Chapter 2 for details on Majorana device).

1.3 Bottom-up grown one-dimensional nanowires

One-dimensional (1D) system, referred to as a quantum nanowire, is a mesoscopic system which allows for one-directional particle motion, usually electrons or holes, but quantization of the particle motion in the transverse direction leads to quantized values of the conductance. Quantum nanowires are unique due to their dimensions which include the large surface area, one-dimensional density of states (DOS), diameter-dependent bandgap, and increased surface scattering for electrons and phonons, significantly different compared to those of their bulk 3D counterparts. The nature of a 1D system depends on the effective electron (hole) mass and is consequently material dependent. In order to be able to explore the 1D electronic nature of nanowires, they have to meet a number of requirements. Most important parameters are:

- Aspect ratio, which is determined by the diameter and the length. Practically, one needs a certain minimum length of the wires to accommodate ohmic contacts and gates, *etc.*, for the final device. The diameter determines the energy spacing between the subbands, and therefore the number of subbands that can be populated by electrons at a given temperature. This level spacing is determined by the effective mass of the charge carrier. *E.g.*, for an InSb nanowire with a diameter of 70 nm a subband level splitting of 16 meV has been observed.[16]

- Carrier scattering probability (elastic and inelastic) determines the mean free path (ballistic), carrier mobility, and coherence length (inelastic). Scattering is affected by crystal quality, impurity level and surface passivation. Generally,

for most quantum devices a defect-free crystalline phase is preferred for coherent and ballistic transport, and for some systems it is important to induce lattice strain in a controllable way. Lattice strain can affect the electronic band structure of a semiconductor, such as the bandgap energy and carrier mobilities. Strain can be exerted in a core-shell geometry. A core-shell geometry can also be used to passivate the large surface area of a 1D system, and therefore reduce detrimental effects of surface states.

- Carrier density and impurity doping. For many devices, the few-carrier regime is most important. To be able to reach theoretically predicted mesoscopic properties of 1D system it is important to control the impurity doping of this system. Normally, impurities are undesired unless the dopants are the active quantum components.

The possibility to fabricate and synthesize high-quality 1D nanomaterials with the desired size, thickness, composition, crystal phase, *etc.*, is an important factor that allows access to the unique electronic and quantum properties of these nanomaterials. There are generally two approaches to fabricate 1D semiconductors: top-down and bottom-up. The top-down fabrication method starts with a bulk substrate, from which the designed structures are carved out by various lithography and etching steps. The second fabrication route follows the bottom-up approach, where structures are assembled using atoms or molecules as building blocks. Compared to the top-down fabrication method, nanostructures are fabricated here without using many advanced lithography steps. Bottom-up is a fabrication method in which atoms and molecules are used to build up the desired nanostructures with few defects, homogenous chemical composition, and large aspect ratio. There are different concepts which refer to the bottom-up fabrication of nanowires, most applied ones are metal-catalyst assisted vapor-liquid-solid (VLS) and vapor-solid-solid (VSS), selective area growth (SAG) and the cleave edge overgrowth (CEO). Within these concepts, different epitaxial growth methods, such as chemical vapor epitaxy (CVD), metal-organic vapor phase epitaxy (MOVPE), chemical beam epitaxy (CBE), molecular beam epitaxy (MBE), *etc.*, can be used for the synthesis of the crystalline 1D nanomaterials. In this thesis MOVPE and MBE are used for the bottom-up growth of 1D Majorana device.

1.4 Outline of the thesis

In this thesis the bottom-up growth of Majorana nanowire devices, made of indium antimonide, is perfected, which is the core of the realization of a topological quantum computer.

The outline of this thesis is as follows:
Chapter 2 introduces the theoretical background relevant for the work discussed in the experimental chapters Chapter 4-7.

Chapter 3 outlines the methods for the growth, functional characterization and device fabrication of the Majorana nanowire.

In the first experiments reported here in **Chapter 4,** we developed a new substrate platform for the growth of complex nanowire networks based on InSb nanowires. The high quality of a "hashtag" nanowire is demonstrated by the Aharonov-Bohm experiment. The substrate platform developed here is generic and can also be used to grow nanowire networks made of different materials.

Next, in **Chapter 5**, we use these network substrates to deterministically shadow-grow superconducting islands on InSb nanowires creating *in-situ* Majorana devices. We explore the device stability by preforming *in-situ* TEM analysis at elevated temperatures. In these devices the characteristic Majorana signatures are observed.

In **Chapter 6** we eliminate the main bottleneck for the growth of InSb nanowires and grow chemically pure nanowires with high aspect ratios. We report the highest observed electron mobility for bottom-up grown nanowires.

Following a similar growth approach we investigated the growth of two-dimensional "free-standing" nanoflake structures in **Chapter 7**. By varying the *ex-situ* and *in-situ* parameters we are able to tune the growth from nanowires to almost fully nanoflakes on the substrate.

Chapter 8 shares the outlook and perspective of material development for topological quantum computation.

1.5 References

1   Ladd, T. D. *et al.* Quantum computers. *Nature* **464**, 45, doi:10.1038/nature08812 (2010).

2   Experts Exchange. *Processing power compared*, https://pages.experts-exchange.com/processing-power-compared.

3   Microsoft.   *Microsoft   Quantum: Research*,   https://www.microsoft.com/en-us/research/lab/quantum/.

4   Google. *Quantum - Google AI*, https://ai.google/research/teams/applied-science/quantum-ai/

5   IBM. *IBM Q,* <https://www.research.ibm.com/ibm-q/

6   Intel. *Quantum Computing*, https://newsroom.intel.com/press-kits/quantum-computing/

7   DWave. *DWave The Quantum Computing Company*, https://www.dwavesys.com/

8   IONQ. *A true quantum leap*, https://ionq.co/?/home

9   Baidu Research. http://research.baidu.com/Index

10   Tencent. https://www.tencent.com/en-us/

11   Alibaba Group. *Aliyun and Chinese Academy of Sciences Sign MoU for Quantum Computing Laboratory*, https://www.alibabagroup.com/en/news/article?news=p150730

12   DiVincenzo,   D.   P.   Quantum   Computation.   *Science*   **270**,   255-261, doi:10.1126/science.270.5234.255 (1995).

13   Stern, A. Non-Abelian states of matter. *Nature* **464**, 187, doi:10.1038/nature08915 (2010).

14   Stern, A. & Lindner, N. H. Topological Quantum Computation—From Basic Concepts to First Experiments. *Science* **339**, 1179, doi:10.1126/science.1231473 (2013).

15   Majorana, E. & Maiani, L. in *Ettore Majorana Scientific Papers: On occasion of the centenary of his birth* (ed Giuseppe Franco Bassani) 201-233 (Springer Berlin Heidelberg, 2006).

16   Kammhuber, J. *et al.* Conductance Quantization at Zero Magnetic Field in InSb Nanowires. *Nano Letters* **16**, 3482-3486, doi:10.1021/acs.nanolett.6b00051 (2016).

2

Chapter

Theory: Majorana nanowire
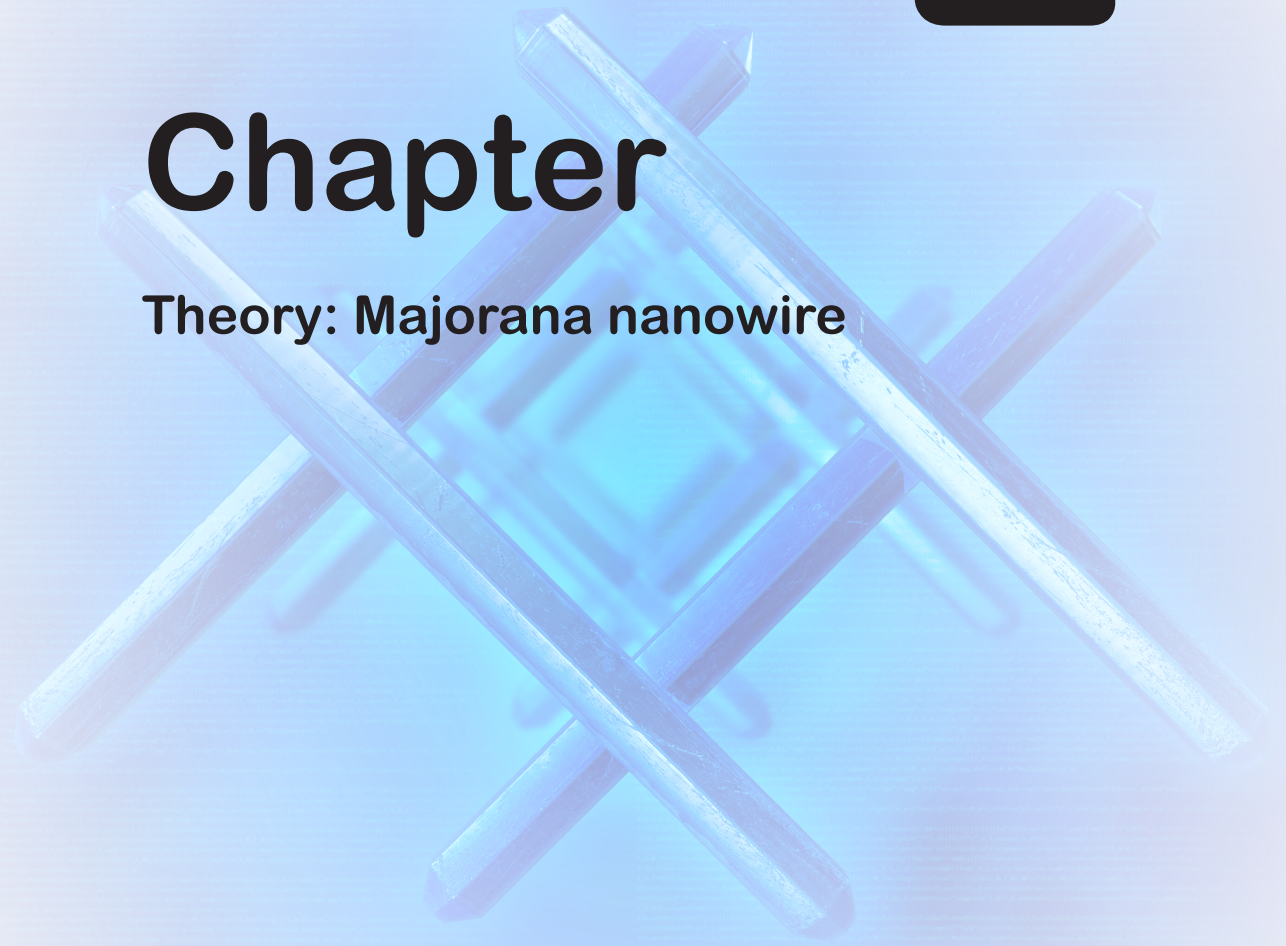
Abstract *For almost a decade, the search for Majoranas in condensed matter has become one of the hottest topics in physics. The scientific journey is progressing with united work of theoreticians, experimentalists and materials scientists. The aim of this chapter is to provide a brief introduction to the basic ingredients needed for realizing Majorana zero modes (MZM) and single qubit devices with a strong focus on materials. An experimental method for the detection of Majoranas in a semiconductor nanowire device using tunneling spectroscopy is proposed. After a short introduction to the requirements of Majorana and qubit devices an explanation for crystal growth of materials, namely vapor-liquid-solid (VLS) grown nanowires and epitaxial growth of thin films, is given. The core of the realization of a topological quantum computer lays in the material science, i.e., thoughtful choice and growth methods of quantum materials.*

2.1 Quantum devices

The revolution of quantum physics had only just started with the work of physicists such as Max Planck, Albert Einstein, Erwin Schrödinger, and Werner Heisenberg when in 1937 the Italian physicist Ettore Majorana proposed the existence of a particle today known as the Majorana quasiparticle. After decades of searching a way to prove the existence of Majorana particles, only recently the focus is moved to the field of condensed matter physics. The major breakthrough is to be realized by specially engineering low-dimensional materials, quantum materials, that would give out the Majoranas, as proposed by Alexei Kitaev.[1] And the key of the experiment, quantum materials, can be defined as materials whose exotic physical properties arise from the quantum mechanical properties of their electrons.[2]

It was only in 2010 when the "recipe" for detection of Majorana particle , as we follow today, was suggested.[3,4] The key element to realize a Majorana device was realizing a one-dimensional spinless p-wave superconductor.[5] Spinless superconductivity arises when a one-dimensional semiconductor nanowire with strong Rashba spin-orbit interaction is in close proximity (coupled) to a normal, s-wave superconductor. The more intuitive and explanatory information is given in Figure 2.1a-b where the energy spectrum of a nanowire with strong spin-orbit coupling is illustrated. Strong spin–orbit coupling splits the otherwise spin-degenerate parabolic bands shifting each by momentum $\pm k_{SO}$ in k-axis and introduces a new energy scale, E_{SO} (Figure 2.1a). The momentum and energy are given by:

$$k_{SO} = m^* \alpha_R / \hbar^2 \qquad\qquad (2.1)$$

$$E_{SO} = m^* \alpha_R^2 / 2\hbar^2 \qquad\qquad (2.2)$$

where m^* is the effective mass of the semiconductor (nanowire) material, α_R the Rashba spin–orbit term with the coupling strength and $\hbar$ Planck's constant. In this situation electron transport is maintained by two electronic subbands with opposite spins. To reach the spinless regime, an external magnetic field (B) perpendicular to the direction of the Rashba spin-orbit coupling axis is applied, Figure 2.1b. The subbands are now split in energy. The energy gap is created at zero momentum (k = 0), and the Zeeman energy term (E_Z) arises. With $E_Z = g\mu_B B/2$, where g is the

2

Landé g-factor and μ_B Bohr magneton. The electron spin orientation is locked to the direction of momentum. If the Fermi level is tuned to be within the gap, ($|\mu| < |E_Z|$) electron transport is maintained by two electronic subbands with single spin. In other words, the spin degree of freedom is locked to the momentum in which there is only a single possible spin direction for each energy value. This regime is often associated with the word "helical".

If the nanowire is proximitized by an s-wave superconductor (illustrated in Figure 2.2a), meaning that Cooper pairs from the superconductor can tunnel into a nanowire and induce superconductivity, another parameter to take into account is Δ_0, an induced pairing potential in the nanowire. Now, the interplay between the key parameters spin-orbit coupling, Zeeman effect and superconductor pairing plays the main role on the emergence of topological superconductivity. For the chemical potential μ inside the Zeeman gap, the system undergoes a topological phase transition with the strict requirement that:

$$E_Z > \sqrt{\mu^2 + \Delta_0^2} \qquad (2.3)$$

The conclusion that can be derived from here is that the proximitized nanowire can be driven into a topological phase experimentally by tuning the magnetic field (introducing Zeeman energy) and the chemical potential.[5]
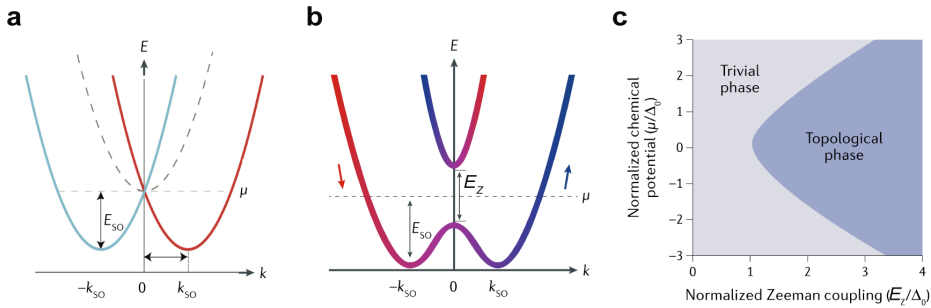
Figure 2.1 | Electronic bands of a one-dimensional nanowire with Rashba spin-orbit coupling without and with applied external magnetic field and topological phase transition diagram. Energy spectrum as function of the momentum, k, along the nanowire showing: **a,** At zero magnetic field, $B = 0$, spin-orbit coupling splits (shifts) the parabolas sideways by k_{so} and introduces a new energy scale E_{so} shifted by $-E_{so}$. The grey dashed parabola corresponds to the case without spin-orbit coupling. **b,** At an applied external magnetic field perpendicular to the direction of the Rashba spin-orbit coupling axis, Zeeman energy (coupling) V_Z is introduced and opens an energy gap at $k = 0$. Arrows (red and blue) indicate the approximate spin orientation for different momentum. The chemical potential, μ, is defined in the middle of the Zeeman gap. **c,** Topological quantum phase diagram. By changing μ in the nanowire or Zeeman splitting E_Z one can drive the system into a topological phase. Here Δ_0 is the induced pairing potential (strength) in the nanowire. Adapted from References 5 and 6.

For large applied B and considering Equation (2.3), Majorana states can emerge at the ends of the proximitized nanowire at the point where the trivial superconducting gap closes and a topological gap re-opens.[7] This phenomenon corresponds to a

topological quantum phase transition, *i.e.*, a quantum phase transition between topologically trivial and non-trivial states, see Figure 2.1c.[5]

2.1.1 Nanowire Majorana device and detection

In the introduction of this section the ingredients for realizing Majoranas are given. They particularly include: a one-dimensional nanowire with strong Rashba spin-orbit interactions with proximity induced superconductivity placed in the magnetic field. A device for the detection of a Majorana can be engineered in the lab, where appropriate selection of the nanowire and superconductor material is essential. So far, the heavy-element semiconductors InAs and InSb have received much attention due to their material properties owning strong spin-orbit coupling as well as large Landé *g*-factor, whereas NbTiN and Al have been primarily used for the superconducting components.[5] The quantum materials are discussed in the Section 2.2 of this chapter.
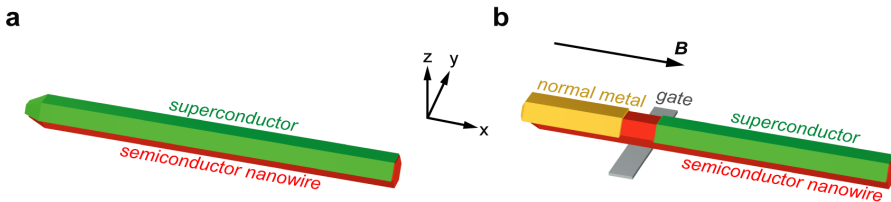
Figure 2.2 | A semiconductor-superconductor nanowire and a Majorana device. a, Schematic illustration of a semiconductor nanowire that meets the requirements for a Majorana nanowire device. Nanowire with strong-spin orbit interaction (red) coupled to a s-wave superconductor (green) on only two facets of the nanowire. **b,** The Majorana nanowire from **a** was fabricated and contacted by a normal contact (yellow) leaving a gap between normal and superconducting contact uncovered. The non-covered part of the wire is capacitively coupled to a gate electrode which, for negative gate voltages, depletes the section between the contacts forming an electrostatically defined tunnel barrier. The conductance experiment through the nanowire, measured using both contacts, resolves the quasiparticle (excitation) density of states in the proximitized nanowire when a magnetic field (*B*) is applied along the *x*-axis. The Rashba spin-orbit coupling is assumed to be along the *y*-axis. Adapted from Reference 8.

To detect Majoranas, a semiconductor nanowire is contacted with a normal metal contact and a superconducting contact as illustrated on Figure 2.2b. The purpose of the normal metal contact is to detect a Majorana. The narrow separation between the two contacts on the nanowire is reserved for the gate that is used to introduce a tunneling barrier in the nanowire. A tunneling spectroscopy measurement is performed by sending a current to the superconductor through a tunnel barrier while applying a magnetic field along the nanowire. A Majorana state is expected to appear at the barrier on the edge of the superconducting contact. The Majorana is detected as a zero-energy state in the otherwise gapped excitation spectrum, referred to as a zero bias peak (ZBP). At the same time, a resonant Andreev reflection takes place where an incident electron is always Andreev reflected into a hole with unit transmission probability, Figure 2.3a. As a result, the measured conductance (*G*)

shows a universal quantized peak at a value of $2e^2/h$ (where e is the charge of an electron and h is the Planck constant), Figure 2.3c. The schematic of the transport characteristics of the tunneling spectroscopy measurement of a proximitized nanowire is given in Figure 2.3.
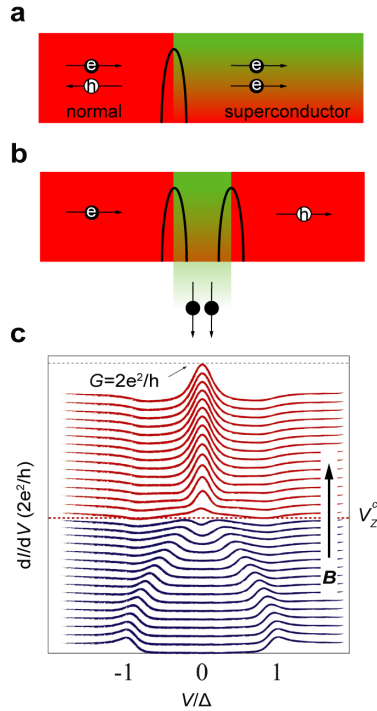
Figure 2.3 | Tunneling spectroscopy experiment in a Majorana device. Transport characteristics of Majorana normal semiconductor-superconductor junctions. **a,** Schematic of Andreev reflection in a normal semiconductor-superconductor junction: an incident electron is transformed into a hole and a Cooper pair is created in the superconductor. **b,** If the junction contains a Majorana bound state, Andreev reflection can be understood as a resonant process at zero energy through a "two lead" double barrier system where the original normal lead is separated into two "electron" and "hole" leads. **c,** Sketch of the tunnel spectroscopy measurement and behavior of differential conductance curves dI/dV as a function of bias voltage for increasing magnetic fields, B. Blue and red curves denote trivial and non-trivial regions, respectively. The topological transition is seen as a closing of the superconducting gap at the critical Zeeman field, E_Z^c, and the Majorana can be detected as a localized state at zero bias (energy) referred to as zero bias peak (ZBP). The ZBP should reach the universal quantized conductance value of $2e^2/h$. The experiment is performed at low (mK) temperatures. Adapted from Reference 6.

Shortly after the recipe has been suggested, Majorana devices were engineered in the lab. Subsequently, the first signatures of Majoranas (often referred to as Majorana zero modes, MZM) have indeed been detected as ZBPs in the tunneling spectroscopy measurements of a superconductor-semiconducting NbTiN-InSb nanowire device.[9] The experiment is outlined in Figure 2.4.
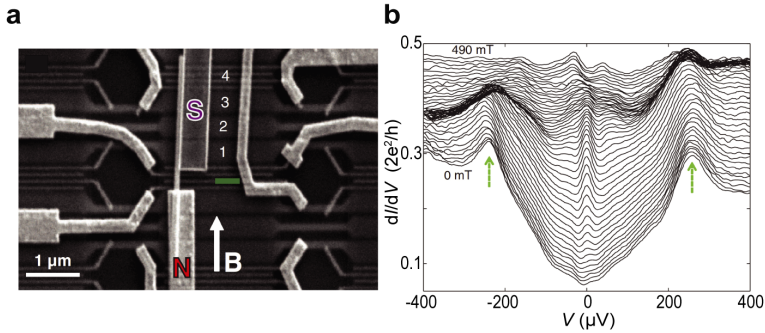
Figure 2.4 | **Tunneling spectroscopy measurement in NbTiN-InSb nanowire. a,** Scanning electron microscopy image of a device with normal (N) and superconducting (S) contacts covering an InSb nanowire. The S contact only covers the right part of the nanowire. The underlying gates, numbered 1 to 4, are used to deplete the wire. The tunnel barrier between normal and superconducting contacts is marked by a green line. **b,** Differential conductance (dI/dV) versus bias voltage (V) taken at different magnetic fields (B) along the nanowire axis (from 0 to 490 mT in 10 mT steps). For B fields between 100 and 400 mT, a clear ZBP at zero voltage emerges in the middle of the superconducting gap. Green arrows indicate the induced gap peaks. Adapted from References 6,9.

The ZBP was reported by several other groups using superconductor-semiconducting nanowire devices.[10-13] However, the features observed did not completely agree with the behavior predicted by Lutchyn and Oreg.[3,4] The most critical (distinct) were: the induced soft superconducting gap, and the ZBP not reaching the universal quantized conductance value of $2e^2/h$. Those were sufficient to lead to the big question in the field, verity of a "smoking gun" evidence for Majoranas. The main reason behind the induced soft superconducting gap is the significant density of states within the gap suggesting disorder (inhomogeneity) at the interface between the superconductor and the semiconductor nanowire. Access to topological properties in a Majorana device can be attained only by a homogeneous and disorder-free interface, resulting in a hard superconducting gap. Furthermore, disorder poses a prime challenge for these experiments, because it can mimic the zero-energy signatures of Majoranas and/or suppress the p-wave superconductivity, hence degenerate the topological phase. Following this knowledge, the experiments continued in a similar fashion focusing on the fabrication of Majorana devices with improved interfaces. The result of such an experiment are presented in Figure 2.5 where the surface of the InSb nanowire with native oxides was carefully treated (passivated) to avoid damaging the nanowire surface prior to the deposition of the NbTiN superconductor.[14-16] In this work, the disorder caused by the interface has been reduced and an induced hard superconducting gap has been observed. These experiments indicate that topological superconductivity by means of the proximity effect can be achieved. However, variation from device to device was observed and the ZBP height was, still, lower than the universal quantized conductance value.

2
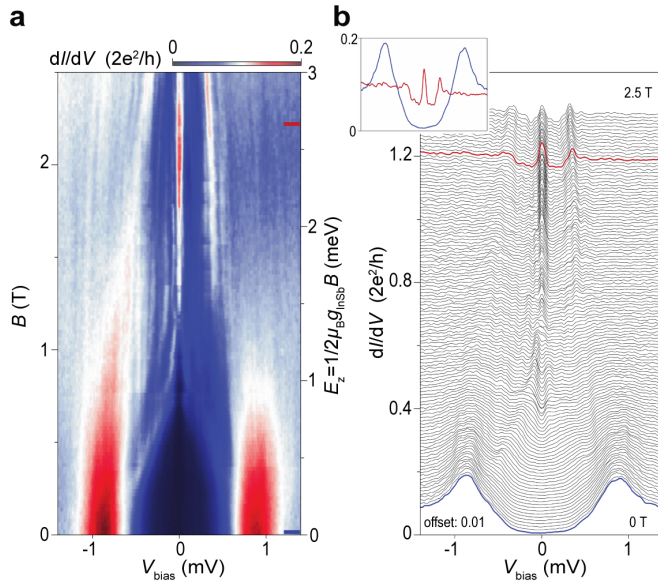
Figure 2.5 | Zero bias peak in ballistic NbTiN-InSb nanowire. a, Differential conductance (dI/dV) as a function of bias voltage (V_{bias}) and magnetic fields (B). An induced superconducting gap is present at zero magnetic field ($\Delta = 0.9$ meV). For increased B the gap closes at ~ 1 T, and a clear ZBP at zero bias voltage emerges and persists up to 2.5 T. **b,** Line cuts from **a** with $0.01 \times 2e^2/h$ offset. Inset: line cuts marked by a blue and red line in **a** and **b,** showing hard induced superconducting gap and ZBP reaching $0.1 \times 2e^2/h$, respectively. Adapted from Reference 14.

Elimination of possible disorder is an important step towards realizing a topological quantum computer, built out of multiple Majorana devices coupled to each other, because it poses a challenge in large scale operations. The disorder issue in the field is the great challenge and it introduces an important task for material scientists. To overcome this problem, a new method, *in-situ* epitaxial growth of hybrid superconductor-semiconductor nanowires, is explored (Chapter 5).

2.1.2 Braiding devices

One step closer towards topological quantum computing is demonstrating the non-local potential of Majoranas – key elements of topological quantum computing – fully, by exchanging them in a well-controlled braiding operation. Such braiding experiments are the ultimate proof of topologically protected Majoranas. The braiding operation needs to be done adiabatically, *i.e.*, Majoranas need to be exchanged without being brought in close proximity to assure that the system stays in the ground state (degenerate ground state). Many different theoretical proposals are given with the essential hardware being a single crystalline nanowire network coupled to superconducting islands.[17-22] For example, a T-shaped proximitized nanowire network that relies on the physical exchange of Majoranas[17] or a braiding system that confides in coupling (tunnel or Coulomb origin) between Majoranas without the need to physically move them[18-21].

More recent proposals suggest measurement-based protocols, where the quantum operations are carried out by measuring the state of the qubits instead of braiding.[22] In addition, schemes involving interferometric operations are explored. The idea for the interference experiment is rooted in the observation of the phase shift through a two-lead "hashtag" structure, see Figure 2.6. Two parameters are coupled to the phase of a topological superconductor and experience a parity-dependent (odd or even) phase shift (π-shift) which can then be measured by various means: The parity of quantum dots and the position of MZM. If the single electron transport trough the nanowire "hashtag" is coherent, the hybridization of left and right quantum dots should show Aharonov-Bohm oscillations when changing the enclosed flux, ϕ.[22]
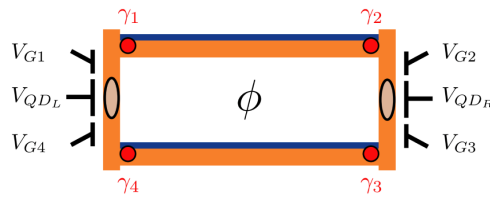
Figure 2.6 | Majorana interferometer. Semiconductor nanowire "hashtag" (orange) coupled with two superconducting islands (blue). The system is tuned into the topological regime. Coherent transport through the interferometer probes the non-local nature of Majoranas. The position of Majoranas, γ_i ($i = 1,\dots 4$) is represented as red dots. The quantum dots are defined by the gates (left and right branch of the semiconductor nanowire).

Developing high-quality semiconductor nanowire networks where braiding operations are possible is a prerequisite to topological qubits. Different network architectures can open a possibility to probe the local density of states of proximitized nanowire, an unique way to discriminate Majoranas from possibly disorder-induced states. The growth of nanowire networks, based on InSb and InAs material, suitable for Majorana experiments are reported,[23-27] and recent progress on InSb-based nanowire networks is in Chapter 4.

2.2 Quantum materials

The central part of the Majorana device is the proximitized Majorana nanowire. Materials that constitute the Majorana nanowire – quantum materials – must abide strict material requirements, outlined in the "recipe" by Lutchyn *et al*.[3] and Oreg *et al*.[4] As mentioned in the Subsection 2.1.1, semiconductors based on InSb or InAs are potential candidates for the nanowire material, whereas Al and NbTiN for the superconducting component. The work in this thesis focuses on perfecting the growth of InSb nanowires and Al-InSb nanowire quantum devices. In Table 2.1 relevant bulk properties of InSb and Al are listed (taken from Reference 5).

Table 2.1 | **Bulk properties of Majorana quantum materials.** Adapted from the Reference 5. Note: The Al-InSb superconducting gap is larger than the gap in bulk Al.

Semiconductor	InSb
g-factor	$40 - 50$
effective mass m^*	$0.014\ m_e$
spin-orbit energy E_{SO}	$0.05 - 1$ meV
spin-orbit coupling α_R	$0.2 - 1$ eV Å
spin-orbit length $\lambda_{SO} = 1/k_{SO}$	$230 - 50$ nm
lattice constant	6.479 Å
Superconductor	**Al**
superconducting gap Δ	0.2 meV
critical field B_C	10 mT
critical temperature T_C	1.2 K
coherence length	1600 nm
lattice constant (FCC)	4.051 Å
Superconductor-semiconductor	**Al-InSb**
superconducting gap Δ_0	$0.2 - 0.3$ meV

2.2.1 InSb nanowires

Indium-antimonide (InSb) nanowires NWs are among the rising star nanostructures due to their potential for hosting topological phases of matter, such as Majorana zero modes[9,10,28] and their appraisal as prime candidates for topological quantum computation. Compared to other III-Vs, InSb has unique properties that allow for different applications, not only topological quantum computing[1,4] but also for spin-based devices[29] and thermoelectric devices[30-32]. InSb has a very narrow direct bandgap of 0.17 eV and the highest bulk electron mobility (77000 Vs/cm^2 at 300K), owing to its low electron effective mass[33]. Together with its large Landé g-factor[34] and its strong spin-orbit interaction (SOI) brought forth by its high atomic number, InSb is an ideal material for spin-orbit quantum bit (qubit) devices[35,36] in addition to its ability to attain stringent material requirements for bearing Majoranas when combined with superconducting materials[5,9]. Another remarkable feature of this material is its crystal perfection, reducing the probability of forming stacking faults and thus strongly favoring the pure zinc blende crystal structure (see TEM analysis

in the Chapter 3).[37] The odds of defect formation are even further reduced in vapor-liquid-solid (VLS) grown NWs, discussed in Section 2.3.

2.2.2 Superconductors

A number of experimental routes with the universal goal to reduce the superconductor-semiconductor interface disorder are explored.[14-16,38] Primary, the thin superconducting film should stay thin enough to withstand high parallel magnetic fields, and uniform along and across the nanowire to ensure long coherence length, and disorder-free interface. Secondly, superconductor materials that are compatible with standard fabrication techniques are favored.

Type I superconductors with long superconducting coherence length are the prime candidates for Majorana devices as they, in particular, can eliminate or decrease the number of vortices in the superconductor. In other words, it is the length scale that defines the size of the vortex, hence the thinner the superconductor, the longer the coherence length, which lowers the number of vortices. Vortices are contemplated to create a dissipation channel,[39] the leading hypothetical mechanism that limits the ZBP height from reaching the quantized value of $2e^2/h$.

Most importantly, material science dictates consideration of additional requirements and uncertainties. Those are listed as bullet points and will be referred to in Chapter 5.

- Superconducting thin film should be uniform in thickness.
- Superconducting thin film must not oxidize completely over the course of a few days (*e.g.,* typical fabrication time); a suitable capping layer must be used.
- Superconducting material that is closer with its lattice constant value to the one of InSb is favorable. Strain from the superconductor should not lead to significant bending of the nanowire or change the electronic band structure.
- The melting/interdiffusion temperature of the superconductor should withstand the typical device processing temperatures (~ 100 – 200 °C).

The work in this thesis focuses on the growth of Al superconducting films on InSb nanowires. Al can be deposited with different techniques such as sputtering, evaporation (electron gun and thermal) and molecular beam epitaxy (MBE). An MBE offers ultra-high vacuum and the possibility of *in-situ* device growth.

2

2.3 Growth of crystalline materials

The task of the crystal growers is not only to synthesize quantum materials but also to perfect the growth and achieve an excellent control over the crystalline quality. By controlling the material properties such as composition, growth direction, crystal phase, thickness, disorder, *etc.*, the grower can tailor the quantum mechanical properties. As a consequence, these high-quality materials will serve as a platform to discover new phenomena in physics.[9,40-42]

2.3.1 Vapor-liquid-solid mechanism for the nanowire growth

Since the vapor-liquid-solid (VLS) method for the growth of nanowires was discovered at Bell Labs,[43] many research groups are using this method for the growth of 1D nanowires with very large aspect ratios and with diameters ranging from 10 to 100 nm. The basis of the VLS growth is a (foreign) metal catalyst particle that acts as a sink for the precursor materials, thereby establishing a local supersaturation, resulting in nanowire growth. VLS nanowire growth involves three distinct stages: alloying, nucleation, and growth. To understand the fundamental physics behind the first stage of the VLS method, one should know the phase diagram of the materials involved. From the phase diagram the eutectic temperature of the system, *i.e.*, the minimum temperature where the alloy can exist in the liquid form, is known. Here, the contact angle of the catalyst particle to the substrate determines the nanowire morphology and the crystal phase. After a supersaturated alloy has been formed, due to the continuous supply of the precursor material, growth takes place. This step of the VLS growth is most unknown to material scientists. The following process is the growth of the nanowire in a layer-by-layer fashion.
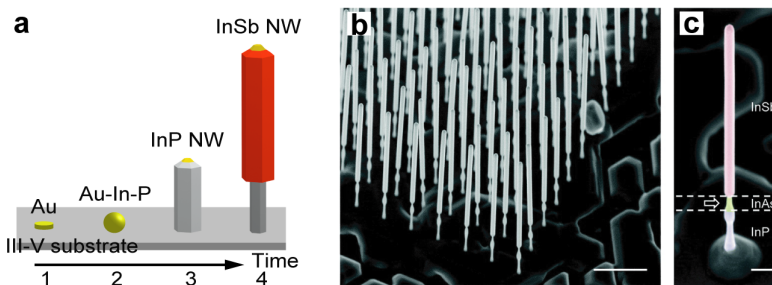
Figure 2.7 | **VLS growth of InSb heterostructure nanowires. a,** Schematic illustration of the VLS growth mechanism of InSb nanowires**.** 1) Gold (Au) catalyst particles are deposited on a III-V substrate. The substrate is placed into an MOVPE reactor and heated up to the growth temperature. 2) Constant flow of material sources is supplied to the catalyst particle via the gas phase and forms a liquid Au-In-P (III-V) alloy that becomes supersaturated. 3) The growth of InP nanowires happens at the liquid (catalyst) – solid (substrate) interface. 4) The growth of heterostructured InP-InSb nanowires. **b,** 30°-tilted SEM images of an InSb nanowire array.[44] The scale bar corresponds to 1 μm. **c,** High magnification SEM image of a single heterostructure nanowire. Color indicates the stacking of materials: InP (blue), InAs (green), and InSb (red). The scale bar is 200 nm.

The mechanism behind the VLS growth is studied to a great extend and different growth models are proposed based on *ex-situ* and *in-situ* analysis methods.[43,45-48] A common catalyst for the VLS growth is gold (Au). Steps of the VLS growth are depicted in Figure 2.7. Gold catalyst particles are deposited on the growth substrate either by deposition of a thin gold layer, randomly using gold colloids, or delicately prepositioned using lithography methods (electron beam or nanoimprint lithography). Due to the special properties of nanowires coming from their narrow dimensions, it is possible to use highly lattice-mismatched materials as substrates for the growth. In addition, this implies that it is possible to grow nanowire heterostructures while maintaining the crystal quality. In recent years, heterostructure nanowires (InP/InSb, InAs/InSb) containing a high quality InSb segment have been realized by means of MOVPE, types of chemical vapor deposition (CVD), chemical beam epitaxy (CBE) and MBE mainly using Au or silver (Ag) as a catalyst particle for the VLS growth.[26,44,49-53] The challenge is to make InSb nanowires impurity and defect free, long for employability in device fabrication and thin to maintain one-dimensionality and therefore their quantum mechanical properties.

In this thesis, VLS nanowire growth was performed using Au catalysts finely defined on the substrate using electron beam (e-beam) lithography. Growth details are given in Chapters 4-7. The nanowires are defect free and have zinc blende (ZB) crystal structure (see Chapter 3, Figure 3.8). The bottom-up growth of InSb nanostructures in this thesis employs two mechanisms, VLS facilitated by a gold particle and selective-area growth (SAG) using a Si_xN_y mask similar to the work of Dalacu *et al.*[54] The abovementioned combinations enhance the selectivity and eliminate parasitic InSb growth.

2

2.3.2 Epitaxial growth of crystalline thin films

Thin metallic films have broad application in the semiconductor industry and are also important for research in condensed matter physics. Vigorous demands of Majorana nanowire device includes growth of uniform and high quality thin superconducting films (~ 10 nm).

The experimental realization of Al thin films requires controlled growth conditions as they play an extremely important role in determining the morphological, structural and electrical characteristics. Two important parameters of the crystal growth, the diffusion length of adatoms and grain growth rate, dictate the morphology of thin films.

Experimentally, depending on the surface energies and the lattice mismatch between the adlayer and the substrate, three different epitaxial growth modes of thin films are defined: Frank-van der Merwe (FM), Volmer-Weber (VW) and Stranski-Krastanov (SK). The above mentioned are schematically depicted in Figure 2.8. FM growth can be recognized by the atom-by-atom deposition on the substrate followed by 2D layer-by-layer-growth. The growth of a new layer occurs only when the layer below is complete. This growth mode is recognized in the growth of epitaxial crystalline thin films with small lattice mismatch to the substrate, and an adlayer having a lower or comparable surface energy to that of the substrate.
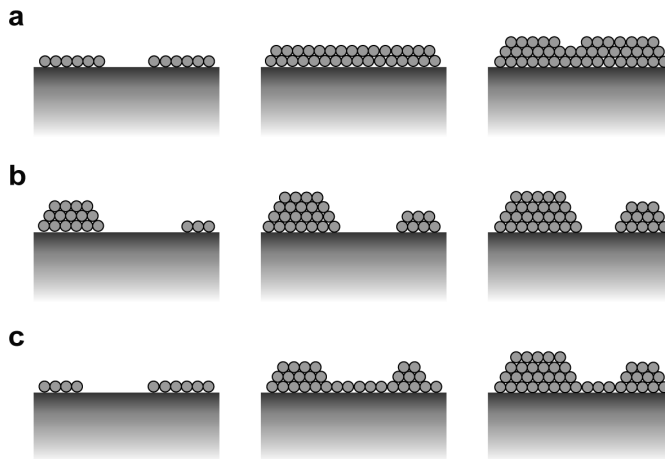
Figure 2.8 | Epitaxial growth of crystalline thin films. a, Frank-van der Merwe, **b,** Volmer-Weber, and **c,** Stranski-Krastanov epitaxial growth modes.

In case of 3D island growth, the growth mode is VW. Here islands spread until they impinge on other islands and eventually form a film. The crystalline film has a large lattice mismatch to the substrate. Generally, the adlayer has a higher surface energy than the substrate. SK growth represents the combination of the other two previously mentioned. Initially layer-by-layer growth is dominating and after reaching the critical thickness, 3D island growth occurs on top of the wetting layer. The adlayer has a lower surface energy than the substrate and therefore tends to wet

the surface, but due to a mismatch in lattice parameters, strain builds up resulting in island growth. A special case of VW growth, *epitaxial grain growth*, is interesting because a grain growth at reduced temperatures can result in a monocrystalline or near monocrystalline thin film. This growth mechanism is reported for metal thin films.[38,55] The steps of the growth are shown in Figure 2.9.

1

2

3
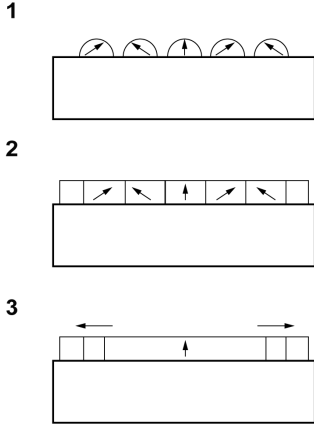
Figure 2.9 | **Schematic of the *epitaxial grain growth* at low substrate temperature**. The growth of islands on single-crystalline substrate at low temperatures. **1,** Initial nuclei do not have uniform crystallographic orientation relationship with the substrate. **2,** Grain growth and formation of a polycrystalline film. **3,** Epitaxial alignment of grains results in an *epitaxial grain growth*. Adapted from Reference 55.

The morphology of the thin film depends on the diffusion length of the adatoms, λ, and the growth rate, $\dot{r}$. Importantly, the diffusion length is a function of parameters that can be controlled directly during the growth by the flux of the source material and the substrate temperature. Macroscopically, the thermal mobility of adsorbed particles can be explained by Brownian motion in two dimensions.[56] The diffusion length can be given as:[38]

$$\lambda_{a,j} \propto \sqrt{D_{a,j}\tau_{a,j}} \tag{2.4}$$

Where $D_{a,j}$ is the diffusion coefficient and $\tau_{a,j}$ is the adatom lifetime.

Considering the transition state theory, the diffusion coefficient can be defined as:

$$D_{a,j} \propto l^2\Gamma = l^2 v e^{-\frac{\Delta\Phi}{k_B T}} \tag{2.5}$$

Where l is the distance between the adjacent, binding, sites of adatoms, Γ is the hopping rate. The hopping rate is dependent on the attempt frequency, v, that can be associated with the vibrational frequency of the adatoms, and the potential energy barrier, $\Delta\Phi$. k_B is Boltzmann's constant and T the temperature. Generally, when growing a crystalline thin film on a lattice-mismatched substrate, a lower substrate temperature is favored in order to reduce the diffusion of atoms on the surface.

Now we will define the grain growth rate. Different post-nucleation processes mentioned in step 3 of the *epitaxial grain growth* in the Figure 2.9 can be surface-driven growth, grain-boundary driven growth, strain-driven growth, *etc*. The *grain growth* process is driven exponentially by thermodynamic excesses such as interfacial and strain-free energies.[5,38] The grain-growth minimizes the total energy

2

of a solid by elimination of grain boundaries. When considering bulk materials, the growth rate of individual grains is given by:

$$\dot{r} = \frac{dr}{dt} = M\gamma_{gb} \left(\frac{1}{\bar{r}} - \frac{1}{r} \right) \tag{2.6}$$

Where M is the average grain boundary mobility, γ_{gb} is the average grain boundary energy, $\bar{r}$ is the average grain radius and r is the radius of the grain under consideration.

The grain growth in thin films also occurs in order to minimize the total energy of the film, but in this case an additional component is added, that is the energy of the top and the bottom surfaces of the film, hence the surface-driven grain growth rate is:

$$\dot{r} = \frac{dr}{dt} = M \left[\frac{2(\gamma_s^* - \gamma_s)}{h} + \gamma_{gb} \left(\frac{1}{\bar{r}} - \frac{1}{r} \right) \right] \tag{2.7}$$

Where γ_s^* is the average surface energy of the film, γ_s the surface energy of the growing grain and h is the film thickness. The surface energy of the growing grain strongly depends on the crystallographic orientation of a grain. As a result, the grains with crystal orientation that lead to low surface energies will grow faster. The abovementioned results in thin films that are composed of large grains with unimodal distribution of sizes. The key to obtaining a short adatom diffusion length and reducing the size of the crystalline grains is lowering the temperature. Some materials need cryogenic temperatures in order to form a thin epitaxial film. This is the special condition of growth that can be realized in molecular beam epitaxy.

2.4 References

1   Kitaev, A. Y. Unpaired Majorana fermions in quantum wires. *Physics-Uspekhi* **44**, 131 (2001).

2   Samarth, N. Quantum materials discovery from a synthesis perspective. *Nature Materials* **16**, 1068, doi:10.1038/nmat5010 (2017).

3   Lutchyn, R. M., Sau, J. D. & Das Sarma, S. Majorana Fermions and a Topological Phase Transition in Semiconductor-Superconductor Heterostructures. *Physical Review Letters* **105**, 077001, doi:10.1103/PhysRevLett.105.077001 (2010).

4   Oreg, Y., Refael, G. & von Oppen, F. Helical Liquids and Majorana Bound States in Quantum Wires. *Physical Review Letters* **105**, 177002, doi:10.1103/PhysRevLett.105.177002 (2010).

5   Lutchyn, R. M. *et al.* Majorana zero modes in superconductor–semiconductor heterostructures. *Nature Reviews Materials* **3**, 52-68, doi:10.1038/s41578-018-0003-1 (2018).

6   Aguado, R. Majorana quasiparticles in condensed matter. *ArXiv e-prints* (2017).

7   Zuo, K., and Mourik, M. *Signatures of Majorana Fermions in Hybrid Superconductor-Semiconductor Nanowire Devices* Doctoral thesis, Delft University of Technology, (2016).

8   Gül, Ö. *Ballistic Majorana nanowire devices* Doctoral thesis, Delft University of Technology, (2017).

9   Mourik, V. *et al.* Signatures of Majorana Fermions in Hybrid Superconductor-Semiconductor Nanowire Devices. *Science* **336**, 1003-1007, doi:10.1126/science.1222360 (2012).

10   Deng, M. T. *et al.* Anomalous Zero-Bias Conductance Peak in a Nb–InSb Nanowire–Nb Hybrid Device. *Nano Letters* **12**, 6414-6419, doi:10.1021/nl303758w (2012).

11   Churchill, H. O. H. *et al.* Superconductor-nanowire devices from tunneling to the multichannel regime: Zero-bias oscillations and magnetoconductance crossover. *Physical Review B* **87**, 241401, doi:10.1103/PhysRevB.87.241401 (2013).

12   Das, A. *et al.* Zero-bias peaks and splitting in an Al–InAs nanowire topological superconductor as a signature of Majorana fermions. *Nature Physics* **8**, 887, doi:10.1038/nphys2479 (2012).

13   Finck, A. D. K., Van Harlingen, D. J., Mohseni, P. K., Jung, K. & Li, X. Anomalous Modulation of a Zero-Bias Peak in a Hybrid Nanowire-Superconductor Device. *Physical Review Letters* **110**, 126406, doi:10.1103/PhysRevLett.110.126406 (2013).

14   Gül, Ö. *et al.* Ballistic Majorana nanowire devices. *Nature Nanotechnology* **13**, 192-197, doi:10.1038/s41565-017-0032-8 (2018).

15   Gül, Ö. *et al.* Hard Superconducting Gap in InSb Nanowires. *Nano Letters* **17**, 2690-2696, doi:10.1021/acs.nanolett.7b00540 (2017).

16   Zhang, H. *et al.* Ballistic superconductivity in semiconductor nanowires. *Nature Communications* **8**, 16025, doi:10.1038/ncomms16025 (2017).

17   Alicea, J., Oreg, Y., Refael, G., von Oppen, F. & Fisher, M. P. A. Non-Abelian statistics and topological quantum information processing in 1D wire networks. *Nature Physics* **7**, 412, doi:10.1038/nphys1915 (2011).

18   Hyart, T. *et al.* Flux-controlled quantum computation with Majorana fermions. *Physical Review B* **88**, 035121, doi:10.1103/PhysRevB.88.035121 (2013).

19   Aasen, D. *et al.* Milestones Toward Majorana-Based Quantum Computing. *Physical Review X* **6**, 031016, doi:10.1103/PhysRevX.6.031016 (2016).

20   Stephan, P., Asbjørn, R., Reinhold, E. & Karsten, F. Majorana box qubits. *New Journal of Physics* **19**, 012001 (2017).

21   Vijay, S. & Fu, L. Teleportation-based quantum information processing with Majorana zero modes. *Physical Review B* **94**, 235446, doi:10.1103/PhysRevB.94.235446 (2016).

22   Karzig, T. *et al.* Scalable designs for quasiparticle-poisoning-protected topological quantum computation with Majorana zero modes. *Physical Review B* **95**, 235305, doi:10.1103/PhysRevB.95.235305 (2017).

23   Dalacu, D., Kam, A., Austing, D. G. & Poole, P. J. Droplet Dynamics in Controlled InAs Nanowire Interconnections. *Nano Letters* **13**, 2676-2681, doi:10.1021/nl400820w (2013).

24   Kang, J.-H. *et al.* Crystal Structure and Transport in Merged InAs Nanowires MBE Grown on (001) InAs. *Nano Letters* **13**, 5190-5196, doi:10.1021/nl402571s (2013).

25   Plissard, S. R. *et al.* Formation and electronic properties of InSb nanocrosses. *Nature Nanotechnology* **8**, 859, doi:10.1038/nnano.2013.198 (2013).

26   Car, D., Wang, J., Verheijen, M. A., Bakkers, E. P. A. M. & Plissard, S. R. Rationally Designed Single-Crystalline Nanowire Networks. *Advanced Materials* **26**, 4875-4879, doi:10.1002/adma.201400924 (2014).

2

27   Rieger, T. *et al.* Crystal Phase Transformation in Self-Assembled InAs Nanowire Junctions on Patterned Si Substrates. *Nano Letters* **16**, 1933-1941, doi:10.1021/acs.nanolett.5b05157 (2016).

28   Zhang, H. *et al.* Quantized Majorana conductance. *Nature* **556**, 74, doi:10.1038/nature26142 (2018).

29   Nadj-Perge, S., Frolov, S. M., Bakkers, E. P. A. M. & Kouwenhoven, L. P. Spin–orbit qubit in a semiconductor nanowire. *Nature* **468**, 1084, doi:10.1038/nature09682 (2010).

30   Mingo, N. Thermoelectric figure of merit and maximum power factor in III–V semiconductor nanowires. *Applied Physics Letters* **84**, 2652-2654, doi:10.1063/1.1695629 (2004).

31   Yazji, S. *et al.* Assessing the thermoelectric properties of single InSb nanowires: the role of thermal contact resistance. *Semiconductor Science and Technology* **31**, 064001 (2016).

32   Cheng, Y. *et al.* New insight into InSb-based thermoelectric materials: from a divorced eutectic design to a remarkably high thermoelectric performance. *Journal of Materials Chemistry A* **5**, 5163-5170, doi:10.1039/C6TA10827J (2017).

33   Vurgaftman, I., Meyer, J. R. & Ram-Mohan, L. R. Band parameters for III–V compound semiconductors and their alloys. *Journal of Applied Physics* **89**, 5815-5875, doi:10.1063/1.1368156 (2001).

34   Nilsson, H. A. *et al.* Giant, Level-Dependent g Factors in InSb Nanowire Quantum Dots. *Nano Letters* **9**, 3151-3156, doi:10.1021/nl901333a (2009).

35   Pribiag, V. S. *et al.* Electrical control of single hole spins in nanowire quantum dots. *Nature Nanotechnology* **8**, 170, doi:10.1038/nnano.2013.5 (2013).

36   van den Berg, J. W. G. *et al.* Fast Spin-Orbit Qubit in an Indium Antimonide Nanowire. *Physical Review Letters* **110**, 066806, doi:10.1103/PhysRevLett.110.066806 (2013).

37   Borg, B. M. & Lars-Erik, W. Synthesis and properties of antimonide nanowires. *Nanotechnology* **24**, 202001 (2013).

38   Krogstrup, P. *et al.* Epitaxy of semiconductor–superconductor nanowires. *Nature Materials* **14**, 400, doi:10.1038/nmat4176 (2015).

39   Liu, C.-X., Sau, J. D. & Das Sarma, S. Role of dissipation in realistic Majorana nanowires. *Physical Review B* **95**, 054502, doi:10.1103/PhysRevB.95.054502 (2017).

40   Klitzing, K. v., Dorda, G. & Pepper, M. New Method for High-Accuracy Determination of the Fine-Structure Constant Based on Quantized Hall Resistance. *Physical Review Letters* **45**, 494-497, doi:10.1103/PhysRevLett.45.494 (1980).

41   Pfeiffer, L. & West, K. W. The role of MBE in recent quantum Hall effect physics discoveries. *Physica E: Low-dimensional Systems and Nanostructures* **20**, 57-64, doi:10.1016/j.physe.2003.09.035 (2003).

42   Alivisatos, A. P. Semiconductor Clusters, Nanocrystals, and Quantum Dots. *Science* **271**, 933-937, doi:10.1126/science.271.5251.933 (1996).

43   Wagner, R. S. & Ellis, W. C. Vapor-liquid-solid mechanism of single crystal growth. *Applied Physics Letters* **4**, 89-90, doi:10.1063/1.1753975 (1964).

44   Plissard, S. R. *et al.* From InSb Nanowires to Nanocubes: Looking for the Sweet Spot. *Nano Letters* **12**, 1794-1798, doi:10.1021/nl203846g (2012).

45   Glas, F., Harmand, J.-C. & Patriarche, G. Why Does Wurtzite Form in Nanowires of III-V Zinc Blende Semiconductors? *Physical Review Letters* **99**, 146101, doi:10.1103/PhysRevLett.99.146101 (2007).

46   Dubrovskii, V. G., Sibirev, N. V., Harmand, J. C. & Glas, F. Growth kinetics and crystal structure of semiconductor nanowires. *Physical Review B* **78**, 235301, doi:10.1103/PhysRevB.78.235301 (2008).

47   Joyce, H. J., Wong-Leung, J., Gao, Q., Tan, H. H. & Jagadish, C. Phase Perfection in Zinc Blende and Wurtzite III−V Nanowires Using Basic Growth Parameters. *Nano Letters* **10**, 908-915, doi:10.1021/nl903688v (2010).

48   Jacobsson, D. *et al.* Interface dynamics and crystal phase switching in GaAs nanowires. *Nature* **531**, 317, doi:10.1038/nature17148 (2016).

49   Caroff, P. *et al.* High-Quality InAs/InSb Nanowire Heterostructures Grown by Metal–Organic Vapor-Phase Epitaxy. *Small* **4**, 878-882, doi:10.1002/smll.200700892 (2008).

50   Daniele, E. *et al.* InAs/InSb nanowire heterostructures grown by chemical beam epitaxy. *Nanotechnology* **20**, 505605 (2009).

51   Vogel, A. T. *et al.* Fabrication of High-Quality InSb Nanowire Arrays by Chemical Beam Epitaxy. *Crystal Growth & Design* **11**, 1896-1900, doi:10.1021/cg200066q (2011).

52   Pan, D. *et al.* Free-Standing Two-Dimensional Single-Crystalline InSb Nanosheets. *Nano Letters* **16**, 834-841, doi:10.1021/acs.nanolett.5b04845 (2016).

53   Thelander, C., Caroff, P., Plissard, S. & Dick, K. A. Electrical properties of $InAs_{1-x}Sb_x$ and InSb nanowires grown by molecular beam epitaxy. *Applied Physics Letters* **100**, 232105, doi:10.1063/1.4726037 (2012).

54   Dan, D. *et al.* Selective-area vapour–liquid–solid growth of InP nanowires. *Nanotechnology* **20**, 395602 (2009).

55   Thompson, C. V., Floro, J. & Smith, H. I. Epitaxial grain growth in thin metal films. *Journal of Applied Physics* **67**, 4099-4104, doi:10.1063/1.344969 (1990).

56   Brown, R. A brief account of microscopical observations made in the months of June, July and August 1827, on the particles contained in the pollen of plants; and on the general existence of active molecules in organic and inorganic bodies. *The Philosophical Magazine* **4**, 161-173, doi:10.1080/14786442808674769 (1828).

3

Chapter

Growth and functional characterization methods

Abstract *The methods of crystal growth, materials characterization, quantum device fabrication and measurement techniques enabling the experiments in this dissertation are discussed. First, a general introduction to the growth of crystalline materials using metal-organic vapor phase epitaxy (MOVPE) and molecular beam epitaxy (MBE) is given. Then, the functional characterization methods employing scanning electron microscopy (SEM) and transmission electron microscopy (TEM) are described. I will discuss the TEM imaging and challenges, in particular focusing on analysis of nanowires. Finally, a brief discussion about the measurement equipment and device fabrication (highlighting important steps) is included. This chapter is not exhaustive, it rather focuses on the topics which are relevant for this thesis and motivates the results which are presented in the results (Chapters 4-7).*

3.1 Growth techniques

Epitaxy is the process of growing a crystal of a particular orientation on top of another crystal, where the orientation is determined by the underlying crystal. The word epitaxy derives from the Greek prefix *epi* meaning "upon" or "over" and *taxis* meaning "arrangement" or "order". Techniques such as MOVPE and MBE are epitaxy techniques and are used for the growth of high-quality crystalline materials. Both techniques are being used within the scope of this thesis.

3.1.1 MOVPE

The epitaxial growth technique used for the nanowire growth in this thesis was MOVPE. The first reports on MOVPE growth of III-V semiconductors have been given in patent files as early as in 1954 (InSb) and 1962/63 (GaAs).[1] It is a low vacuum system (10 – 50 mbar) that uses high purity carrier gas (usually H_2). As mentioned in the name of the technique, the main sources for the crystal growth in a MOVPE reactor are metal-organic (MO) sources such as *trimethyl*-indium (TMIn), *trimethyl*-antimony (TMSb), *etc.*, and hydride sources such as phosphine (PH_3) and arsine (AsH_3). Other, dopant sources for instance, as H_2S can be added as well. An MOVPE reactor is schematically outlined in Figure 3.1. While hydrides are carried directly from the source bottles into the gas lines, the MO sources (either liquids or powders) are stored in metal containers, so-called bubblers. A bubbler is stored in a thermostatic bath that is usually kept at temperatures around -15 – 17 °C. To extract the source material from the bubbler, H_2 gas is introduced to the bubbler through the inlet. H_2 creates bubbles and carries the source vapor trough the outlet into the gas lines towards the reactor. The gas lines are heated to prevent condensation. The molar flow of the extracted MO source is determined by controlling three parameters: 1) the flow of the carrier gas (H_2) through the inlet of bubbler, 2) the total pressure of the bubbler and 3) the temperature of the bubbler. Detailed formulations can be found in chemical vapor epitaxy (CVD) and MOVPE growth text books.[1,2]
The mixing of the gases takes place at the gas inlet located at the very beginning of the reactor chamber. The reactor chamber, a quartz glass tube, is the part of MOVPE where the pyrolysis of source molecules in the gas phase take place close to the heated substrate. This is followed by diffusion of adatoms on the substrate and eventually the semiconductor crystalline material is grown. The temperature of the

substrate in a MOVPE reactor is usually around 400 – 1000 °C. Different sources have different pyrolysis temperatures, and therefore different source decomposition rates. The decomposition rate of a certain source is the most important quantity next to the vapor pressure.[1] Depending on where the decomposition takes place, the reaction can be homogeneous, *i.e.*, take place in the gas phase, or heterogeneous, *i.e.*, take place at the sample surface.

3
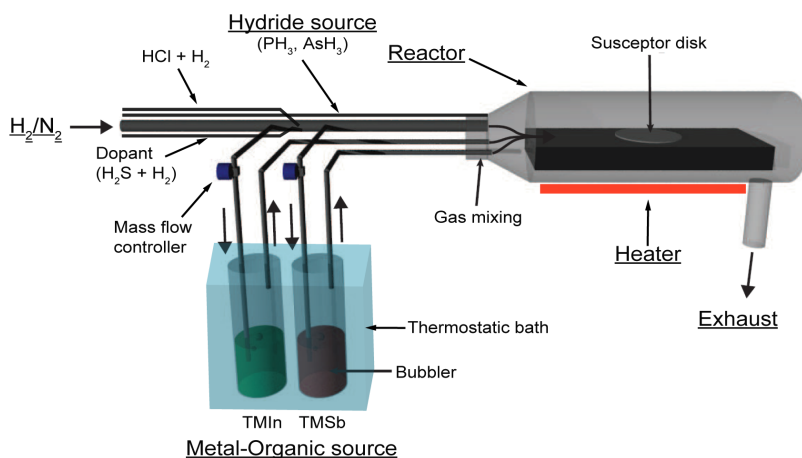
Figure 3.1 | Schematic illustration of a horizontal MOVPE reactor used in this thesis. Hydrogen is used as a carrier gas for sources (hydrides and metal-organic sources). The reaction and the epitaxial growth happens in the reactor, on the graphite susceptor disk. The heaters of the reactor are infra-red (IR) lamps. Adapted from Reference 3.

Even though MOVPE seems to be a practical machine, the growth process is very complex and there are many parameters that influence the growth of different crystalline materials. That is, the temperature and the exact geometry of the reactor which are responsible for the decomposition (homogeneous and/or heterogeneous) rate of the material and its diffusion length. The growth of Sb-based materials, such as InSb, is challenging because the pyrolysis temperature of a standard MO source *trimethyl*-antimony (TMSb) is higher than the usual growth temperature (over 400 °C).[2] This influences the growth kinetics and reduces the growth window for InSb nanowires. When MO sources do not decompose completely, a metal ion stays attached to an alkyl-group (*methyl-* or *ethyl-*). The presence of alkyl-groups could result in a high carbon incorporation in the grown crystal, hence reduced device performance. This is a major bottleneck for applications such as quantum devices where a low carbon incorporation is vital. To avoid carbon incorporation, suitable MO sources as well as high growth temperatures are desired.

There are different commercially available MOVPE reactors: a vertical showerhead and horizontal reactor. Both reactors employ substrate rotation in order to achieve uniform growth. The work in this thesis was performed on an Aixtron Dual Horizontal Reactor (schematic in Figure 3.1). Here, the cracking of source materials

happens not only at the substrate but also close to the gas mixing inlet of the reactor. This enhances the decomposition rate of TMSb, for instance, which is the reason why this reactor geometry is chosen for the growth of InSb nanowires. Another advantage of the horizontal reactor is the possibility to replace whole reactor parts (quartz tube, susceptor) when switching from one growth material to another. In this way, the cross-contamination is reduced and "ultra-pure" materials can be grown.

3.1.2 MBE

An MBE chamber is an ultrahigh vacuum (UHV) system which enables the epitaxial growth of various materials. The main advantages over MOVPE are the growth of high quality, pure material, low growth temperatures (no need to crack/decomposition the source in the reactor) and relatively low growth rate (1-2 Å/s), and the possibility to integrate *in-situ* characterization techniques. The background pressure of MBE system is at ultra-high vacuum (UHV) values, ~ 10^{-10} Torr. An MBE machine consists of a stainless-steel chamber equipped with high operation performance ion pumps and/or cryopumps in addition to cryopanels surrounding the walls of the chamber with flowing liquid nitrogen (LN_2). A schematic of an MBE chamber is shown in Figure 3.2. Usually, laboratories working on the MBE growth do not have single MBE chambers, but multiple chambers connected to each other with transfer tubes, forming an MBE cluster tool. The cluster tool gives an advantage if one is interested in growth of *in-situ* devices, for example.
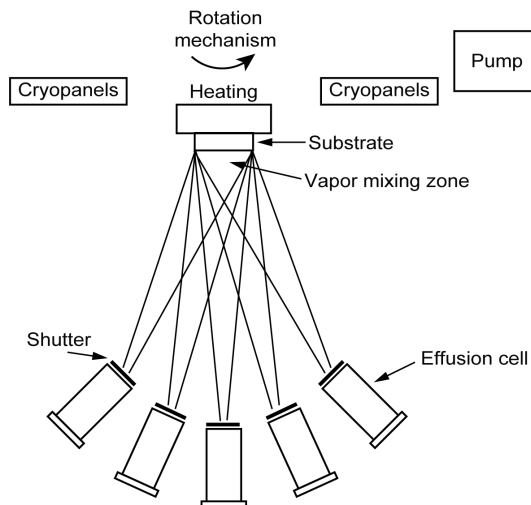
Figure 3.2 | **Schematic illustration of an MBE chamber.** Effusion cells are positioned on the bottom of the sample holder with substrate. The chamber is surrounded by cryopanels.

The material for the growth is stored in cells. One MBE chamber can have many ports for cells. The design of the cells can be different depending on the material that

needs to be evaporated. Solid source materials are supplied from effusion cells for instance, while cracker cells are mainly used for the group V materials like Sb and As. Cells are positioned at the bottom of the chamber and directed towards the substrate holder at a certain angle (30° – 45°). Due to the UHV conditions in an MBE chamber, the atoms have a long mean free path, and the crystal growth occurs only at the surface of the substrate.

The growth of crystalline thin films of aluminium reported in this thesis was performed in an MBE cluster in Palmstrøm's group at the University of California in Santa Barbara. The experiments presented in Chapter 5 are the result of the growth in UHV, using a cooling stage that is part of an MBE cluster tool. A schematic and a photo of the cold stage are shown in Figure 3.3. The cold stage is designed especially for the deposition of highly diffusive metals, such as aluminum (Al), that requires a low deposition temperature close to liquid nitrogen (LN$_2$) temperatures enabling the growth of an uniform crystalline film.
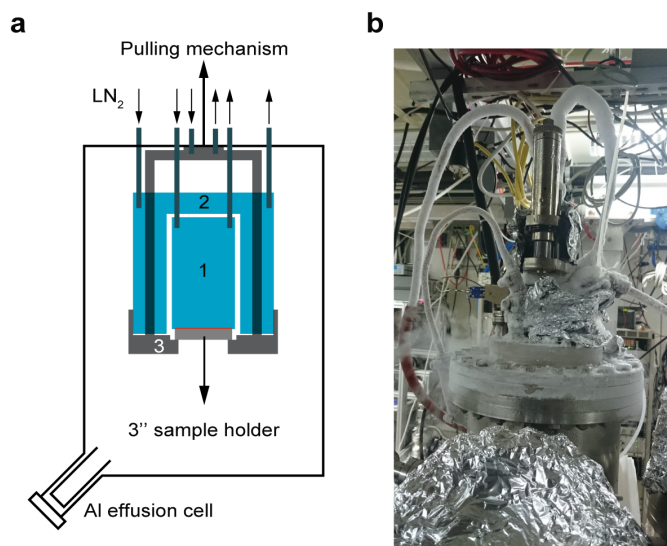
Figure 3.3 | Schematic illustration of a UHV cooling stage. a, Schematic of a cold stage with Aluminium effusion cell. The 3-inch sample holder is surrounded by three compartments (1, 2 and 3 in the schematic) actively cooled by LN$_2$. Active cooling allows for stable sample temperatures at ~85 K. The temperature is measured by a thermocouple type K positioned in the back of the sample holder. The aluminum (Al) effusion cell is under 45° angle with respect to the sample holder. **b,** Photograph of the cold stage before the deposition. Inlets and outlets of LN$_2$, as well as the pulling mechanism, are clearly visible.

3.2 Functional characterization methods

Scanning electron microscopy (SEM) and transmission electron microscopy (TEM) are the main growth feedback techniques in the field of nanowires. There are two steps towards functional characterization of nanowires. First, after the growth of the nanowire building block, the SEM is used to demonstrate if the desired structure is grown. Then, the crystalline quality is determined using TEM. More complex techniques developed within the TEM are used to inspect the detailed structural quality such as growth direction, presence of defects, compositional information, *etc*. Therefore, in addition to the basic working principles of characterization techniques, boosting the functionality of these techniques for nanowire applications is desirable in order to provide adequate feedback.

3.2.1 Scanning electron microscopy (SEM) with nanorobots

Scanning electron microscopy is a vital imaging tool used to examine the nanowire yield, aspect ratios and surface morphologies. SEM uses a finely focused beam of electrons in order to produce a high-resolution image of a sample allowing resolutions as small as 0.8 nm. A cross-sectional schematic of an SEM is illustrated in Figure 3.4a. The most fascinating innovation in recent research in the field of bottom-up grown nanomaterials takes advantage of the precise manipulation of nanostructures using nanomanipulators. The applications can be: the fabrication of a complicated prototype device made of a single nanostructure or to transfer a structure for further structural characterization (HR-TEM), *etc*.
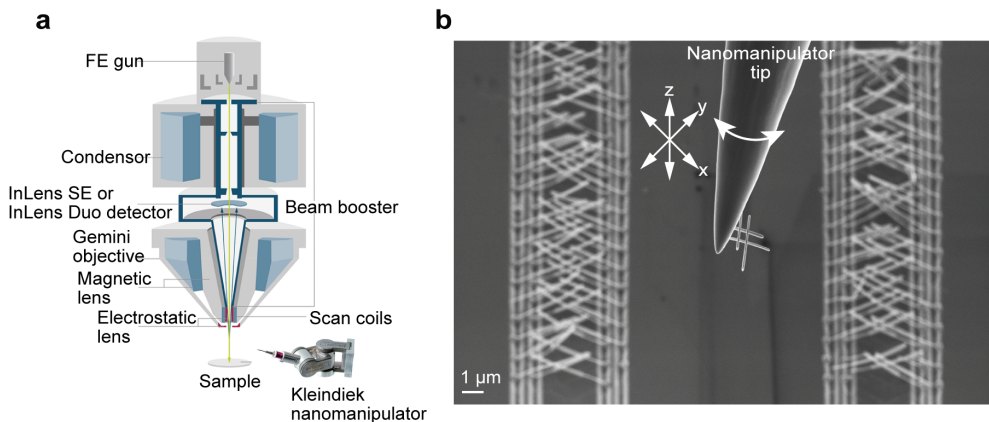
Figure 3.4 | SEM microscope with nanorobot. a, Schematic cross-section of the Zeiss Gemini optical column[4] with Kleindiek nanomanipulator.[5] **b,** SEM image of a field with nanowire networks and the tip of nanomanipulator with "flying hashtag". The arrows represent possible XYZ motion and rotation of the nanomanipulator tip.

Due to our interest in absolute control of physical manipulations of structures at the nanometer scale, our Zeiss SEM microscope[4] is equipped with a Kleindiek

nanomanipulator[5]. A nanomanipulator is a piezoelectric system that allows for XYZ motion as well as 360° rotation of the tip. Because of the nanowire dimensions, the SEM electron beam often causes charging effects that are not possible to control. The electrostatic effects can influence the nanomanipulation. Consequently, it is important to ground the nanomanipulator tip and reduce these effects. Depending on the desired experiments, various changeable end-tips can be mounted. On Figure 3.4b, an SEM image of the nanomanipulator tip with nanowire "hashtag" structure overhanging the field with nanowire networks is shown. Because of the narrow tip size and good resolution of the SEM, one can pick up the nanostructure and accurately place it on the desired device substrate with complicated electrically required openings, local bottom gates for instance. A video document of the nanowire network manipulation performed in the TU/e lab is available in Reference 6.

3.2.2 *Transmission electron microscopy (TEM): Imaging and challenges*

In contrast to the SEM, where secondary or back-scattered electrons are detected, in the TEM the transmitted electron beam is used to create the image. TEM is a powerful technique, that allows for obtaining structural and crystallographic information of materials down to atomic resolution. As a matter of fact, it is a fundamental tool for nanowire-related research. Since nanowires are often used as templates for the growth of different lattice-mismatched heterostructures (radially or axially) or with switching phase domains, zincblende (ZB) or wurtzite (WZ), for the purpose of engineering the final material properties, accurate TEM imaging can often be very challenging. Therefore, it is important to mention challenges and crucial imaging modes that are used to obtain information from different nanowire-based samples.

To acquire TEM images in this thesis, a JEOL ARM 200F TEM operating at a 200 kV acceleration voltage was used. This microscope offers two operation modes: parallel beam for conventional TEM and convergent beam for scanning TEM (STEM). In this subsection, the sample will be referred to as a specimen.

Fundamentals of TEM imaging lays in the different electron scattering phenomena that occur when the electron beam interacts with the specimen. If we consider the particle nature of electrons, we can distinguish elastic and inelastic scattering, and for the wave nature coherent and incoherent scattering. A very special form of elastic scattering is diffraction. Diffraction is important for crystalline nanowires. The operation modes of the TEM considering peculiar electron scattering phenomena will be discussed.

Two distinct imaging modes in a TEM are bright field (BF) and dark field (DF) imaging. By using an objective aperture, one can select the direct beam (BF) or one of the diffracted beams (DF) of electrons combined with carefully selected diffraction conditions. While crossing over the specimen, the electron wave can change both its amplitude and its phase providing image contrast.[7] Imaging conditions are often

chosen in a way that only one, *amplitude* or *phase*, contrast mechanism dominates. *Amplitude contrast* can be mass-thickness contrast and diffraction contrast as it originates from the variations of both mass (Z-number) and/or thickness of the specimen. The former, mass-thickness contrast, emerges from incoherent (Rutherford scattering), while the latter, diffraction contrast, emerges from coherent (Bragg scattering) elastic scattering of electrons. *Amplitude contrast* is obtained when a single beam is selected using the objective aperture, primely when imaging in TEM, BF, DF and STEM mode.

BF imaging is a basic and the most common method used to create a TEM image. Here, the intensity distribution of the direct beam constitutes the image. When imaging in BF mode, regions of the specimen that are thicker or have a higher Z-number, hence the mass, will appear dark, while the regions around the specimen will appear bright. This mode allows imaging nm-scale details, and details such as dislocations. However, sometimes crystalline films/grains of heavy elements will appear dark due to their high mass and imaging details in BF mode are reduced. That is where the DF mode becomes more convenient.
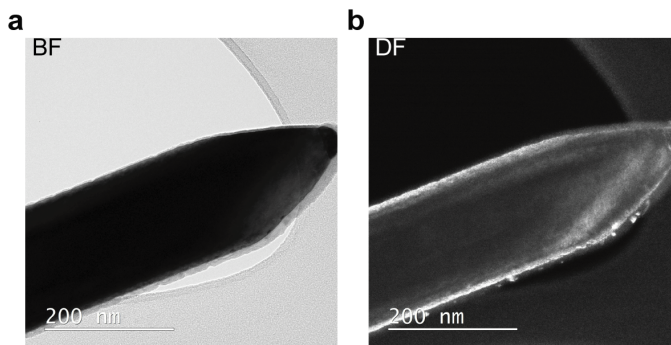
Figure 3.5. | **Bright field (BF) and dark field (DF) TEM images.** TEM BF and DF images of the same area of an InSb nanowire covered with a thin (~10 nm), crystalline film of Al. In the BF image **a,** InSb nanowire and Al crystalline grains appear with dark contrast. In addition, thickness contrast occurs: areas with Al close to the edge of the nanowire are thinner and thus appear brighter. In the DF image, **b,** some of the crystalline Al grains appear with bright contrast, namely the ones whose diffracted beams partially pass the objective aperture.

DF images are recorded using only diffracted beams. To be able to distinct diffraction patterns from different parts of the specimen, a selective area aperture is used. After the crystal information is identified, one or more differently diffracted beams from the recorded diffraction pattern can be selected by placing a small objective aperture in the back focal plane of the objective lens. After that, DF images are recorded, and areas that diffract to the specific location of the objective aperture will appear bright in the image, while non-diffracted areas will appear dark. Depending on the crystal structure and the specimen orientation, the diffraction pattern will be different and will have different intensities. The useful information that is present in DF images is, *e.g.* details about planar defects, stacking faults or

sizes of crystalline particles because it allows us to pick out individual grains. Also, considering that we are in the right zone-axis, we can use DF imaging to distinguish where different domains, ZB or WZ, are present since they have different diffraction patterns. Examples of BF and DF images are shown in Figure 3.5.

Additionally, many different techniques can be employed within a TEM depending on whether elastic or inelastic electron scattering takes place, or whether the phase of the collected electrons is coherent or incoherent. We can have: high-resolution TEM (HR-TEM), selected area diffraction (SAED), and high angle annular dark field (HAADF) scanning TEM (STEM) with energy-dispersive X-ray spectroscopy (EDX).

High resolution TEM

As discussed earlier, both *amplitude* and *phase* contrast may contribute to the image. The application of *amplitude contrast* is briefly explained when discussing TEM imaging. *Phase contrast* arises as a result of interference of different phases of many electron waves scattered by the specimen. Although it can be present in low resolution images, *phase contrast* allows for high resolution imaging as it requires the selection of more than one beam. In general, the more beams collected, the higher the resolution of the image.[7] For that reason, *phase contrast* is the basis for HR-TEM imaging. HR-TEM is used to find more details on the crystal structure, whereas the TEM mode gives more information on morphology and texture of the specimen. After identifying the diffraction pattern of a specimen, the information is used to tilt the sample to a specific zone-axis to be able to perform a HR-TEM. The contrast in HR-TEM is formed as the interference between sets of diffracted beams which corresponds to certain crystallographic planes or sets of crystallographic planes and thus reveal information of crystal lattices, particularly on imperfect structures, such as interfaces and dislocations in the specimen.[8]
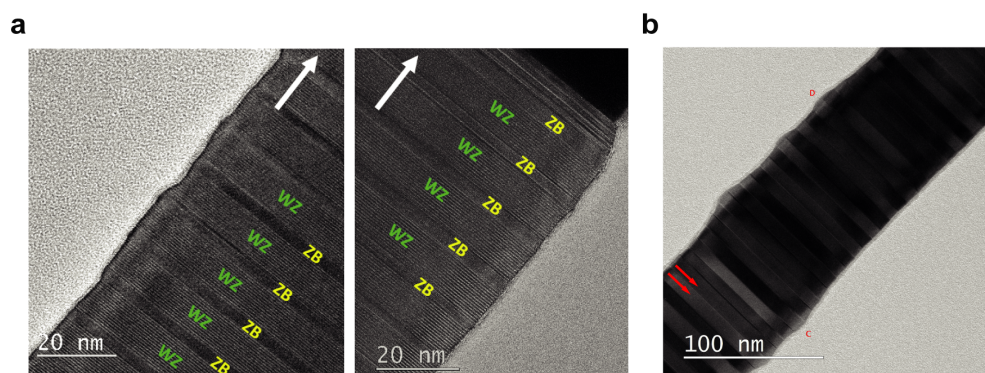
Figure 3.6. | **Superlattice GaP and InP nanowire growth.** HR-TEM images of **a,** GaP nanowire showing a superlattice (13 ZB/WZ segments). The arrow indicates the growth direction.[9] **b,** GaP superlattices in a bent nanowire.

It is often important to show defect-free and atomically sharp interfaces between different phases of the crystal.[9-11] Using the HR-TEM mode, one can resolve different segments, identify different crystal phase domains and determine the thickness. An HR-TEM image of a GaP nanowire superlattice is shown in Figure 3.6. High imaging resolution allows to easily identify different crystal domains. However, when imaging such a structure, there are a number of challenges that can occur. For instance, difference in the diffraction contrast can arise due to the thickness effect or to the specimen bending effect.[7] In case of bending, the diffracting planes tilt relative to the beam, and as a result the contrast changes. Notice, in Figure 3.6b due to the specimen bending, marked with red arrows, equal contrasts of opposite domains are acquired. To interpret changes in an image contrast we need to understand how the contrast is related to the bending. The effect in Figure 3.6b arises due to a local zone-axis orientation variation along the wire with respect to the direction of the incident electron beam. Since the optimal zone-axis orientation of the nanowire varies along the length of the nanowire, it is necessary to re-align the nanowire when imaging each domain in order to obtain atomic resolution.

Selected area electron diffraction pattern

Selected area electron diffraction (SAED) is the technique within a TEM used to obtain site-selective diffraction patterns of the specimen. It is "selected" because the operator decides from which part of the specimen to obtain the diffraction pattern. An aperture hole is brought to the section of the specimen that is of interest. By this means, only a small fraction of the diffracted electron beam passes through the aperture hole and the SAED patterns are recorded. The patterns obtained are a projection of the reciprocal lattice, with lattice reflections showing as sharp diffraction spots. In case of diffraction by a single crystal, a pattern of diffraction spots is obtained. Otherwise, for a polycrystalline specimen, the diffraction pattern results in continuous rings. SAED is an essential tool prior to setting up DF imaging conditions. In the nanowire field, SAED is a powerful technique to identify the local phases of crystalline materials.[12] Using SAED the nanowire growth directions can be determined. Also, we can identify the crystal and its orientation with respect to both the beam and to any adjacent crystals, see Figure 3.7. Typically, the area size of the specimen selected by SAD aperture is 0.5-1 µm.

3
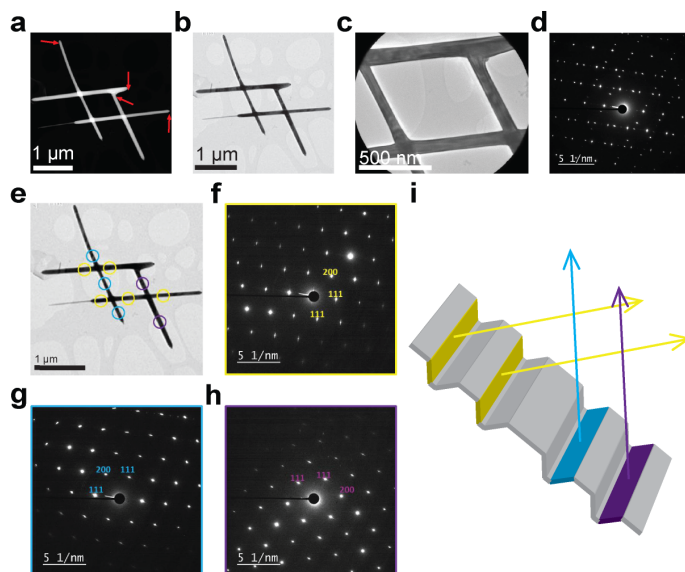
Figure 3.7 | Structural analysis of a "hashtag" nanowire. a, High-angle annular dark field (HAADF) scanning TEM image of the hashtag. The red arrows indicate the positions of the gold catalyst particles. For one wire, the InP stem is present and recognizable. **b,** Corresponding BF TEM image. **c,** BF TEM image displaying the central part of the hashtag as well as the 1.3 μm aperture inserted for the selected area electron diffraction (SAED) pattern displayed in **d**. The pattern represents a superposition of three twin-related ⟨110⟩ zone-axis patterns. **e,** To reveal the orientation of the individual wires of the hashtag, SAED patterns for all the wires were acquired, using a smaller SAED aperture diameter of 0.25 μm. Three different ⟨110⟩ zone-axis patterns were recorded. The color coding of the apertures in e corresponds to the SAED patterns in **f–h**. **i,** Schematic representation of the formation of the hashtag presented in the TEM images.[13]

Scanning TEM

Besides HR-TEM, high resolution imaging can also be accomplished in STEM mode. Here, the coherent beam is condensed to form an incoherent probe that is scanned across the specimen. To create an image in this mode, the back focal plane of the objective lens is projected to a detector. Many different detectors can be employed: bright field (BF), dark field (DF), annular dark field (ADF) and high-angle ADF (HAADF). The detector used in this thesis was an HAADF detector. The HAADF detector collects the electrons incoherently scattered to very high angles where the contribution from diffraction contrast (Bragg scattering) decreases. When imaging in HAADF-STEM mode, the image contrast originates from the mass-thickness contrast. When the thickness variation of the specimen is negligible, the contrast depends only on the Z-number. In atomic resolution HAADF-STEM mode this contrast can be used to distinguish the elements, *i.e.,* the heavier atoms will have a stronger and brighter signal than the lighter ones. Challenges when imaging in this mode are: It is hard to distinguish the elements with close atomic numbers and differences in local thickness change the contrast of the image. Examples of HAADF-

STEM images are shown in Figure 3.8 where a VLS-grown InSb nanowire with a Au catalyst particle is analyzed.
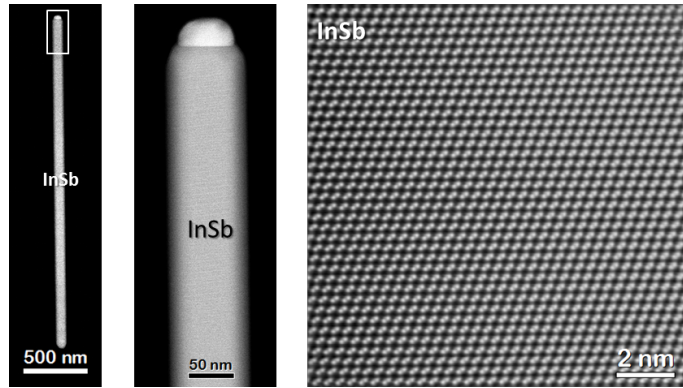
Figure 3.8 | TEM/high angle annular dark field (HAADF) image of a defect free InSb nanowire grown in the MOVPE reactor at TU/e laboratories. The nanowire is analyzed in the [110] zone-axis to show the pristine zincblende (ZB) crystal structure. Nanowires grow along the [111]B direction.[14]

Cross-sectional TEM and energy-dispersive x-ray spectroscopy

The transparency of the specimen to the electron beam is a very important parameter when performing TEM imaging. If the specimen is too thick, the TEM information will be reduced and often the analysis is not even possible. Also, for the analysis of core-shell structures the information about the interfaces is desired. To allow for imaging of such structures one can use a focused ion beam (FIB) to cut structures into thin lamellas, such that they are thin enough to be observed in a TEM. Cross-sectional analysis facilitates to record the faceting and to observe the inner structure of the shell. The downside of the cross-sectional analysis is that it is time consuming and requires a lot of difficult preparation steps and the experiment is performed only to a particular part of the sample cross-section.
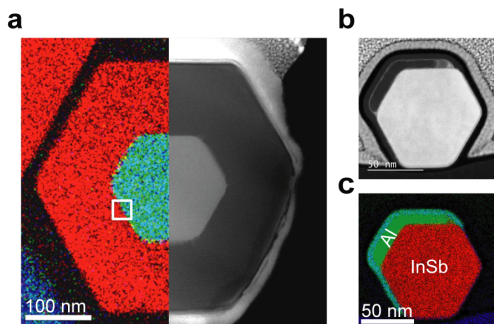
Figure 3.9 | HAADF-STEM image of a nanowire cross-section with an EDX chemical composition map. a, HAADF-STEM and EDX overlapped images of a cross-sectional lamella of one representative GaP/Si core/shell nanowire.[15] **b,** HAADF-STEM image of the nanowire cross-section with crystalline Al covering two out of six nanowire facets. **c,** EDX compositional map of the cross-section in **b**. The Al–InSb interface is oxygen-free.

When using the microscope in HAADF-STEM mode, elemental analysis can be performed. This is done using energy-dispersive x-ray spectroscopy (EDX), as shown in Figure 3.9. X-rays emitted by the specimen under the influence of the

electron irradiation are detected as an energy spectrum. The spectrum of peaks is qualitatively analyzed with EDX software. However, the peaks of some elements are very close in energy and accurate peak identification can be difficult. A quantitative EDX analysis can be performed by analyzing an area or line over a longer time. Note that sometimes, the area of the specimen that is exposed to the focused electron beam for a longer time may be damaged. We use the EDX data to get information about the chemical composition, whether the interface is abrupt, *etc.*

In-situ TEM

It is very appealing for a researcher working with epitaxy to be able to follow the growth of a crystal in real time, and observe its dynamics with high spatial and temporal resolution.[16] Over the past decade *in-situ* applications of TEM became more accessible for understanding the growth of nanoscale materials, especially nanowires. Most recent results emerging from in situ transmission electron microscopy revealed the growth of nanowire structures and importantly the *in-situ* growth dynamics of the VLS mechanism are demonstrated.[11,17-19] The importance of this technique is mainly to enhance microscopic understanding of the growth mechanism. There are different variations to an *in-situ* TEM instrument. *In-situ* TEM (STEM) experiments presented in Chapter 5 of this thesis are performed on an FEI Titan Themis that operates at 200 kV. For this work, a commercial DENSsolution six contact double tilt TEM holder is used with a through hole heater chip allowing for *in-situ* heating experiments.

Imaging induced damage

Imaging nanowire specimen for an extended period with a highly intense beam may result in beam-induced "defects" in the specimen as illustrated in Figure 3.10 where an InSb nanowire with an Al layer is imaged. After long beam exposure the formation of "voids" and possible delamination in the Al layer is observed where the InSb nanowire stays intact. Hence, care has to be taken with beam sensitive materials and proper imaging conditions, such as lowering the acceleration voltage (kV) or the beam current, should be chosen.
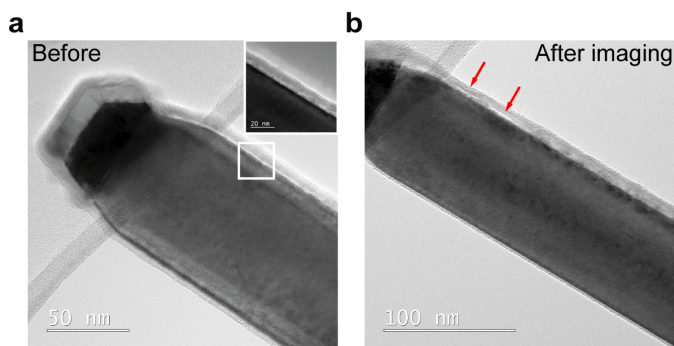
Figure 3.10 | Long "high beam" exposure. (HR)TEM image of an InSb nanowire covered with a thin (~10 nm), crystalline film of Al showing the Al layer **a,** at the beginning and **b,** after long imaging the formation of "voids: in the Al layer is visible. The image is taken along the <112> zone-axis.

3.3 Low temperature measurements and devices

The core purpose of the experiments in this dissertation is to find "smoking gun" evidence for the existence of Majorana states, which requires high quality materials and interfaces. However, the exotic quantum effects in nanostructures are expected to be apparent only at temperatures way below 1 K. For this reason, it is essential to perform the measurement in a setup that can reach cryogenic temperatures at which electrical measurements are still possible while reducing the noise of the environment.

For the transport measurements in this dissertation ^{3}He/^{4}He cooled cryostats are used with base temperatures down to 20 mK. Details on the measurements performed in different setups are enclosed in appendices of the respective experimental chapters separately. The advantage of a dilution refrigerator is stable operation at low temperatures, which enables interesting experimental quantum physics.

To measure different quantum phenomena in InSb nanostructures, four main fabrication steps are made before the final device is realized:

- Step I, the nanowire sample and nanowire device sample is grown by metal-organic vapor phase epitaxy (MOVPE) or molecular beam epitaxy (MBE) in the cleanroom and laboratory of NanoLab @ TU/e and UCSB, respectively (see Chapters 4-7).

- Step II is performed in the Kavli Nanolab Delft, where the device chips with bitmarkers, metallic structures on the chip used to locate nanowires, are processed by means of e-beam lithography followed by the deposition or etching and resist liftoff. The substrates used for the device samples are p-doped silicon (Si) covered with 285 nm thick layer of SiO$_2$. The heavily doped Si is used as a global backgate. The experiments in Chapters 4-7 employ such a global backgate.

- Then, in step III, the nanowire or nanowire device nanomanipulation from the growth chip to the device chip is performed at NanoLab @ TU/e. For this purpose the SEM Zeiss microscope is equipped with the Kleindiek nanomanipulator. See Subsection 3.2.1 of this chapter for details about the tool.

- Finally, in step IV, normal contact and top/side gates are defined using several e-beam lithography steps followed by the metal evaporation. To have a reliable contact with the nanowire, prior to contacting, an additional step is required in order to remove the native oxides from the nanowire or nanowire device. This is done using either wet chemical (ammonium sulfide solution[20]) or *in-situ* dry etching methods (argon or helium milling). The contact deposition recipes differ for various nanostructures grown in the work of this thesis and will be presented separately in Chapters 4-7. Top/side gates are used for the fabrication of the Majorana device in Chapter 5. The advantage of top gates is potentially stronger coupling to the nanowire in comparison to the local bottom gates fabricated on the device chip.

3.4 References

1   Herman, M. A., Richter, W. & Sitter, H. in *Epitaxy: Physical Principles and Technical Implementation*   171-200 (Springer Berlin Heidelberg, 2004).

2   Stringfellow, G. B. *Organometallic vapor-phase epitaxy: theory and practice*. (1999).

3   Borg, M. *Antimonide Heterostructure Nanowires - Growth, Physics and Devices* Doctoral thesis, Lund University, (2012).

4   Zeiss. *Gemini Optics*, https://www.zeiss.com/microscopy/us/products/scanning-electron-microscopes/sigma.html.

5   Kleindiek Nanotechniek. *Micromanipulator for Electron Microscopy*, https://www.nanotechnik.com/.

6   Fadaly, E. M. T. *et al.* Observation of Conductance Quantization in InSb Nanowire Networks. *Nano Letters* **17**, 6511-6515, doi:10.1021/acs.nanolett.7b00797 (2017).

7   Williams, D. B., Carter, C. Barry,. *Transmission Electron Microscopy: A Textbook for Materials Science*. Second edn, (Springer, 2009).

8   Spence, J. C. H. *Experimental high-resolution electron microscopy / John C.H. Spence*. (Clarendon Press ; Oxford University Press, 1981).

9   Assali, S. *Pure crystal phase nanowires : growth and optical properties* Doctoral thesis, Technical University of Eindhoven, (2015).

10   Algra, R. E. *et al.* Twinning superlattices in indium phosphide nanowires. *Nature* **456**, 369, doi:10.1038/nature07570 (2008).

11   Jacobsson, D. *et al.* Interface dynamics and crystal phase switching in GaAs nanowires. *Nature* **531**, 317, doi:10.1038/nature17148 (2016).

12   Ding, Y., Fan, F., Tian, Z. & Wang, Z. L. Atomic Structure of Au−Pd Bimetallic Alloyed Nanoparticles. *Journal of the American Chemical Society* **132**, 12480-12486, doi:10.1021/ja105614q (2010).

13   Gazibegovic, S. *et al.* Epitaxy of advanced nanowire quantum devices. *Nature* **548**, 434, doi:10.1038/nature23468 (2017).

14   Arbiol, J., de la Mata, M. *Polarity study in III-phosphide and III-antimonide nanowires* (2014).

15   Hauge, H. I. T. *et al.* Hexagonal Silicon Realized. *Nano Letters* **15**, 5855-5860, doi:10.1021/acs.nanolett.5b01939 (2015).

16   Jacobsson, D. *Crystal Structures in GaAs Nanowires: Growth and Characterization* Doctorate thesis, (2015).

17   Wen, C. Y. *et al.* Periodically Changing Morphology of the Growth Interface in Si, Ge, and GaP Nanowires. *Physical Review Letters* **107**, 025503, doi:10.1103/PhysRevLett.107.025503 (2011).

18   Frances, M. R. Controlling nanowire structures through real time growth studies. *Reports on Progress in Physics* **73**, 114501 (2010).

19   Panciera, F. *et al.* Synthesis of nanostructures in nanowires using sequential catalyst reactions. *Nature Materials* **14**, 820, doi:10.1038/nmat4352 (2015).

20   Suyatin, D. B., Thelander, C., Björk, M. T., Maximov, I. & Samuelson, L. Sulfur passivation for ohmic contact formation to InAs nanowires. *Nanotechnology* **18**, 105307 (2007).

3

4

Chapter

Complex InSb nanowire networks

Abstract *Semiconductor nanowires are ideal for realizing various low-dimensional quantum devices. In particular, topological phases of matter hosting Majorana quasiparticles can emerge when a semiconductor nanowire with strong spin–orbit coupling is brought into contact with a superconductor. To exploit the potential of Majoranas, they need to be exchanged in a well-controlled braiding operation. Essential hardware for braiding is a network of crossed crystalline nanowires. These network structures should be of superior crystalline quality to enable the ballistic electron transport. The growth of nanowire networks based on InSb and InAs was reported before, however the main challenge for the growth of crossed nanowires is in the yield, overall morphology and crystal quality. Here, we develop a technique for bottom-up synthesis of single crystalline InSb nanowire networks with an unprecedented yield of crossed junctions by exposing (111)B facets in (100) substrates and deliberately forcing wires to merge. Accurate control over the nanowire position and growth direction enables us to grow complicated networks of up to four crossed junctions, such as closed loops of four interconnected nanowires (referred to as "hashtags"). The method we develop is generic and can be used to grow nanowire networks of different semiconductor materials. Quantum transport measurements of nanowire "hashtags" reveal Aharonov–Bohm and weak-antilocalization effects, indicating a phase-coherent system with strong spin–orbit coupling.*

4.1 Introduction

To exploit the potential of Majorana quasiparticles—which are key elements of topological quantum computing, they need to be exchanged in a well-controlled braiding operation. Since the first detection of Majorana signatures in hybrid superconductor-semiconductor InSb nanowires,[1] many topological quantum computing schemes are proposed, based on the braiding of these Majorana zero modes in complex hybrid nanowire networks.[2-7] The high crystalline quality of these nanowire networks is important because Majorana quasiparticles require ballistic transport, and defects in the wires and at the interface may induce unwanted disorder. To grow these nanowire networks, a top-down approach, provides high degree of freedom in terms of network structure designing and scalability.[8] However, the large lattice mismatch between InSb and growth substrates highly limits the mobility and thus the feasibility of this method. An alternative approach is bottom-up synthesis of out-of-plane nanowire networks which, owing to their large surface-to-volume ratio, effectively relieve strain on their sidewalls, enabling the growth of monocrystalline nanowires on highly lattice-mismatched substrates.[9-11] Merging these one-dimensional nanowires into network self-assembly, requires highly accurate control of the wire positions with well-defined growth directions to achieve an adequate yield.

Recently, different schemes have been reported for merging InSb and InAs nanowires into networks.[12-17] Unfortunately, these structures are either not monocrystalline, owing to a mismatch of the crystal structure of the wires with that of the substrate (that is, hexagonal nanowires on a cubic substrate),[14] or the yield is low owing to limited control over the multiple accessible growth directions (the yield decreases with the number of junctions in the network).[16] Previous work on the bottom-up growth of InSb nanowire networks were based on the substrate crystallography and nanowire growth directions. The first report on InSb "nanocrosses" explored sliding of the catalyst particle onto one of the side facets of the hexagonal stem nanowire allowing for a InSb nanowire to grow parallel to the

substrate surface in one of the horizontal (111)B directions. If the optimal diameter and density of gold colloids (random deposition) is used, InSb nanowires, growing from different stems, can meet and merge into nanostructures having a T or X shape.[15] The second report focused on a more rationally designed approach towards merging of wires. That is, deliberately kinking the growth direction of stem wires, *i.e.*, from (100) to one of the possible two <111>B growth orientations, followed by the growth of InSb nanowires.[16] In this way, by carefully patterning the substrate using e-beam lithography, InSb nanowires growing in the [11-1] and [-1-1-1] directions could meet and merge into a network forming multiple crossed junctions. Even though the growth and design concepts reported before allow for the growth of nanowire networks the yield of the structures steeply decreases with increasing complexity, and therefore it has not been possible to grow the envisioned structures. Here, we explore a generic bottom-up growth approach to fabricate complex nanowire network structures, in order to have the required flexibility in device design. Our approach is generic and allows to synthesize the complete nanowire network quantum system by a bottom-up process with a great controllability and excellent yield. Nanowire networks are one-dimensional and "free-standing" and therefore lattice matching conditions to the substrate are avoided. Our material of choice is InSb owing to its extreme properties needed to create Majorana zero modes (MZM) fundamental to topological quantum computing. Additionally, since these bottom-up structures are free-standing, three-dimensional epitaxial structures can be realized with large freedom over the substrate material.

4.2 Results

4.2.1 Substrate preparation

Our approach towards the bottom-up growth of nanowire networks is based on controlling the position and growth direction of nanowires. It is well-known that III-V nanowires tend to grow along a (111)B crystal direction. In order to force the wires to grow towards each other and merge, we create a substrate in which trenches are etched in an InP(100) crystal to expose (111)B facets tilted under an angle of 54.7° (see Figure 4.1). Fabrication of substrates with trenches is a three-step e-beam lithography process: First, markers on a (100) InP substrate are fabricated. Markers are used for alignment, which is crucial in the next two steps of the processing. Second, trench structures in the substrate are defined by electron-beam lithography, a reactive ion etch and a subsequent wet or *in-situ* gaseous HCl (in the MOVPE) etch to expose (111)B facets on an InP(100) crystal surface, Figure 4.1.
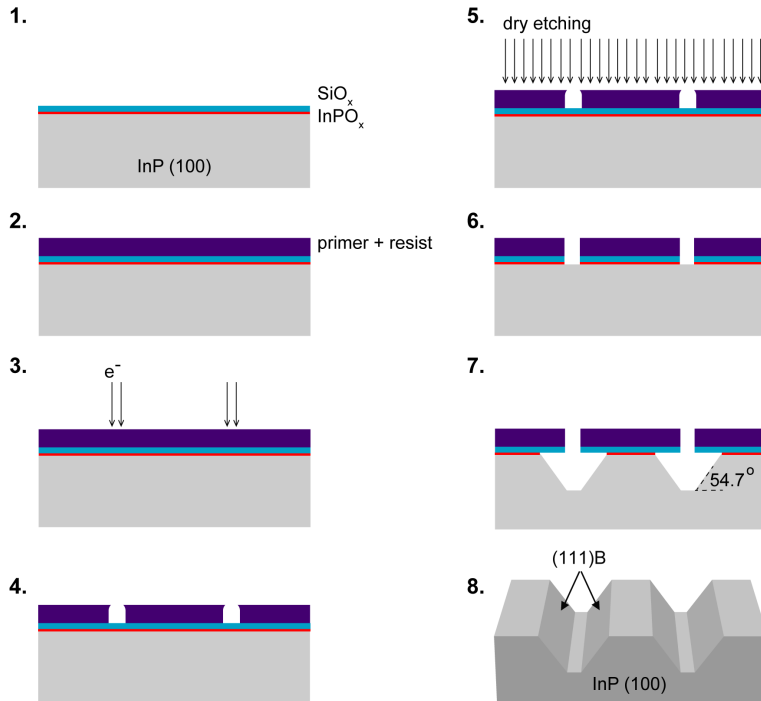
Figure 4.1 | Fabrication of InP substrate with trenches. 1–8: Schematic illustration of the processing steps. **1**, An epiready wafer is etched in 7:1 buffered oxide etch, NH$_4$F:HF=7:1, (BOE); an oxygen plasma step is performed to create a "sacrificial" native oxide layer of 1.9 ± 0.1 nm (see Reference 18); a 20 nm SiO$_x$ hard mask is deposited followed by another oxygen plasma treatment. **2, 3, 4,** The electron-beam primer and resist layer are spun; rectangular windows of ~200 nm are written using e-beam lithography and subsequently developed. **5, 6,** The hard mask is etched using reactive ion etching (RIE) with CHF$_3$ and Ar. **7, 8,** The wet etch in HCl (37%):H$_3$PO$_4$ (85%) with 5:1 ratio or in-situ MOVPE gaseous HCl etch is performed to expose (111)B facets in InP (100) and the hard mask is removed using 7:1 BOE.

Third, gold (Au) particles with varying diameter from 10 – 50 nm, crucial for an optimized crossing process and a yield, are defined (positioned) on the inclined facets, which catalyze nanowire growth via the vapor–liquid–solid (VLS) mechanism, as shown in Figure 4.2. Details on the substrate preparation are in the Appendix 4.4.1 of this chapter.
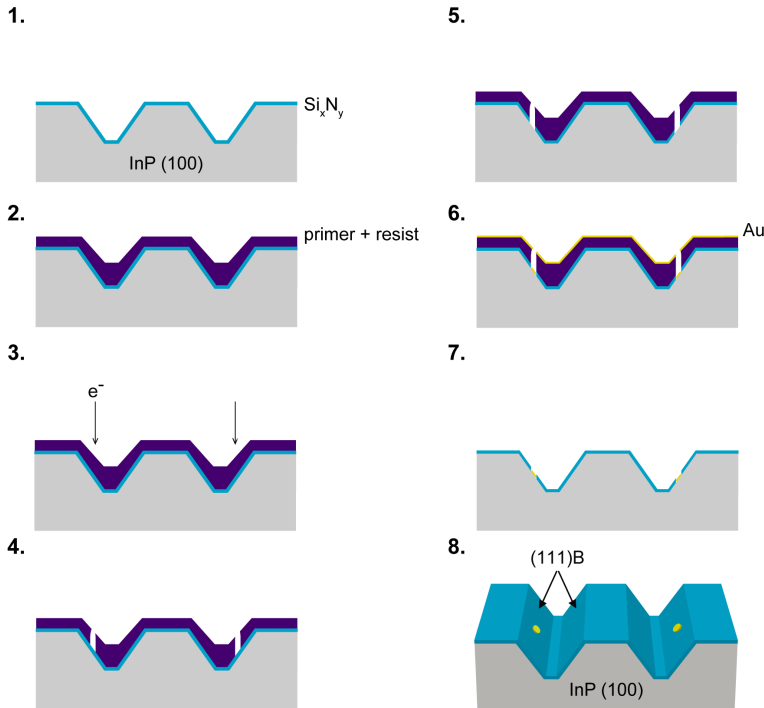
Figure 4.2 | Catalyst deposition. 1–8: Schematic illustration of the processing steps. **1**, 20 nm Si_xN_y mask is deposited followed by an oxygen plasma treatment. **2–4**, E-beam primer and resist layer is spun (nominal resist thickness needs to be half of the depth of the trenches); arrays of dots (10–50 nm) are written on inclined (111)B facets using e-beam lithography and the resist is then developed. **5**, Openings in the Si_xN_y mask are defined using a short 20:1 buffered oxide etch (BOE). **6–8**, 10 nm of gold is evaporated through the opening in Si_xN_y mask followed by a lift-off.

4.2.2 Growth of InSb nanowire networks

To facilitate nucleation of the InSb wires, first an InP stem wire is grown. InP nanowires, were grown at 450°C for 19 minutes using *trimethyl*-indium (TMIn), phosphine (PH$_3$) and HCl (1%) with precursor molar fractions $\chi_{TMIn} = 7.6 \times 10^{-6}$ and $\chi_{PH3} = 9 \times 10^{-3}$ and $\chi_{HCl} = 8.3 \times 10^{-6}$. HCl was used to suppress unwanted sidewall growth. Further, InSb nanowires were grown at 495°C using TMIn and *trimethyl*-antimony (TMSb) with precursor molar fractions $\chi_{TMIn} = 2.8 \times 10^{-7}$ and $\chi_{TMSb} = 5.1 \times 10^{-5}$, for 35 minutes. For both processes, the reactor pressure was 50 mbar, with a total flow of 6000 sccm and H$_2$ was used as a carrier gas.
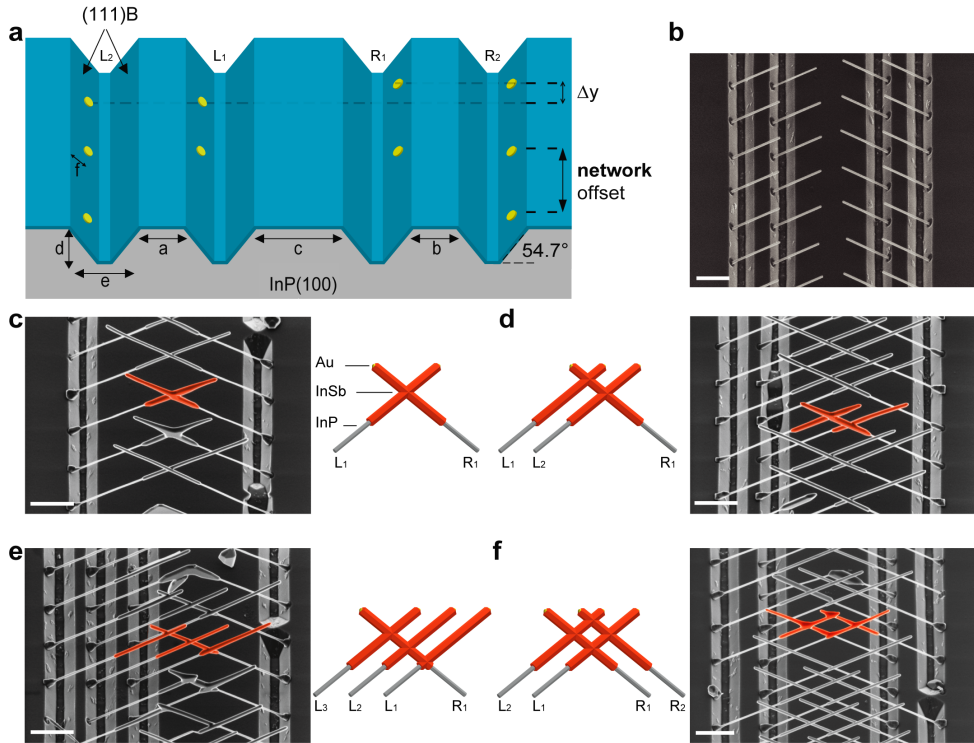
Figure 4.3 | Deterministic growth of InSb nanowire networks. a, Schematic illustration of the substrate with etched trenches. Gold catalysts are lithographically defined on the inclined facets. The offset between the catalyst particles (Δy) is critical for the realization of nanowire networks and shadowed superconducting islands (see Chapter 5 for superconducting islands). The size and the symmetry of the networks are controlled by the dimensions of the trenches indicated in the schematic: the spacing between the left–left (L_1, L_2), a, right–right (R_1, R_2), b, and left–right (L_1, R_1) trenches, c, as well as the trench depth, d, width, e, and position of the gold particles on the inclined facets, f. **b**, A scanning electron microscopy (SEM) image of InP nanowires which serve as stems for InSb nanowire growth. **c–f**, SEM images and schematic illustrations of accomplished nanowire structures having one junction (**c**), two junctions (**d**), three junctions (**e**) or four junctions (**f**; hashtag). All SEM images are taken at 30°-tilt. All scale bars are 1 μm.

Owing to the geometry of the (111)B facets, InP stem nanowires are forced to grow towards each other. From Figure 4.3b it is evident that the yield of the InP nanowires is very high. InSb follows the growth on InP stems and can fuse into a network. The final size and symmetry of the networks are controlled by the dimensions of the trenches and the spacing between them, that is, the parameters a–f, as indicated in Figure 4.3a and demonstrated later in Figure 4.4. The left (right) trenches and wires grown from them are labelled L_1, L_2 (R_1, R_2). The offset (Δy) between the gold particles is an important parameter to control because it determines the distance between the cores of the wires. If $\Delta y < D$, where D is the nanowire diameter, nanowires will merge during growth (specifically, for $\Delta y \approx 0$ ($\Delta y \leq D$), resulting in the formation of a T-junction (X-junction)[16]); otherwise, $\Delta y > D$ enables shadow growth of the superconducting islands, which will be discussed in the Chapter 5.

The optimum offset for forming a crystalline junction is 30 – 50nm for wires grown from a 30 nm diameter catalyst particle. Due to this offset the resulting structures are not planar, as shown in Appendix Figure 4.10. Figure 4.3b shows a uniform array of InP nanowires which are used as stems to facilitate uniform nucleation of InSb nanowires. When InSb nanowires (highlighted in red in Figure 4.3c-f) are grown on top of these InP stems, nanowire networks with 1-4 wire-wire junctions are formed, depending on the trench design. The number of wire-wire junctions can be increased by fabricating a larger number of left and right trenches.

We further vary parameters *a* and *b* on the abovementioned trench design and grow nanowire networks with four junctions referred to as "hashtags". Hashtag structures spanning different areas are realized as apparent from the Figure 4.4. In order to perform the braiding operations, Majorana quasiparticles need to be exchanged without being brought in close proximity to ensure that the system stays in the degenerate ground state. Hence the size of the system should obey the Majorana requirements.

4
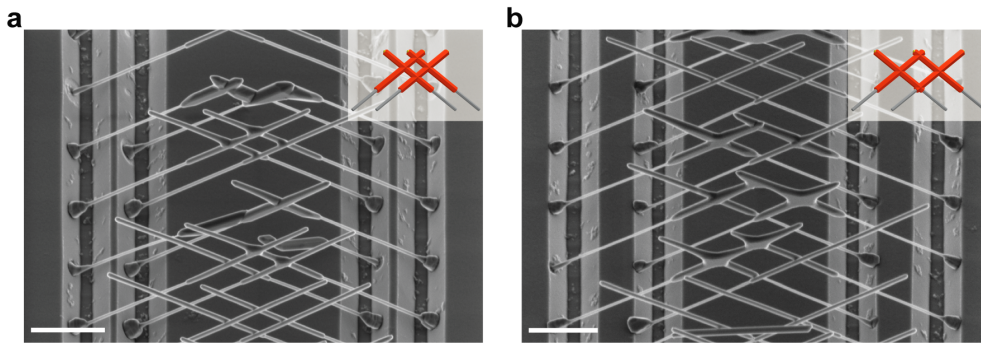
Figure 4.4 | Lithographic control over the trench design layout enables growth of hashtags spanning different loop areas. a, b, InSb nanowire networks grown on trenches with different spacing between the left–left (L_1, L_2) and right–right (R_1, R_2) trenches, labelled *a* and *b* in Figure 4.3a, respectively. Control over the dimensions of the trenches allows us to tune the length of the hashtag parallelogram. The scale bars are 1 μm.

We investigated the role of the Si_xN_y mask for the growth of InSb networks since we know that concave edges of the trenches may act as a preferential nucleation site for InSb growth. Our observations are shown in Figure 4.5. Thin-film InSb growth is in direct competition with InSb nanowire growth, resulting in short nanowires and a very low yield of crossed junctions[10], Figure 4.5a. By covering the substrate with a Si_xN_y mask, the growth is restricted to areas where the InP substrate is exposed.[19] This, in combination with approximately 100 times lower molar fractions of TMIn and TMSb used for the growth of wires shown in Figure 4.5b, eliminates the unwanted InSb layer growth and allows for growth of high-aspect-ratio InSb nanowires which merge into networks.
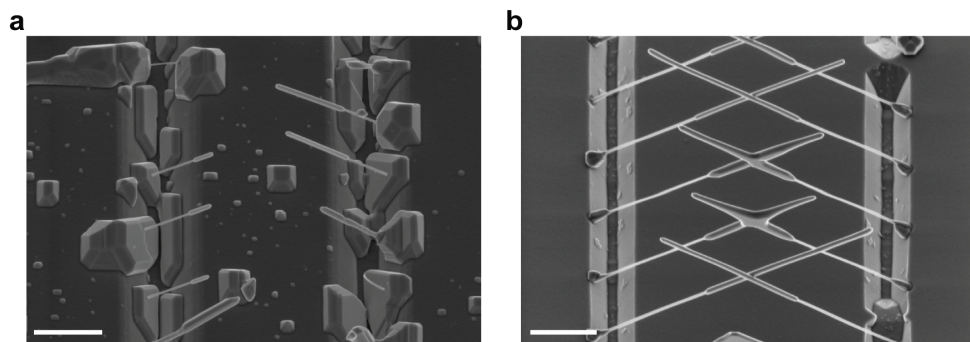
Figure 4.5 | Role of the Si$_x$N$_y$ mask in InSb nanowire growth. a, b, A 30°-tilted SEM image of InP–InSb nanowires grown on a substrate without, **a**, and with, **b**, Si$_x$N$_y$ mask. A substantial amount of parasitic thin film growth is observed in **a**. Both scale bars are 1 μm.

We fabricated a substrate with a larger number of left and right trenches and increased the growth time of the InSb nanowires. The growth on these trenches results in structures up to 9-junctions that are promising for the single qubit device,[5] Figure 4.6. The challenge here is in the yield of these structures that is determined by the InP stem endurance to the long growth time.
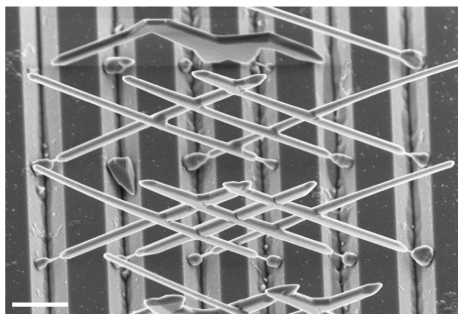
Figure 4.6 | The growth of a qubit device. A 30°-tilted SEM image of InP–InSb nanowire qubit networks made of up to 9-crossed InSb nanowires. The scale bar is 1 μm.

4.2.3 "Hashtag" structural quality check

We know that InSb nanowires and nanowire networks have a zinc blende crystalline structure.[16] However, due to the growth of InSb nanowires on top of stem nanowire that is full of rotational twin boundaries there is a possibility to form a grain boundary at the junction between two InSb nanowires. To investigate the crystallographic orientation relationship between 4 crossed nanowires, a "hashtag" was taken from a substrate and deposited on a holey carbon film using a manipulator in the SEM. Next, the structures were imaged in bright field TEM (BF TEM) mode using selected area electron diffraction (SAED). The resulting pattern of 4 junctions demonstrating a superposition of three twin-related <110> zone axes is shown in Figure 4.7d. The colored circles represent the area where SAED patterns

were acquired (Figure 4.7e). The colors correspond to the different wire orientations schematically illustrated in Figure 4.7i.
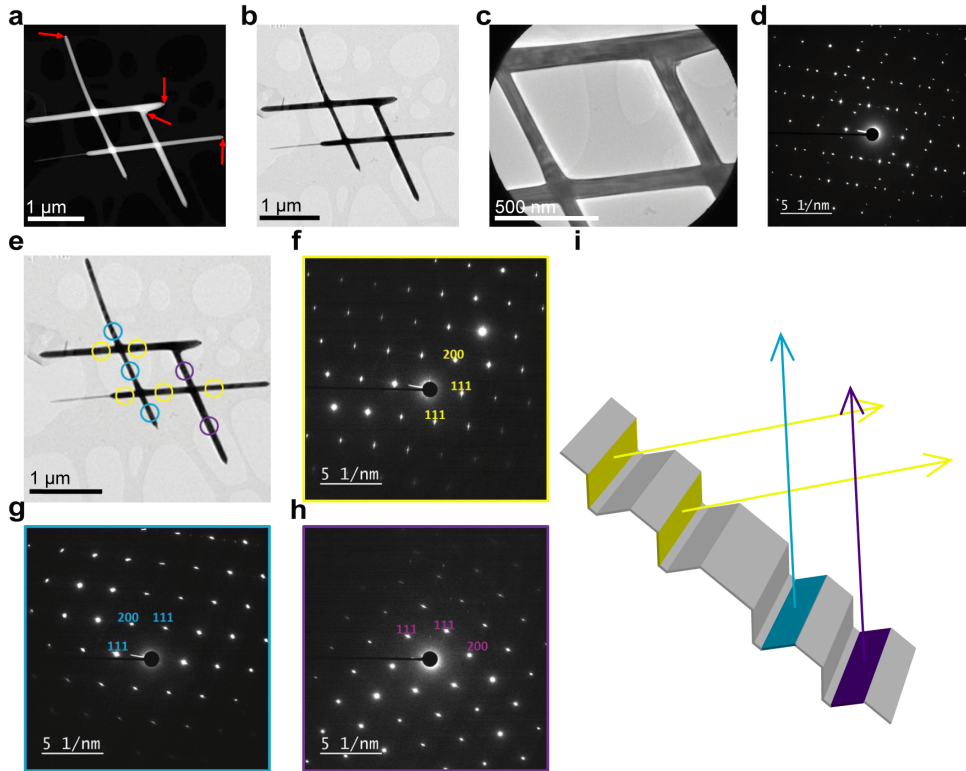
Figure 4.7 | Structural analysis of a "hashtag". a, High-angle annular dark field (HAADF) scanning TEM image of the hashtag. The red arrows indicate the positions of the gold catalyst particles. For one wire, the InP stem is present and recognizable. **b,** Corresponding BF TEM image. **c,** BF TEM image displaying the central part of the hashtag as well as the 1.3 μm aperture inserted for the selected area electron diffraction (SAED) pattern displayed in **d**. The pattern represents a superposition of three twin-related ⟨110⟩ zone axis patterns. **e,** To reveal the orientation of the individual wires of the hashtag, SAED patterns for all the wires were acquired, using a smaller SAED aperture diameter of 0.25 μm. Three different ⟨110⟩ zone axis patterns were recorded. The color coding of the apertures in **e** corresponds to the SAED patterns in **f**–**h**. **i,** Schematic representation of the formation of the hashtag presented in the TEM images.

The analysis shows that blue and purple nanowires have two different orientations, related by a 180° rotation around their long axis. Thus, one of the wires has the same orientation as the substrate wafer, while the other one is twin related. The two yellow wires have identical orientations that differ from the orientations of the two other wires. Thus, these yellow wires are also twin-related to the substrate, though their rotation axis is different from that of the blue and purple wires. TEM imaging of a "hashtag" structure confirms the high crystalline quality of the InSb nanowire junctions.

4.2.4 Aharonov-Bohm oscillations in InSb "hashtags"

Phase-coherent transport is a basic requirement for certain measurement-based braiding schemes which make use of an interferometric readout.[6,7] This interferometer requires tuning towards a maximum amplitude of Aharonov–Bohm (AB) oscillations. The AB effect[20] is induced by coherent interference of electron waves. Aharonov and Bohm propose that, if a coherent beam of electrons is split into two paths (path 1 and path 2) around a fluxoid the beams would interfere on the other side, Figure 4.8. This is because both parts of the beam have picked up an additional phase caused by the vector potential. Depending on the vector potential the beams will have constructive or destructive interference. The intensity of the current, exiting to the right, oscillates with a period $\Delta B = h/e$. And importantly, the phase of the system will depend on the area of the loop, $A = \Phi/\Delta B$ where $\Phi = h/e$ is the flux quantum.
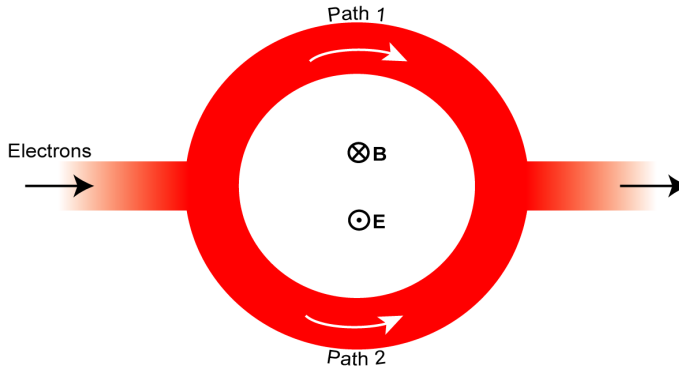
Figure 4.8 | Aharonov-Bohm ring. Schematic of the semiconductor ring structure with an out-of-plane magnetic field. A beam of electrons enters the ring structure on the left, splits into two beams of the ring and recombines on the other, right, side.

To investigate the Aharonov–Bohm effect in our nanowire networks, nanowire hashtags were transferred onto a p-doped Si/SiO_2 substrate and contacted by metal electrodes (Au/Cr, Figure 4.9a left inset). Figure 4.9a shows the magnetoconductance of a representative device (device A). Periodic Aharonov–Bohm oscillations can clearly be seen (Figure 4.8a right inset), as well as a pronounced weak-antilocalization conductance peak at B = 0 T. The weak-antilocalization conductance peak is present in most of the measured hashtag devices, for both in- and out-of plane magnetic field orientations (see Appendix Figure 4.11), indicating a strong spin–orbit coupling in this system. The observed weak-antilocalization effect also suggests diffusive transport in our hashtag devices, since the hashtag length is several times longer than the estimated mean free path, approximately 250 nm for InSb nanowires.[21,22] The period of the Aharonov–Bohm oscillations is extracted from a discrete Fourier transform of the magneto-conductance.
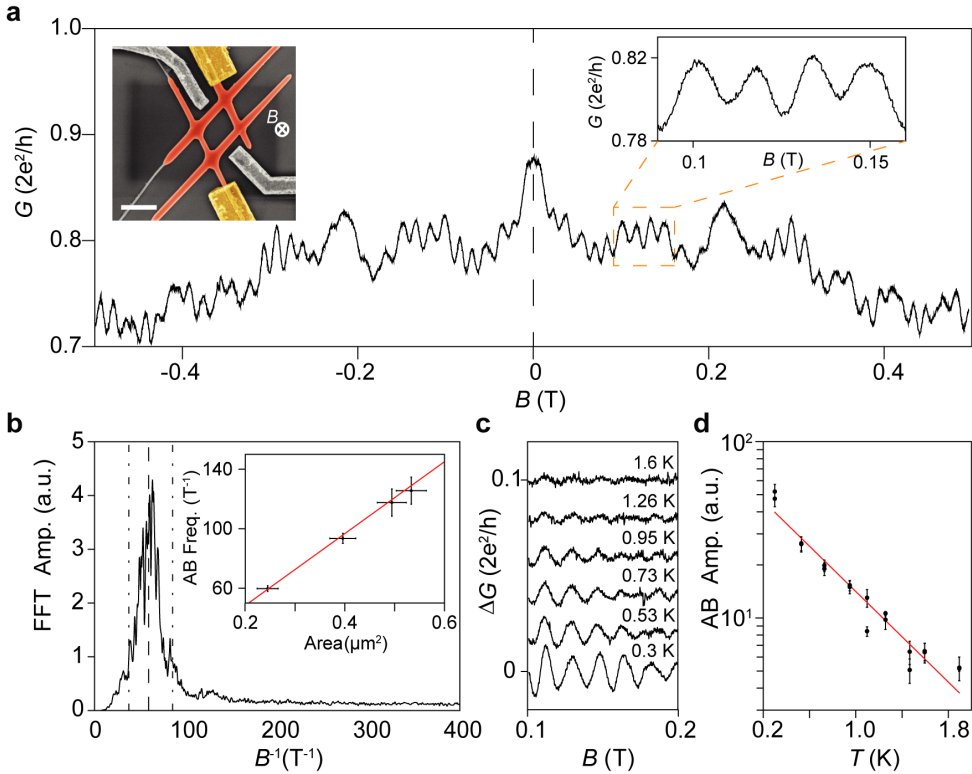
Figure 4.9 | Aharonov–Bohm and weak-antilocalization effects in nanowire hashtags. a, Magnetoconductance of a hashtag shows periodic Aharonov–Bohm oscillations and a weak-antilocalization peak at $B = 0$ T. Inset (left), a pseudo-colored SEM image of the device. An InSb hashtag (red) is in contact with normal metal electrodes (yellow) and measured in an out-of-plane magnetic field at 300 mK. Scale bar is 500 nm. Inset (right), magnification of the region indicated by an orange rectangle in the main panel, containing four Aharonov–Bohm periods. **b**, FFT spectrum of the magnetoconductance of this device (ensemble averaged), indicating the Aharonov–Bohm (AB) oscillation frequency. The dashed line indicates the expected frequency based on the area calculated from the SEM image, dash-dotted lines indicate the expected minimum and maximum frequencies due to the finite thickness of the interferometer arms. Inset, plot of the peak frequency, assigned from the averaged FFT spectra, as a function of the loop area for four different hashtag devices. The red line corresponds to the expected frequency of an h/e periodic oscillation for a given loop area, (a.u., arbitrary units). **c**, Temperature dependence of Aharonov–Bohm oscillations (background subtracted). The Aharonov–Bohm effect persists up to 1.6 K. Curves are offset vertically for clarity. **d**, Aharonov–Bohm (AB) amplitude as a function of temperature. The red line is a fit to the data, showing an exponential decay of the oscillation amplitude.

Figure 4.9b shows the averaged fast Fourier transform (FFT) spectrum of which the peak frequency (60 T^{-1} with a standard deviation of 2 T^{-1}) corresponds to a period ΔB of 16.7 mT with a standard deviation of 0.6 mT. The effective area (A) calculated from this Aharonov–Bohm period ($A = \Phi/\Delta B = 0.25$ μm^2 with a standard deviation of 0.01 μm^2, where $\Phi = h/e$ is the flux quantum) is in agreement with the measured area of a hashtag loop ($A \approx 0.25$ μm^2 with a standard deviation of 0.02 μm^2). We determine the peak frequency for four different devices with different loop areas

(These devices are presented in the Appendix 4.4.6), showing good agreement with the expected values (Figure 4.9b inset). This agreement between theory and experiment confirms that the observed Aharonov–Bohm oscillations are indeed a result of the quantum interference of electron waves emanating from the two transport channels that constitute the hashtag.

Magnetoconductance traces taken at increasing temperature values are shown in Figure 4.9c. Aharonov–Bohm oscillations persist up to about 1.6 K. The amplitude of the Aharonov–Bohm oscillations decays exponentially with temperature (Figure 4.8d). This exponential behavior, observed in early Aharonov–Bohm experiments with similar loop size,[23] suggests that the phase coherence length is proportional to T^{-1}. Following the method described in Reference 23, we can estimate a phase coherence length on the basis of the suppression slope in Figure 4.9d, to be 0.7 μm with a standard deviation of 0.1 μm at 1 K, which translates to 2.3 μm with a standard deviation of 0.3 μm at 300 mK.

4.3 Conclusion

To summarize, we demonstrate the growth of bottom-up nanowire networks with unprecedented control over envisioned network structure. By careful multi-step e-beam lithography design a completely novel substrate platform is realized. Our substrates allows for the growth up to 9 junctions of InSb nanowires, adequate for engaging in the Majorana qubit devices. We emphasize that the platform developed in this work is generic and can be used to synthesize interconnected nanowires of various semiconductor materials which grow along a <111>B direction.

Phase-coherent transport observed in the network of nanowires is a materials advancement that paves the road for the first Majorana braiding experiments. Achieved presents opportunities in the development of new quantum devices. For instance, devices working on the principle of beam splitting and interference of electrons (that is, Aharonov–Bohm interferometers), as well as other, less-investigated quasiparticles, that is, phonons. Additionally, these networks could be used to fabricate multi-terminal Josephson Junctions to investigating other, exotic topologically protected quasiparticle, such as Weyl fermions.[24]

4.4 Appendix

4.4.1 Substrate fabrication recipe

The starting point of the fabrication process is a 2-inch InP (100) wafer that can accommodate number of nanowire network chips. A design software has been written in order to manage the multiple fabrication of nanostructures with different parameters on a wafer. The software allows to write the lithographic model of nanostructures with different structural parameters into an area of 500x500 mm^2.

Fabrication of substrates with trenches is a three-step lithography process:

First, e-beam lithography and metal lift-off are used to deposit alignment markers on a (100) InP substrate.

Second, the InP (100) wafer is cleaned in buffered oxide etch (BOE) for 5 minutes and exposed to O_2 microwave plasma to create a thin (~2 nm) sacrificial layer of native oxide on the surface prior to deposition of 50 nm of SiO_x by plasma-enhanced chemical vapor deposition (PECVD). E-beam lithography and reactive ion etching (RIE) with CHF_3/Ar plasma are used to define rectangular openings in SiO_x, whose long edge is aligned with the [0-1-1] direction of the substrate. The alignment of the openings is crucial to achieve trenches with inclined (111)B facets after the subsequent anisotropic wet-etch step (HCl:H_3PO_4 = 5:11, for 15 s at 1 °C) or gaseous MOVPE HCl etch (χ_{HCl} = 3.33 × 10^{-6}, χ_{PH3} = 3.3 × 10^{-3}, 600 °C, ~6 minutes).

Third, SiO_x is stripped in BOE (5 minutes) and 20 nm of PECVD Si_xN_y is deposited on the substrate to prevent the parasitic InSb thin film growth which competes with nanowire growth.[18] E-beam lithography step followed by a short (40 seconds) BOE (NH_4F:HF = 20:1 + surfactant Triton) is used to define openings in the Si_xN_y mask. Metal evaporation (8 nm of Au) and lift-off are used to position Au catalysts (10-50 nm in size) in the openings in the Si_xN_y. Detailed description of processing steps is listed below.

a) **Markers**

Substrate Cleaning
- InP (100) wafer is cleaned with BOE (NH_4F:HF = 7:1) (5 minutes), rinsed with ultra-pure water (UPW), IPA (10 minutes).

Fabrication of markers
- Spin resist AR-P 6200.13 at 6000 rpm, bake at 150 °C for 3 minutes;
- Write marker patterns using e-beam lithography (dose 300 μC/cm^2);
- Developing in AR 600-546 for 1:30 minutes in ultrasonic agitation;
- Ultrasonic rinse in IPA for 30 seconds, blow dry;
- Evaporation of 80 nm Au;
- Lift-off in PRS3000 at 88 °C for 2 hours;
- Rinse in warm (>50 °C) UPW;
- Rinse in IPA for 1 minute, blow dry.

b) Trenches

Substrate Cleaning
- InP (100) wafer with markers is cleaned with buffered oxide etch ($NH_4F:HF = 7:1$) (5 minutes), rinsed with UPW, IPA (10 minutes).

Hard mask (1. in Figure 4.1)
- Sacrificial layer deposition microwave oxygen plasma (10 minutes, 200 mL/min, power 100 W, PVA Tepla 300);
- PECVD 20 nm SiO_x deposition (300 °C, Oxford Instruments PlasmaLab 80 Plus);
- Oxygen plasma (60 seconds, power 40 W).

Fabrication of trenches (2 – 8 in Figure 4.1)
- Spin primer (sticking layer) AR 300-80 at 2000 rpm, bake at 180 °C for 2 minutes
- Spin resist AR-P 6200.13 at 6000 rpm, bake at 150 °C for 3 minutes;
- Write trench patterns using e-beam lithography (dose 350 $\mu C/cm^2$);
- Developing in AR 600-546 for 1:30 minutes in ultrasonic agitation;
- Ultrasonic rinse in IPA for 30 seconds, blow dry;
- RIE (reactive ion etch) mask (23 W, 50 sccm CHF_3, 2 sccm Ar, Leybold Hereaus, 12 minutes);
- Wet etch in HCl (37%):H_3PO_4 (85%) ratio 5:1 (15 seconds, 1 °C) or HCl gaseous etch *in-situ* in MOVPE
- Strip the resist in PRS3000 at 88 °C for 20 minutes;
- Removing hard mask in buffered oxide etch ($NH_4F:HF = 7:1$) (5 minutes).

c) Catalyst deposition

Deposition of the mask (1. in Figure 4.2)
- PECVD 20 nm Si_xN_y deposition (300 °C, Oxford Instrumentals PlasmaLab 80 Plus);
- Oxygen plasma (60 seconds, power 40 W)

Dots formation (2 – 8 in Figure 4.2)
- Spin primer (sticking layer) AR 300-80 at 2000 rpm, bake at 180 °C for 2 minutes;
- Spin resist AR-P 6200.04 at 4000 rpm, bake at 150 °C for 3 minutes;
- Write dot patterns using e-beam lithography (dose 700-800 $\mu C/cm^2$);
- Developing in AR 600-546 for 1:30 minutes in ultrasonic agitation;
- Ultrasonic rinse in IPA for 30 seconds, blow dry;
- Opening the holes in Si_xN_y mask with buffered oxide etch ($NH_4F:HF = 20:1$) + 5 drops of surfactant Triton X-100 (40-60 seconds);
- Rinse with UPW, IPA (10 minutes);
- Evaporation of 10 nm Au;
- Lift-off in PRS3000 at 88 °C for 2 hours;
- Rinse in warm (>50 °C) UPW;
- Rinse in IPA for 1 minute, blow dry.

4.4.2 Prior the growth of nanowire networks

To remove organic residues from the wafer caused by the photoresist layer, substrates were descumed in O_2 plasma (10 minutes, 55 sccm O_2, 300 W plasma power) prior to loading into a horizontal Aixtron 200 metal-organic vapor phase epitaxy (MOVPE) reactor.

4.4.3 Atomic force microscope topography

We investigated the topography of our nanowire hashtag structure using atomic force microscopy (AFM), see Figure 4.10. All four junctions of nanowire "hashtag" structure appear smooth and uniform in height.

4
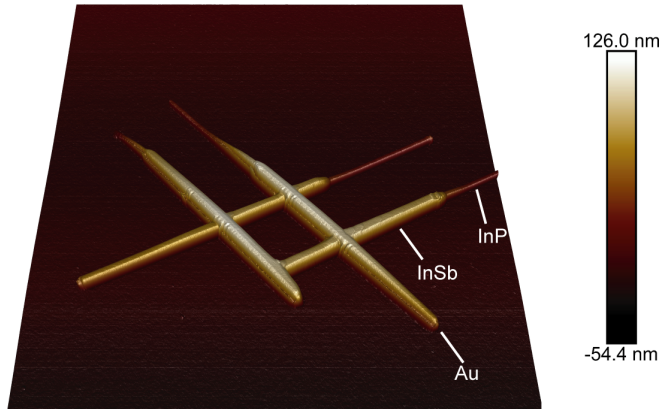
Figure 4.10 | Nanowire "hashtag" AFM topography. 3D reconstruction of the nanowire "hashtag" on a Si/SiO$_x$ substrate. Morphology of all four nanowire cross regions is visible. The height profile of the crossed nanowires is indicated by the black box on the right.

4.4.4 Device fabrication

Device fabrication recipe:

1. Transfer "hashtag" nanowires using nanomanipulator onto a p-doped Si substrate covered by 285 nm SiO$_2$ layer, serving as a back-gate dielectric.
2. Spinning bi-layer PMMA: first PMMA 495K A6 at 3000 rpm spinning rate, bake at 175 °C for 10 minutes. Then PMMA 950K A2 at 2000 rpm, bake at 175 °C for 10 minutes.
3. Write designed contacts and side gates patterns with e-beam.
4. Develop in developer (MIBK:IPA = 1:3) for 1 minute, clean in IPA for 1 minute, air-gun blow dry.
5. Descum, oxygen plasma 1 minute with power 100 W, pressure 1.95 mbar (with Faraday cage in to screen the plasma).
6. Sulphur passivation: dip the chip in ammonium sulfide solution (3 ml (NH$_4$)$_2$S mixed with 290 mg sulfur powder, then diluted with UPW at a volume ratio of 1:200) at 60 °C for 30 minutes. Then, rinse the chip in UPW and transfer to an evaporator.
7. Helium milling for 30 seconds with a Kauffman ion source. Then continue to evaporate Au/Cr (200 nm/10 nm). Cr is the sticking layer.
8. Lift off in acetone.

4.4.5 Device measurement and analysis

Measurement and Analysis:
All the four AB devices were measured in a He-3 fridge with based temperature ~300 mK. During the measurement, the side gates (grey in Figure 4.9a left inset) were kept grounded, and the global back gate is used to turn on the conducting channels in the "hashtag arms". The back-gate voltage is 13.35 V for the measurement in Figure 4.9a.

Ensemble average of FFT: The FFT spectrum shown in Figure 4.9b is an ensemble average of the absolute values of 25 individual FFT spectra[25]. The individual FFTs were calculated from the corresponding magnetoconductance traces (including the one in Figure 4.9a), which were measured successively with gate voltage values between 13.3 V and 13.7 V (resulting in conductance values between 0.7 and 0.9 x $2e^2$/h). A smooth background is subtracted from the original magnetoconductance curves before the FFT is calculated.

Estimation of "hashtag" loop area: The estimation is based on the SEM images of the device. We took the middle of the wire as the loop boundary to estimate the area, while the error bar of the area is estimated based on the accuracy of the nanowire length we measured from SEM images.

Estimation of phase coherence length: The amplitude of the AB oscillations is determined by integrating the obtained Fourier spectrum over the frequency range corresponding to the expected h/e peak. This amplitude decays as $\exp(-L/L_\varphi(T)$, where L is the relevant device length, and L_φ is the phase coherence length. For a quasiballistic system coupled to a thermal bath, we have $L_\varphi \propto T^{-1}$ giving an exponential dependence of the AB amplitude on temperature.[26] The slope of the fitted curve then gives the ratio between L and L_φ at 1 K. This allows us to estimate the phase coherence length if the relevant device length scale is known.

4.4.6 Aharonov-Bohm oscillations in hashtags spanning different areas
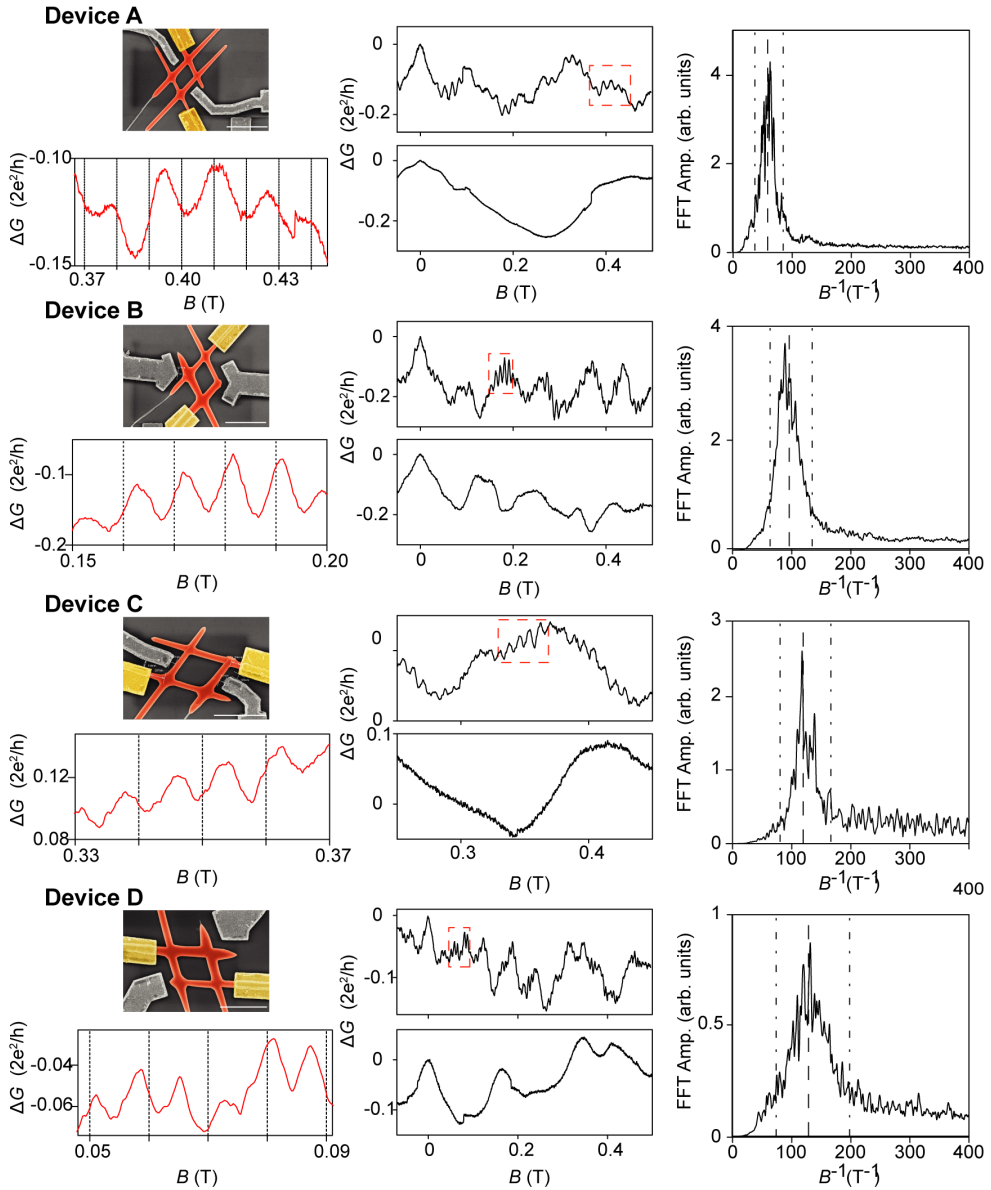
Figure 4.11 | Aharonov–Bohm oscillations in four devices with different hashtag surface areas. Magnetoconductance of a hashtag shows periodic Aharonov–Bohm oscillations and a weak-antilocalization Device A has been studied in detail in the main text of this chapter (Figure 4.9). For all devices, left upper panel shows the pseudo-colored SEM image of the device, middle panels show the conductance measured in the out-of-plane (top) and in-plane (bottom) magnetic field and right panel shows the ensemble averaged FFT spectrum. Only the out-of-plane magnetic field, whose flux penetrates through the hashtag loop, gives Aharonov–Bohm oscillations which indicates that the Aharonov–Bohm oscillations indeed originate from the coherent interference of electron waves of the two separated

conducting nanowire arms. A magnified view of the Aharonov–Bohm oscillations (a zoom-in on the region indicated by an orange rectangle in the upper middle panel) is shown in the lower left panel, while the right panel shows the averaged FFT spectrum. Plot of the peak frequency, assigned from the averaged FFT spectra, as a function of the measured loop area of the four devices is shown in the inset of Figure 4.9b. Weak-antilocalization peak at $B = 0$ T is present for both field directions, and in three (A, B, D) out of four devices, suggesting the strong spin–orbit nature of the InSb nanowire network. The corresponding back gate voltages of the four devices are: 15 V, 9 V, 12 V and 9 V, respectively. Temperature is 300 mK. The scale bar is 1 μm.

4.5 References

1   Mourik, V. *et al.* Signatures of Majorana Fermions in Hybrid Superconductor-Semiconductor Nanowire Devices. *Science* **336**, 1003-1007, doi:10.1126/science.1222360 (2012).

2   Alicea, J. *et al.* Non-Abelian statistics and topological quantum information processing in 1D wire networks. *Nat Phys* **7**, 412 (2011).

3   Hyart, T. *et al.* Flux-controlled quantum computation with Majorana fermions. *Physical Review B* **88**, 035121, doi:10.1103/PhysRevB.88.035121 (2013).

4   Aasen, D. *et al.* Milestones Toward Majorana-Based Quantum Computing. *Physical Review X* **6**, 031016 (2016).

5   Plugge, S., Rasmussen, A., Egger, R. & Flensberg, K. Majorana box qubits. *New Journal of Physics* **19**, 012001 (2017).

6   Vijay, S. & Fu, L. Teleportation-based quantum information processing with Majorana zero modes. *Physical Review B* **94**, 235446, doi:10.1103/PhysRevB.94.235446 (2016).

7   Karzig, T. *et al.* Scalable designs for quasiparticle-poisoning-protected topological quantum computation with Majorana zero modes. *Physical Review B* **95**, 235305, doi:10.1103/PhysRevB.95.235305 (2017).

8   Shabani, J. *et al.* Two-dimensional epitaxial superconductor-semiconductor heterostructures: A platform for topological superconducting networks. *Physical Review B* **93**, 155402 (2016).

9   Conesa-Boj, S. *et al.* Gold-Free Ternary III–V Antimonide Nanowire Arrays on Silicon: Twin-Free down to the First Bilayer. *Nano Letters* **14**, 326 (2014).

10   Plissard, S. R. *et al.* From InSb Nanowires to Nanocubes: Looking for the Sweet Spot. *Nano Letters* **12**, 1794 (2012).

11   Caroff, P. *et al.* InSb heterostructure nanowires: MOVPE growth under extreme lattice mismatch. *Nanotechnology* **20**, 495606 (2009).

12   Dalacu, D., Kam, A., Austing, D. G., Poole, P. J. & al., e. Droplet Dynamics in Controlled InAs Nanowire Interconnections. *Nano Letters* **13**, 2676 (2013).

13   Kang, J.-H. *et al.* Crystal Structure and Transport in Merged InAs Nanowires MBE Grown on (001) InAs. *Nano Letters* **13**, 5190-5196, doi:10.1021/nl402571s (2013).

14   Rieger, T. *et al.* Crystal phase transformation in self-assembled InAs nanowire junctions on patterned Si substrates. *Nano letters* **16**, 1933 (2016).

15   Plissard, S. R. *et al.* From InSb Nanowires to Nanocubes: Looking for the Sweet Spot. *Nano Letters* **12**, 1794-1798, doi:10.1021/nl203846g (2012).

16   Car, D., Wang, J., Verheijen, M. A., Bakkers, E. P. A. M. & Plissard, S. R. Rationally Designed Single-Crystalline Nanowire Networks. *Advanced Materials* **26**, 4875-4879, doi:10.1002/adma.201400924 (2014).

17   Kang, J.-H. *et al.* Au-Assisted Substrate-Faceting for Inclined Nanowire Growth. *Nano Letters* **18**, 4115-4122, doi:10.1021/acs.nanolett.8b00853 (2018).

18   White, L. K. Bilayer Taper Etching of Field Oxides and Passivation Layers. *Journal of The Electrochemical Society* **127**, 2687-2693, doi:10.1149/1.2129573 (1980).

19   Dalacu, D. *et al.* Selective-area vapour–liquid–solid growth of InP nanowires. *Nanotechnology* **20**, 395602 (2009).

20   Aharonov, Y. & Bohm, D. Significance of Electromagnetic Potentials in the Quantum Theory. *Physical Review* **115**, 485-491, doi:10.1103/PhysRev.115.485 (1959).

21   Kammhuber, J. *et al.* Conductance Quantization at Zero Magnetic Field in InSb Nanowires. *Nano Letters* **16**, 3482-3486, doi:10.1021/acs.nanolett.6b00051 (2016).

22   Gül, Ö. *et al.* Towards high mobility InSb nanowire devices. *Nanotechnology* **26**, 215202 (2015).

23   Hansen, A. E., Kristensen, A., Pedersen, S., Sørensen, C. B. & Lindelof, P. E. Mesoscopic decoherence in Aharonov-Bohm rings. *Physical Review B* **64**, 045327 (2001).

24   Riwar, R.-P., Houzet, M., Meyer, J. S. & Nazarov, Y. V. Multi-terminal Josephson junctions as topological matter. *Nature Communications* **7**, 11167, doi:10.1038/ncomms11167 (2016).

25   Meijer, F. E., Morpurgo, A. F., Klapwijk, T. M., Koga, T. & Nitta, J. Statistical significance of the fine structure in the frequency spectrum of Aharonov-Bohm conductance oscillations. *Physical Review B* **69**, 035308 (2004).

26   Stern, A., Aharonov, Y. & Imry, Y. Phase uncertainty and loss of interference: A general picture. *Physical Review A* **41**, 3436 (1990).

4

5

Chapter

Advanced Majorana nanowire device

Abstract *Majorana zero modes are predicted to emerge once a superconductor is coupled to a semiconductor nanowire with strong spin–orbit interaction in an external magnetic field. Following proposals for their detection, a number of tunneling spectroscopy experiments showed "Majorana-like" signatures (localized state at zero bias/energy, referred to as a zero bias peak). The height of the zero bias peak is predicted to be quantized at the universal conductance value of $2e^2/h$. Previous experiments, however, reported zero bias peaks reaching much smaller values than $2e^2/h$. The prime challenge was the disorder in the superconductor-nanowire that creates a so-called "soft superconducting gap", and importantly disorder can mimic the zero energy state of Majoranas. In this chapter we report the growth of a hybrid, Al-InSb superconductor-semiconductor, nanowire device. The growth of Al was performed in-situ at liquid nitrogen temperatures reducing the Al diffusion length and allowing for the growth of a very thin film needed to ensure coherence length of Al. Samples with nanowire network geometry were used and superconducting islands are grown. We have investigated rapid in-situ oxidation methods, important to consolidate the continuous and almost single crystalline Al layer. In-situ TEM heating experiment allowed us to determine the maximum device fabrication temperature, that is below 120 °C (much lower than typical resist baking temperatures). These material improvements and understanding enable creating advanced Majorana device paving the way for future experiments that could lead to the topological quantum computing.*

5.1 Introduction

Majorana zero-modes—a type of localized quasiparticle—hold great promise for topological quantum computing.[1] In Chapter 2 tunneling spectroscopy experiment are introduced in order to investigate proximity induced superconductivity and identify the presence of Majorana zero modes. A semiconductor nanowire coupled to a superconductor can be tuned into a topological superconductor with two Majorana zeromodes localized at the wire ends.[1-3] Tunneling into a Majorana mode will show a zero-energy state in the tunneling density-of-states, that is, a zero-bias peak (ZBP) in the differential conductance (dI/dV).[4,5] The height of the Majorana zero-bias peak is predicted to be quantized at the universal conductance value of $2e^2/h$ as a direct consequence of the famous Majorana symmetry in which a particle is its own antiparticle.[6]

A short update on the progress in superconductor-InSb system is given in the Chapter 2. The two main challenges of the field, caused by the disorder in the system, are: the induced soft superconducting gap caused by disorder at the superconductor-semiconductor interface, and consequently, conductance quantization has not yet been observed,[4,5,7] instead, most of the ZBPs have a height considerably less than $2e^2/h$.

In this chapter we tackle the disorder problem by focusing on *in-situ* growth of the superconductor on the semiconductor. Substantial advances are achieved by eliminating disorder and interface roughness by choosing the optimum growth and post-growth conditions. An advanced sample geometry allows for growth of separated superconducting islands, and, importantly understanding and controlling detrimental parameters during device processing. We focus on the growth of Al superconducting films on InSb nanowires but emphasize that similar methods can be applied, *e.g.*, Sn- , V- , In- , Pb-InSb combinations. The growth technique was molecular beam epitaxy (MBE). The MBE cluster in Palmstrøm's group offers the possibility for *in-situ* device growth.

5.2 Results

5.2.1 Superconducting aluminum islands

Nanowire networks samples (discussed in the Chapter 4) are used for the experiments discussed in this chapter. The nanowire samples are grown in an MOVPE reactor and transferred *ex-situ* to an MBE cluster tool where an atomic hydrogen clean (20 minutes under continuous rotation, 380 °C, 5×10^{-6} Torr H_2 pressure) is first done to remove the native oxide from the InSb nanowire surface.[8] The source of hydrogen is under an angle to the sample holder. Subsequently, samples are transferred to the Al-deposition chamber, in which they are cooled down to ~120 K by active liquid nitrogen (LN_2) cooling. It is known that the diffusion length of Al adatoms is long, hence for the growth of continuous thin films it is beneficial to lowering the sample temperature such that the diffusivity is drastically reduced. The Al cell temperature was 1085 °C, resulting in a growth rate of ~2 Å/min. We choose the growth rate of Al to be slow to prevent heating of the nanowire sample by the Al source. The nanowire network geometry is combined with the directionality of MBE to shadow-grow aluminium superconducting islands (SCIs) on the InSb wires. Careful alignment of nanowires relative to the Al source is important for well-controlled shadowing of the nanowires. The aluminium flux is aligned parallel to the trenches (Figure 5.1a), such that a frontal wire casts a shadow on a wire in the background (Inset Figure 5.1a). This causes interruptions in the layer of aluminium as shown in Figure 5.1b-c, forming Al islands. The partial coverage of a nanowire with Al is essential as it allows tuning of the electron density of the proximitized nanowire by an external gate electrode, which is necessary for accessing the topological phase. The shadow-deposition method eliminates the need for metal etching during device fabrication and the integration of semiconductors with metals is possible without invasive etching processes. The latter guarantees that the pristine atomically flat InSb (110) facets are left intact as high quality nanowire channels with intact surfaces are the key-element for high device performance.[9,10] For an effective shadowing, it is important that the frontal wire does not merge with the shadowed wire, *i.e.*, the offset between the wires should be larger than the wire diameter ($\Delta y > D_{Au}$, see Chapter 4 for the dimensions). The number of shadows, n, (and, accordingly, the number of SCIs, $n+1$) on any InSb nanowire is determined by the number of wires directly in front of that nanowire. For example, Figure 5.1c depicts an InSb nanowire with three shadows cast by three frontal nanowires. The position and the width of the shadows are uniform for all wires examined and are set by the relative position of the wires and the solid angle of the aluminium effusion cell.
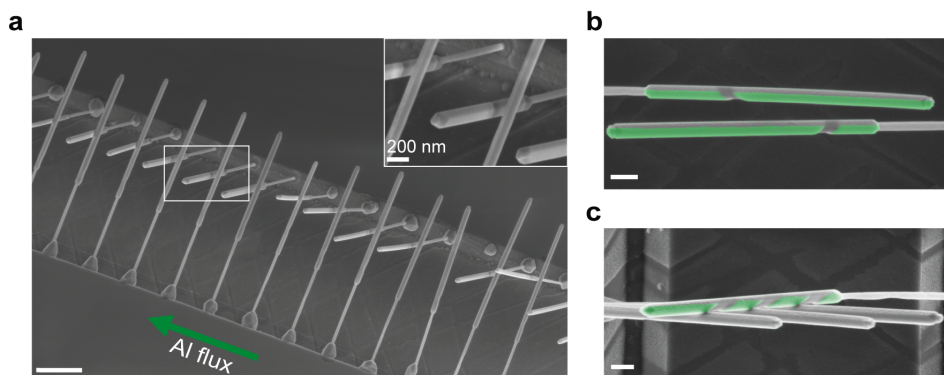
Figure 5.1 | Growth of Al islands on InSb nanowires. a, A 45°-tilted SEM image of an array of Al–InSb nanowires. The green arrow indicates the direction of the Al beam flux during deposition. Scale bar is 1 µm. Inset, magnified area indicated by a white rectangle in the main panel. Each InSb nanowire is covered by two Al islands separated by a shadowed region. The number of shadows, n, and hence the number of superconducting islands, $n + 1$, is determined by the number of wires directly in front of the shadowed wire. SEM image of InSb nanowires with **b,** two, and **c,** four Al islands (false-colored green). Scale bars are 200 nm.

The morphology of the aluminium layer is revealed by HR-TEM imaging in Figure 5.2a. The Al film is crystalline and has a uniform thickness of ~10 nm. The interface between the Al and the InSb is epitaxial. The abrupt transition between the shadowed region of the nanowire and the segment covered with aluminium is evident from the chemical composition map (Figure 5.2b) acquired by energy-dispersive x-ray spectroscopy (EDX) combined with scanning transmission electron microscopy (STEM). The line-of-sight directionality of MBE growth results in aluminium being deposited on two out of six facets of an InSb nanowire, as can be seen from a STEM-EDX map of a nanowire cross-section (Figure 5.2c).
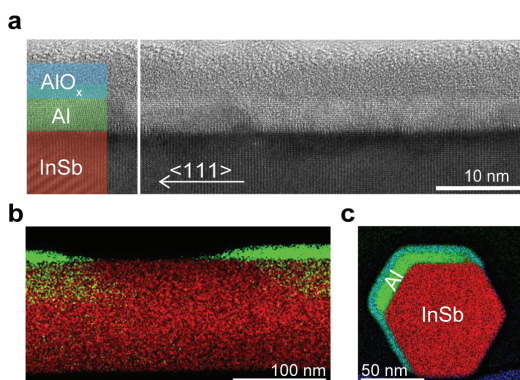
Figure 5.2 | Disorder-free Al-InSb interface. a, HR-TEM image of an InSb nanowire (red) covered with a thin (about 10 nm), crystalline film of Al (green) and a layer of AlO$_x$ (blue). InSb growth direction ⟨111⟩ is indicated by a white arrow. The image is taken along the ⟨110⟩ zone axis. **b,** STEM–EDX chemical composition map of an InSb nanowire (red) with Al islands (green) separated by an Al-free shadowed region. **c,** EDX chemical composition map of the nanowire cross-section. Al (green) is covering two out of the six {110} InSb side-facets. The Al–InSb interface is oxygen-free.

5.2.2 In-situ Al oxidation methods

An excellent morphology of the superconductor, implying a uniform layer thickness and a disorder-free interface is essential for Majorana physics. We have seen that the key parameter towards obtaining a short adatom diffusion length is lowering the substrate temperature to LN_2 temperatures (Figure 5.1). As a result, a continuous Al layer is formed on the nanowire facets. An additional diffusion component that impacts the morphology of the Al layer is the post-growth diffusion of Al, which takes place during sample heat-up to room temperature. This postgrowth diffusion has detrimental effects on the superconductor layer: 1) formation of a non-uniform Al layer, 2) interface reactions between Al and InSb, driven by thermodynamics and strain. An SEM image of an Al-InSb sample that was kept in UHV conditions for two hours after the Al growth, at LN_2 temperatures, and before it was vented to the atmosphere is shown in Appendix (Figure 5.8). The Al appears rough, and regions composed of discontinuous Al islands are recognizable, illustrating the problems of post-growth diffusion.

This post-growth diffusion can be avoided by oxidation of the Al, such that an AlO_x layer is formed on top of the Al layer, which mechanically stabilizes the Al layer.[9] This self-terminating oxide layer will "freeze-in" the Al film onto the surface of the nanowire facets. After growth of the Al layer and prior to the exposure to the atmosphere it is important to oxidize the Al *in-situ*, while the sample is still cold. Ergo, an adequate growth sequence includes Al growth followed by fast oxidation. Here, we investigated three different *in-situ* Al-capping methods available in the MBE cluster, which are: 1) Loadlock venting with nitrogen gas followed by the fast pumping to the vacuum conditions; 2) Aluminum oxide (AlO_x) evaporation from an e-gun source; 3) Exposure to an ultra-high purity oxygen (O_2) gas in the oxide MBE chamber. The Al thin film growth conditions for samples used for these experiments were the same, (~120 K, ~2 Å/min, 75 minutes). After the growth of Al, it takes approximatively 10-20 minutes to transfer the sample from the cold stage to the oxygen-abundant ambient.

We study the morphology, interface and elemental composition of these samples using BF TEM, HAADF-STEM and EDX, respectively. At least three nanowires are deposited on the Si chip from each experiment and a cross-sectional thin lamella is prepared using a focused ion beam. The images presented in Figure 5.3 are representative for each experiment. Each technique reveals important information on the Al layer along the wire and in the cross-section direction. Importantly, the cross-sectional samples display that all six facets of InSb are flat implicating that that the cleaning by atomic hydrogen prior to Al deposition, used to remove the native oxides of InSb, has not deteriorate the InSb facets. From EDX mapping we conclude that the native InSb oxides have been removed, such that we start the Al deposition on a clean, epitaxial InSb surface.
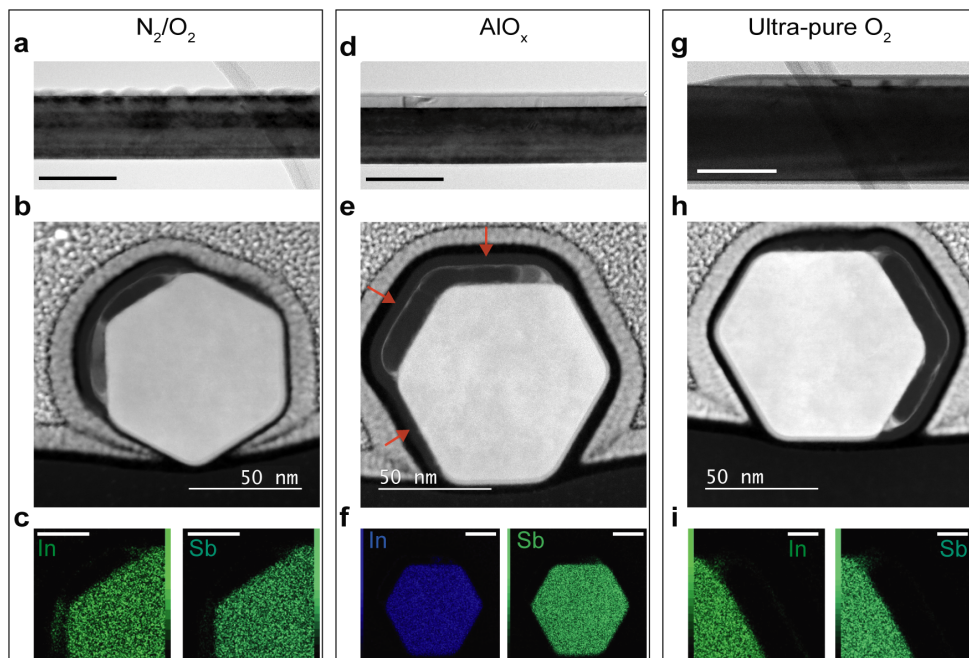
Figure 5.3 | *In-situ* oxidation methods of Al-InSb samples. Three different *in-situ* oxidation methods are analyzed: Loadlock venting (panels **a-c**), AlO$_x$ evaporation (panels **d-f**) and exposure to high purity oxygen (panels **g-i**). BF TEM along Al-InSb nanowires deposited on a holey carbon grid is in panels **a**, **d**, **g**. The image is taken along <112> zone axis. HAADF-STEM images of a nanowire cross-sectional lamellae is in panels **b**, **e**, and **h**. EDX elemental mapping for In (K) (left) and Sb (L) (right) are in panel **c**, **f** and **i**. Scale bars for **c, f** and **i** are 20 nm, 30 nm and 10 nm, respectively.

For the structure shown in Figure 5.3a-c loadlock venting with a N$_2$/O$_2$ mixture was used. The BF TEM image along the nanowire in Figure 5.3a indicates that the Al layer was not properly oxidized, allowing for further Al diffusion during heat up. As a result the Al has diffused along the nanowire surface, forming Al islands. The cross-sectional analysis (Figure 5.3b) confirms that the Al layer varies in thickness, coherent with our hypothesis. Moreover, both In and Sb are detected in the Al layer, visible in the EDX map (Figure 5.3c), indicating that Al has reacted with the InSb.

The sample in Figure 5.3d is capped with an AlO$_x$ layer. The AlO$_x$ was evaporated from an e-gun source perpendicular to the sample holder that was kept at room temperature (2 min under continuous rotation, 2 x 10^{-7} Torr pressure). The aimed nominal thickness of AlO$_x$ was 3 nm. The analysis along the length of the nanowire demonstrates the presence of a continuous Al film on the nanowire (Figure 5.3d). Due to the sample geometry AlO$_x$ was deposited on three facets of the Al-InSb nanowire indicated onto with red transparent arrows in the HAADF-STEM image (Figure 5.3e). In contrast to previous experiment, the Al layer in the cross-section seems smooth and continuous, capped with a conformal AlO$_x$ layer.

Oxidation through exposure to ultra-high purity oxygen appears very similar to AlO$_x$ capping along the nanowire and in cross-sectional imaging (Figure 5.3g and

Figure 5.3h). The sample was exposed to oxygen for ~30 minutes under continuous rotation at room temperature reaching low 10^{-6} to 10^{-5} Torr O_2 pressure. Interestingly, all three samples display a thin layer between Al and AlO_x appearing bright in the HAADF-STEM images. The bright layer corresponds to In, which likely diffused over the Al as "hot" Al adatoms were reaching the surface of the nanowire facet. Also, at the edges of Al as well as at the interface between Al and AlO_x some InSb can be discerned from EDX mapping (Figure 5.3c, f and i).

5.2.3 In-situ temperature experiments

In previous subsections we learned that the Al-InSb system is a delicate material system particularly sensitive to the temperature changes. Nevertheless, high-quality Al-InSb nanowires are obtained, confirmed by TEM. The next step is to assess the electronic quality of those structures. Fabrication of Majorana device requires a number of steps where even slight heating of the nanowire is almost inevitable (*e.g.*, resist baking, Ar or He milling). However, the temperature at which the Al layer start to react with the InSb is unknown.

We perform *in-situ* TEM heating experiment and study interface reactions as a function of temperature. For this work, a commercial DENSsolution six contact double tilt TEM holder is used with a through hole heater chip. Al-InSb nanowires, *in-situ* capped with AlO_x are transferred using a nanomanipulator and carefully suspended over the hole in the chip such that the nanowire has a good thermal contact to the heater. In Figure 5.4 BF STEM images of the nanowire undergoing the *in-situ* heating experiments are shown. The sequence of images is arranged in temperature/temporal order. The first changes in the Al layer are already observed at 120 °C. Dark areas appear in the layer and the interface between the Al and the InSb roughens.
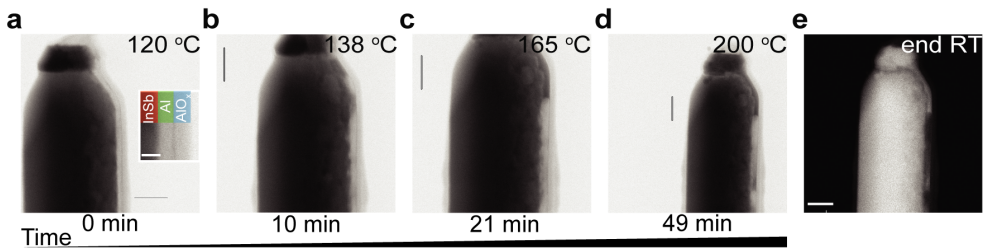
Figure 5.4 | *In-situ* heating STEM study for varying temperatures. BF STEM image of an Al-InSb nanowires undergoing the heating experiment **a-d** and HAADF-STEM image of the end result **e**. Transformations in the Al layer are recorded for different sample heating temperatures. Time and temperature are specified in the images. Inset: Zoom-in to the false-colored segments for clarification. The InSb nanowire (red), Al layer (green), AlO_x layer (blue). The scale bar in the inset is 10 nm. Scale bars for all images are 50 nm.

A further increase in temperature (138 °C) results in In and Sb locally entering the Al layer as Al is being pushed outward (notice the thickening in the AlO_x at the

bottom of the BF STEM image), already after only 10 minutes. Increasing the temperature even further (to 165 °C and 200 °C) continuously transforms the Al layer with an increasing number of local spots that spread through the Al layer.

Our experiments point towards a maximum device fabrication temperature of 120 °C. However, at a constant temperature of 120 °C changes in the Al layer are already observed after 5 minutes of annealing (see Appendix Figure 5.9).
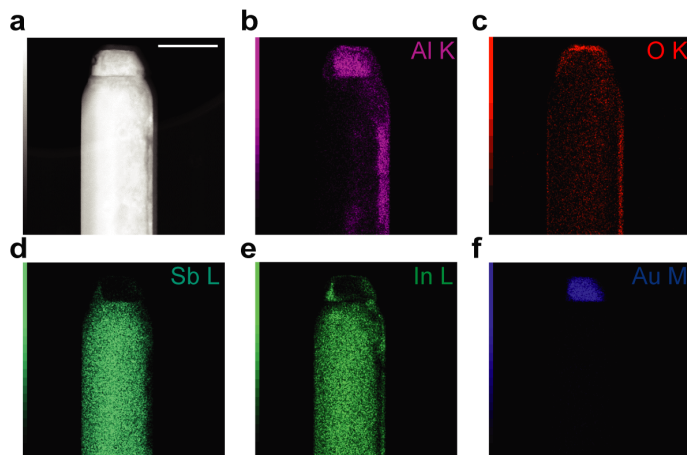
Figure 5.5 | Elemental mapping of the Al-InSb nanowire annealed at 200°C. a, HAADF-STEM image the Al-InSb nanowire annealed at 200°C. **b**-f, EDX elemental mapping of the nanowire from the panel **a**. The scale bar is 100 nm.

Note that the *in-situ* TEM used for the study is not compatible with EDX mapping. To analyze the specific elemental components present in the Al layer we annealed a holey carbon film with our Al-InSb nanowires at 200 °C for 20 minutes and analyzed the same using STEM-EDX (Figure 5.5). The HAADF-STEM image in the Figure 5.5a shows similar features as the image obtained from the Al-InSb nanowire, imaged at room temperature after the *in-situ* experiment, as shown in Figure 5.4e. This allows us to directly compare the EDX elemental mapping of the two heated nanowires. The EDX data in Figures 5.5b-f supports the above discussed – both In and Sb are protruding into the Al layer.

5.2.4 Hard-induced superconducting gap and ZBP in Al-InSb nanowires

In this subsection, we assess the electronic quality of our structures. The essential ingredient for a topological phase is induced superconductivity in the InSb nanowires. For this reason, we first study InSb wires with two SCIs were used to fabricate "simple" N (normal) – nanowire – S (superconductor) devices by replacing one SCI with a normal metal electrode to measure induced superconductivity (see Appendix Subsection 5.4.4 for the device fabrication steps). To prevent interdiffusion of Al and InSb, baking steps in the fabrication process are omitted. The shadowed region of the nanowire is situated in between the normal contact and the other SCI, and can be depleted by a bottom gate (inset Figure. 5.6c), to form a tunnel barrier. In the tunnelling regime, the differential conductance reflects the quasiparticle density-of-states in the proximitized nanowire segment. Figure 5.6a shows a plot of the differential conductance (dI/dV) vs. bias voltage (V) and back-gate voltage (V_{gate}) at 20 mK. Hence, the two high-conductance horizontal lines (at $V = \pm 0.24$ mV) in Figure 5.6a correspond to the superconducting coherence peaks. The shape of the superconducting gap can be clearly resolved in Figure 5.6b, which shows a vertical line-cut plotted on both linear (left) and logarithmic (right) scale, indicating the ratio of the above-gap to sub-gap conductance $G_N/G_S \sim 100$. Figure 5.6c maps out the obtained values of G_S vs. G_N (black dots) together with the Beenakker expression (red line) for an N-QPC-S system (QPC being quantum point contact). This expression assumes that G_S is due to a single channel Andreev reflection in the shadowed region (see Appendix Figure 5.10).[11] Theory and experiment are in agreement over two orders of magnitude in conductance. This shows that the G_S in this system is dominated by the Andreev process in the absence of quasi-particle transport. Figure 5.6d shows the differential conductance (dI/dV) of the same device as a function of bias voltage (V) and magnetic field (B) pointing along the nanowire, taken at $V_{gate} = -5.7$ V. From the horizontal line-cut at $V = 0$ V (lower panel), it can be clearly seen that G_S is pinned to extremely low values of conductance for magnetic field values up to 0.9 Tesla. The evolution of the induced superconducting gap in the magnetic field is illustrated in Figure 5.6e. The black, green and orange line cuts are taken at $B = 0$, 0.5 and 1 T, respectively. Importantly, the induced hard superconducting gap in Al-InSb nanowires endures up to $B \sim 0.9$ T, which surpasses the value of the magnetic field required for achieving a topological phase transition in InSb ($B \sim 0.2$ T).[2,3,7] Figure 5.10 in Appendix shows data of additional devices and the corresponding analysis.
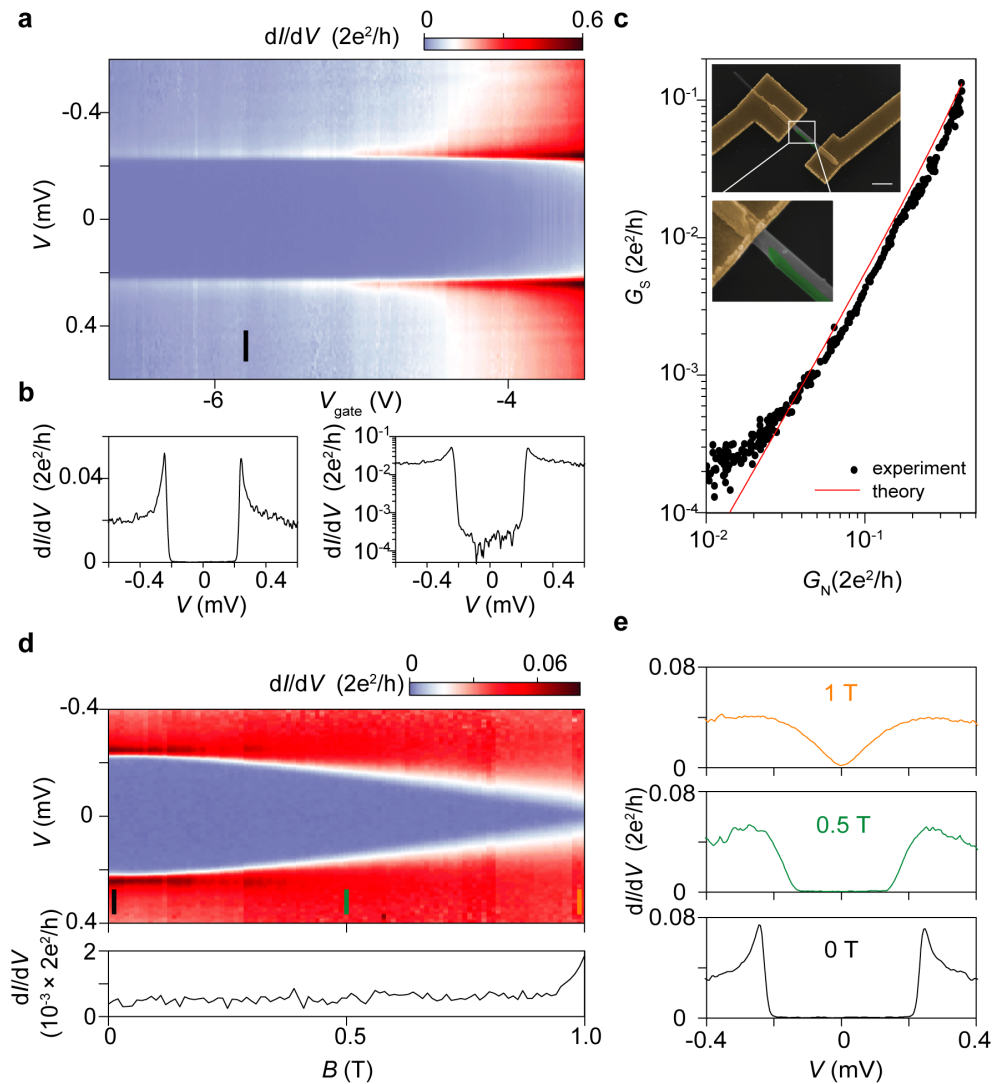
Figure 5.6 | Hard induced superconducting gap in shadowed Al-InSb nanowire device. a, Differential conductance (dI/dV) as a function of bias voltage (V) and back gate voltage (V_{gate}) in the tunneling regime, resolving a hard superconducting gap (at ~20 mK). b, A line cut taken at the position indicated by the black bar in panel a (at V_{gate} = -5.8 V), plotted on linear (left) and logarithmic scale (right). The ratio of above-gap and sub-gap conductance (G_N/G_S) reaches ~100. The induced superconducting gap size is Δ ~ 0.24 meV. **c,** Sub-gap conductance as a function of above-gap conductance. The red line is the theoretical curve calculated assuming only Andreev processes[11]. Inset, A false-colored SEM image of the similar device. The device is an N (yellow)-nanowire (grey)-S (green) system. **d,** Magnetic field dependence of the superconducting gap (V_{gate} ~ -5.7 V) in the device. The magnetic field direction is aligned with the nanowire axis. The lower panel shows a horizontal line-cut taken at V = 0 V (in the middle of the superconducting gap). **e,** Vertical line cuts taken at positions indicated by a black (B = 0 T), green (B = 0.5 T) and orange bar (B = 1 T) in the upper panel d, illustrating the evolution of the induced superconducting gap in the increasing magnetic field.

We have demonstrated a presence of a hard-superconducting gap in InSb nanowires, induced by local superconductor islands. This marks our material system fitting for Majorana devices. Figure 5.7a shows a false-colored SEM image of a fabricated device and schematics of the measurement set-up. An InSb nanowire (grey) is partially covered by a thin superconducting Al shell (green). The "tunnel-gates" (coral red) are used to induce a tunnel barrier in the non-covered segment between the left electrical contact (yellow) and the Al shell. The right contact is used to drain the current to ground. The chemical potential in the segment covered with Al can be tuned by applying voltages to the two long "super-gates" (purple). Transport spectroscopy is shown in Figure 5.7b, which displays dI/dV as a function of voltage bias V and magnetic field B (aligned with the nanowire axis), while fixed voltages are applied to the tunnel- and super-gates. As B increases, two levels detach from the gap edge (at about 0.2 meV), merge at zero bias and form a robust ZBP. This is consistent with the Majorana theory: a ZBP is formed after the Zeeman energy closes the trivial superconducting gap and re-opens a topological gap.[2,3] The gap re-opening is not visible in a measurement of the local density-of-states because the tunnel coupling to these bulk states is small.[12] Moreover, the finite length (about 1.2 μm) of the proximitized segment (that is, the part that is superconducting because of the proximity effect from the superconducting Al layer) results in discrete energy states, turning the trivial-to-topological phase transition into a smooth crossover[13]. Figure 5.7c shows two line-cuts from Figure 5.7b extracted at 0 T and 0.88 T. Importantly, the height of the ZBP reaches the quantized value of $2e^2/h$. The line-cut at zero bias in the lower panel of Figure 5.7b shows that the ZBP height remains close to $2e^2/h$ over a sizable range in B field (0.75–0.92 T). Beyond this range, the height drops, most probably because of a closure of the superconducting gap in the bulk Al shell. We note that the sub-gap conductance at $B = 0$ (black curve, left panel, Figure 5.7c) is not completely suppressed down to zero, reminiscent of a soft gap. In this case, however, this finite sub-gap conductance does not reflect any finite sub-gap density-of-states in the proximitized wire. It arises from Andreev reflection (that is, transport by dissipationless Cooper pairs) due to a high tunneling transmission, which is evident from the above-gap conductance (dI/dV for $V > 0.2$ mV) being larger than e^2/h. As this softness does not result from dissipation, the Majorana peak height should still reach the quantized value.[14]
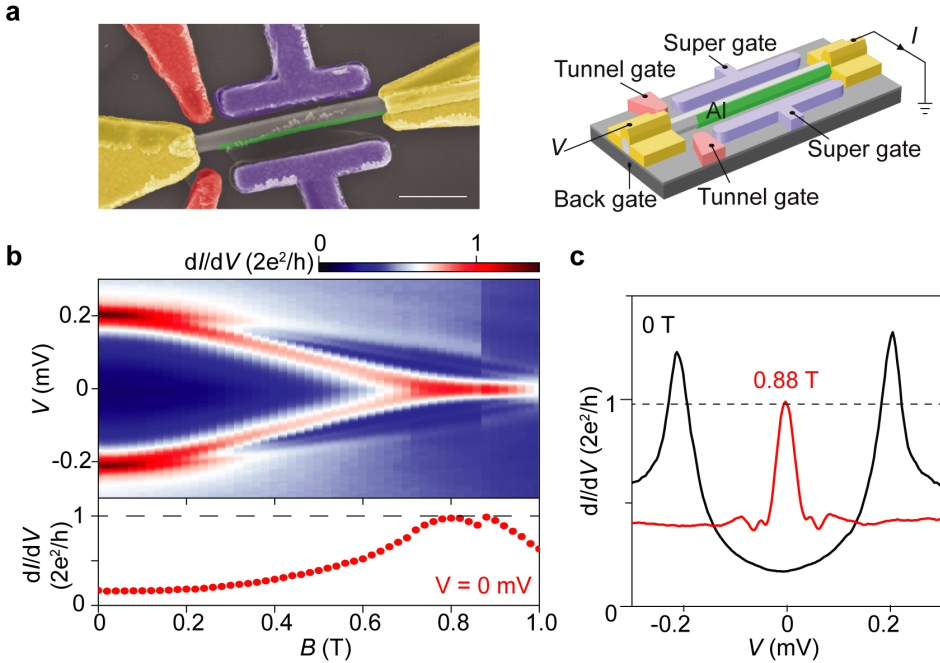
Figure 5.7 | Quantized Majorana zero-bias peak. a, False-colored SEM of device A (left panel) and its schematics (right panel). Side gates and contacts are Au/Cr (100 nm/10 nm). The Al shell thickness is approximately 10 nm. The substrate is p-doped Si, acting as a global back-gate, covered by 285 nm SiO_2. The two tunnel-gates are shorted externally, as are the two super-gates. The scale bar is 500 nm. **b,** Magnetic field dependence of the quantized ZBP in device A with the zero-bias line-cut in the lower panel. Magnetic field direction is aligned with the nanowire axis for all measurements. Super-gate (tunnel-gate) voltage is fixed at −6.5 V (−5.7 V), while the back-gate is kept grounded. Temperature is 20 mK unless specified. **c,** Left (right) panel shows the vertical line-cuts from **b** (**d**) at 0 T and 0.88 T (1.07 meV).

5.3 Conclusions

We reported a substantial material advancement by realizing hybrid Al-InSb SCIs solving disorder. A clean and uniform superconductor-nanowire interface is established, which is crucial for the quality of the induced gap.[5,15] Additionally, tunneling spectroscopy experiment reports a quantized conductance plateau at $2e^2/h$ at zero-bias. The observation of a quantized conductance plateau strongly supports the existence of Majorana zero-modes in the system, consequently paving the way for future braiding experiments that could lead to topological quantum computing (see Chapter 4).

5.4 Appendix

5.4.1 Substrate fabrication recipe

Substrate fabrication recipe is described in the Chapter 4, Subsection 4.4.1.

5.4.2 Post-growth Al diffusion
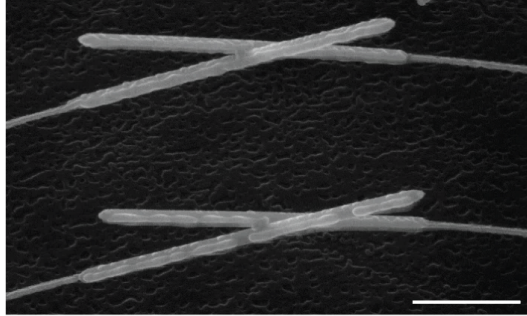
Figure 5.8 | Post-growth diffusion of Al along InSb nanowire in UHV conditions. A 30°-tilted SEM image of Al–InSb nanowires. Al layer appears rough and regions with separated discontinuous Al islands are observed. The scale bar is 500 nm.

5.4.3 In-situ heating experiment at constant temperature
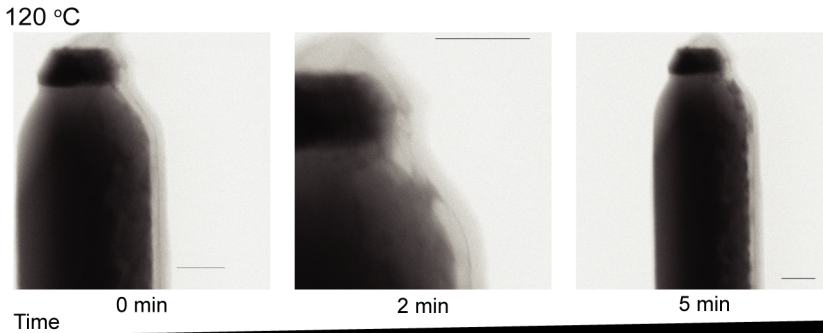
Figure 5.9 | _In-situ_ heating TEM study for constant temperature of 120 °C. BF STEM image of an Al-InSb nanowires. Transformation in the Al layer are recorded with the time. Time is specified below the images. Scale bars are 50 nm.

The clear change in the Al layer happens soon after the temperature is stable at 120 °C. Increasing the time even further a significant amount of InSb is permeated into Al.

5.4.4 Hard-gap and Majorana device fabrication

An InSb nanowires with two shadowed aluminium islands is contacted by Au/Cr. Argon plasma etching was used to remove the aluminium film prior to evaporation

of normal contacts. One normal contact is deposited right next to the shadowed region to replace one aluminium island. The second normal contact is on the other end of the nanowire, sufficiently apart from the shadowed region not to affect the superconducting properties in its vicinity, serving as a current drain for the superconducting contact.

> Device fabrication recipe:
> 1. Transfer Al-InSb nanowires onto a p-doped Si substrate covered by 285 nm SiO_2 layer, serving as a back-gate dielectric.
> 2. Spinning PMMA 950K A6 at 4000 rpm, leave the chip in a vacuum chamber pumped with a turbo for overnight. Baking is not performed!
> 3. Write designed contacts and side gates patterns with e-beam.
> 4. Development: (MIBK:IPA = 1:3) for 1 minute, IPA for 1 minute, blow dry.
> 5. Ar plasma etch for 4 minutes (with Ar pressure 3 mTorr, 100 W) to etch away Al, AlO_x, InSb surface oxide and part of the InSb nanowires. To prevent the PMMA from burning due to long plasma etch, one can perform short plasma etch (e.g. 20 seconds) for 12 times with 40 seconds break between each etch to let the chip to cool down.
> 6. Evaporate normal contact (and top gate contacts for Majorana device), Au/Cr (100 nm/10 nm).
> 7. Lift off in acetone.

5.4.5 Measurement procedure and analysis of the additional hard-gap devices

Device X (Figure 5.6), Z, M (Appendix Figure 5.10) were measured in a dilution refrigerator with a base temperature ~20 mK, while Device Y (Appendix Figure 5.10) was measured in a He-3 fridge with a base temperature ~300 mK.

Sub-gap vs above-gap conductance fitting in Al-InSb devices: we assume there is a single transmitting channel in the shadow region with transmission T. The above-gap conductance is conductance of normal carriers: $G_N = 2e^2/h \times T$, while sub-gap conductance, based on Beenakker's formula[11], is: $G_S = 2e^2/h \times 2T^2/(2-T)^2$. Thus, G_S can be plotted as a function of G_N as shown in Figure 5.6 (red line). For the experimental data, at each gate voltage, we get the above-gap conductance by averaging the conductance at bias (V) much larger than the gap (Δ), while the sub-gap conductance is obtained by averaging a small bias window at zero bias.

Contact transparency estimation based on Andreev enhancement: in Figure 5.10, we get Andreev enhancement for subgap conductance reaching $1.7 \times 2e^2/h$. Based on Beenakker's formula, setting this value equal to G_S, we can extract a transparency T ~ 0.96.
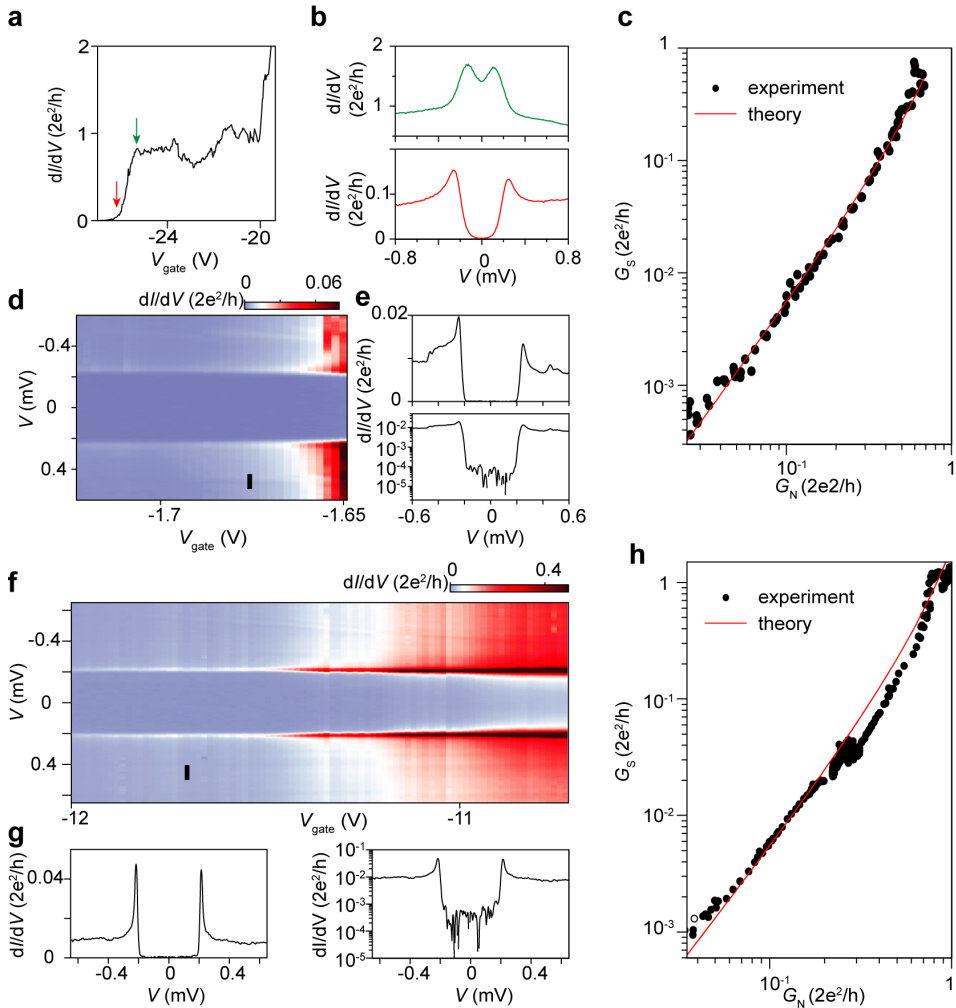
Figure 5.10 | Ballistic transport, Andreev enhancement and hard gap in additional Al-InSb devices. a, Above-gap (normal carriers) conductance of device Y as a function of V_{gate}. A conductance plateau near the quantized value ($2e^2/h$) can clearly be seen, indicating ballistic transport. **b**, dI/dV versus bias voltage in the open and tunneling regime, resolving strong Andreev enhancement (green) and a hard gap (red), respectively, with V_{gate} indicated by arrows in panel **a**. The coherence peaks are smeared out owing to thermal broadening (temperature of about 300 mK for this device). The Andreev enhancement is due to Andreev reflection: an incoming electron reflects as a hole at the N–S interface generating a Cooper pair. This process effectively doubles the transported charge from e to 2e, enhancing the sub-gap conductance. Our enhancement factor reaches $1.7 \times 2e^2/h$, indicating the high Al–InSb interface transparency, with transmission larger than 0.96. The small dip in Andreev enhancement near zero bias is due to mode mixing induced by minimal residual disorder[7]. **c**, Sub-gap versus above-gap conductance of device Y (black dots), and a theoretical fit (red) based on the Beenakker formula, showing perfect agreement over three orders of magnitude conductance change. **d**, dI/dV of device Z as a function of V_{gate}. **e**, A line cut from panel d (black bar), plotted in linear (top) and logarithmic scale (bottom). The above-gap/sub-gap ratio is larger than 300. **f**, dI/dV of device M as a function of V_{gate}. **g**, A line cut from panel **f** (black bar), plotted on linear (left) and logarithmic scale (right). **h**, Sub-gap versus above-gap conductance of device M (black dots), and the Beenakker theoretical fit (red). Device shown in the main text (X), and devices Z and M are measured at around 20 mK.

5.5 References

1   Kitaev, A. Y. Unpaired Majorana fermions in quantum wires. *Physics-Uspekhi* **44**, 131 (2001).

2   Lutchyn, R. M., Sau, J. D. & Das Sarma, S. Majorana Fermions and a Topological Phase Transition in Semiconductor-Superconductor Heterostructures. *Physical Review Letters* **105**, 077001, doi:10.1103/PhysRevLett.105.077001 (2010).

3   Oreg, Y., Refael, G. & von Oppen, F. Helical Liquids and Majorana Bound States in Quantum Wires. *Physical Review Letters* **105**, 177002, doi:10.1103/PhysRevLett.105.177002 (2010).

4   Mourik, V. *et al.* Signatures of Majorana Fermions in Hybrid Superconductor-Semiconductor Nanowire Devices. *Science* **336**, 1003-1007, doi:10.1126/science.1222360 (2012).

5   Lutchyn, R. M. *et al.* Majorana zero modes in superconductor–semiconductor heterostructures. *Nature Reviews Materials* **3**, 52-68, doi:10.1038/s41578-018-0003-1 (2018).

6   Liu, C.-X., Sau, J. D., Stanescu, T. D. & Das Sarma, S. Andreev bound states versus Majorana bound states in quantum dot-nanowire-superconductor hybrid structures: Trivial versus topological zero-bias conductance peaks. *Physical Review B* **96**, 075161, doi:10.1103/PhysRevB.96.075161 (2017).

7   Gül, Ö. *et al.* Ballistic Majorana nanowire devices. *Nature Nanotechnology* **13**, 192-197, doi:10.1038/s41565-017-0032-8 (2018).

8   Webb, J. L. *et al.* Electrical and Surface Properties of InAs/InSb Nanowires Cleaned by Atomic Hydrogen. *Nano Letters* **15**, 4865-4875, doi:10.1021/acs.nanolett.5b00282 (2015).

9   Krogstrup, P. *et al.* Epitaxy of semiconductor–superconductor nanowires. *Nature Materials* **14**, 400, doi:10.1038/nmat4176 (2015).

10   Gül, Ö. *et al.* Hard Superconducting Gap in InSb Nanowires. *Nano Letters* **17**, 2690-2696, doi:10.1021/acs.nanolett.7b00540 (2017).

11   Beenakker, C. W. J. Quantum transport in semiconductor-superconductor microjunctions. *Physical Review B* **46**, 12841-12844, doi:10.1103/PhysRevB.46.12841 (1992).

12   Stanescu, T. D., Tewari, S., Sau, J. D. & Das Sarma, S. To Close or Not to Close: The Fate of the Superconducting Gap Across the Topological Quantum Phase Transition in Majorana-Carrying Semiconductor Nanowires. *Physical Review Letters* **109**, 266402, doi:10.1103/PhysRevLett.109.266402 (2012).

13   Mishmash, R. V., Aasen, D., Higginbotham, A. P. & Alicea, J. Approaching a topological phase transition in Majorana nanowires. *Physical Review B* **93**, 245404, doi:10.1103/PhysRevB.93.245404 (2016).

14   Liu, C.-X., Setiawan, F., Sau, J. D. & Das Sarma, S. Phenomenology of the soft gap, zero-bias peak, and zero-mode splitting in ideal Majorana nanowires. *Physical Review B* **96**, 054520, doi:10.1103/PhysRevB.96.054520 (2017).

15   Chang, W. *et al.* Hard gap in epitaxial semiconductor–superconductor nanowires. *Nature Nanotechnology* **10**, 232, doi:10.1038/nnano.2014.306 (2015).

6

Chapter

High mobility stemless InSb nanowires

Abstract *High aspect-ratio InSb NWs with high performance capabilities are sought for the implementation of advanced quantum devices. The growth of InSb NWs is challenging, generally requiring a stem of a foreign material for nucleation. Such a stem tends to curb the length of InSb NWs and its material gets incorporated in the InSb segment. Here, we report on the growth of chemically pure stemless InSb NWs tens of microns long. Using a selective-area mask in combination with gold as a catalyst allows us to completely omit the stem, thus demonstrating that InSb NWs can grow directly from the substrate. The introduction of the selective-area mask gives rise to novel growth kinetics, demonstrating high growth rates and complete suppression of layer growth on the mask for Sb-rich conditions. The purity of these NWs yields significant enhancement in electron mobility as compared to InSb NWs grown on stems.*

6.1 Introduction

InSb nanowires (NWs) have sparked interest in the past few years due to their potential to host Majorana zero modes (MZMs),[1-3] prime candidates for topological quantum computing.[4-7] InSb has further unfolded as an ideal material for spin-orbit quantum bits (qubits)[8-11] due to its giant Landé *g*-factor (≈ 51) and strong spin-orbit interaction (SOI).[12] Additionally, InSb offers other unique properties such as a large bulk electron mobility of 77000 Vs/cm² at 300 K,[12,13] and provides a convenient platform for superconductor-semiconductor hybrid devices[14,15]. Many of these applications require NWs longer than a few microns. Specifically, to fully explore Majoranas it would be advantageous if the hybrid devices contain multiple microns-long superconducting islands.[16,17] It is important that the islands are long enough compared to the characteristic coherence length associated with the superconductor to be able to conserve the Majorana parity.[18]

Despite their ability to outperform the majority of III-Vs in many aspects, synthesis of long InSb free-standing nanostructures has proven to be rather challenging. The challenges associated with growing InSb NWs are primarily due to the low vapor pressure of antimony (Sb) of about 2 x 10⁻⁴ Torr at 450 °C. In particular, when in excess, the evaporation of Sb is less favorable causing it to stick to epitaxial surfaces and causing parasitic island growth.[19] Importantly, Sb is a surfactant known to change the wetting properties of surfaces, which is likely to impede NW growth and affect the migration length of adatoms. More specifically, instead of being pushed up to promote NW growth, the metal catalysts are rather propelled on the substrate surface, leaving behind a streak of grown material.[19] To realize InSb NWs they have to be grown on a NW stem made of a foreign material.[19-25]

In this chapter I will report the growth of stemless InSb NWs directly on an InSb substrate. We show that with the optimized substrate design parameters, the growth of NWs can be accomplished. The length of these stemless wires reaches tens of microns, outperforming their stemmed counterparts in dimensions and electronic properties. We perform low-temperature mobility measurements and extract record mobilities for bottom-up grown InSb nanowires. Furthermore, from measurements in quantum point contact (QPC) formed in InSb nanowire we estimate the system parameters, which are important for realizing topological quantum computing (Rashba spin-orbit coupling, Landé *g*-factor).

6.2 Results

6.2.1 Growth kinetics of stemless InSb nanowires

The inhibition of vertical growth is attributed to a decrease in contact angle between the catalyst droplet and the substrate in the presence of Sb (Figure 6.1a). Alternatively, one can circumvent the contact angle issue by nucleating InSb NWs on top of a NW stem of a different material;[19-21,23-25] thereby, inhibiting the metal catalyst from spreading due to the small footprint of the stem (Figure 6.1b-d).
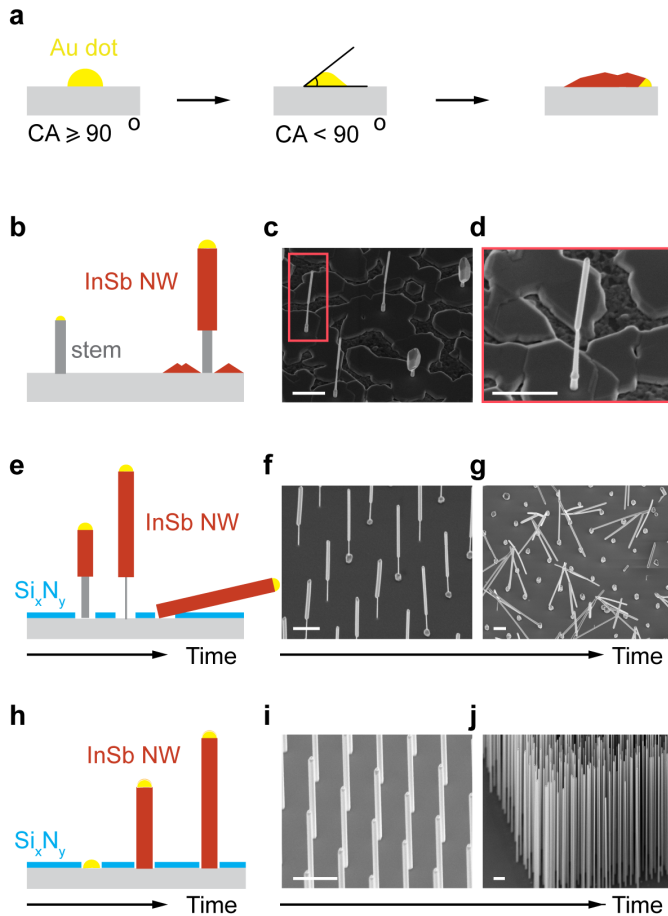
Figure 6.1 | Stem omission and stemless InSb NW growth. a, Schematic illustration of correlation between the Au catalyst particle contact angle before, upon introduction of Sb and after the growth of InSb by propelling Au. **b,** A NW stem (of a foreign material) allows for the growth of InSb NWs. **c,** SEM images show InSb NW growth on a stem. A red rectangle magnified in **d** highlights the presence of layer growth on the substrate. **e,** In order to suppress layer growth, a Si_xN_y mask is used. **f,** The growth of stem/InSb NWs on a masked substrate. **g,** Increased growth duration, evaporation of stems and collapsed InSb NWs. **h,** InSb NW growth directly from the substrate with a Si_xN_y mask. **i-j,** Growth of longer InSb NWs is achieved. All SEM images are taken at 30º-tilted view. All scale bars correspond to 1 μm.

However, the growth of a parasitic InSb layer is challenging for realizing high yield of these NWs. Employing the selective-area (SA) mask similar to the work of Dalacu *et al.*[26] allows us to attain a good yield (Figure 6.1e-g). The downsides of this technique are, however, the incorporation of the stem material into the InSb NW segment,[20] and the length limitation of the InSb NW,[21,23] to a maximum of approximately 3.5 μm (Figure 6.1f). In particular, the stem, in this case made of indium phosphide (InP), evaporates during the InSb growth; and hence, is not able to maintain the weight of the growing InSb NW (Figure 6.1g). This length restriction is likely to limit their utilization in complex devices. Specifically, longer NWs could reduce the overlap between MZMs at the NW ends by spatially separating them[18] and would also offer the possibility to accommodate multiple superconducting islands.[15] Here we demonstrate a method that enables InSb NWs to grow directly from the substrate without requiring a foreign NW stem. Stem omission is realized by positioning catalyst droplets within restricted openings of a SA mask, as shown in Figure 6.1h. As a consequence, Sb is impeded from changing the surface energy of the epitaxial substrate; thus, ensuring a catalyst contact angle that permits NW growth. Introduction of the silicon nitride (Si_xN_y) mask not only completely suppresses parasitic layer growth (see Figure 6.1i and Figure 6.1j) but also unveils entirely different growth kinetics and adatom diffusion behavior in contrast to stemmed growth on unmasked substrates, as will be investigated in this chapter.

To understand the emerging kinetics of the SAG-VLS InSb NW growth, arrays of gold catalyst particles with different diameters spaced at varying distances are defined using electron beam lithography on an InSb(111)B substrate covered with a 20 nm Si_xN_y layer. Gold particles are positioned within differently sized nano-openings in the Si_xN_y (see row 1 in a matrix arrangement Figure 6.2a). The diameter of the openings is varied by means of wet-etching the Si_xN_y (details on substrate fabrication can be found in Appendix Subsection 6.4.1). The interplay between gold particle diameter and mask opening brings about new growth kinetics. To investigate the evolution of the wire dimensions, we vary the mask opening diameter, denoted here by D_{mask}, for a given droplet size $D_{Au} = 30$ nm and preform a growth time series. Nucleation of these wires is consistent with selective-area nucleation at edge sites. In particular, during the early stages of growth, we discern that the gold particle is consistently pushed to the edge of the opening (see Appendix Figure 6.6). This phenomenon persists until the opening is entirely covered by grown InSb. When that is achieved, the gold particle is centered with respect to the mask opening as the nanowire is filling the size of the opening in the substrate, already observed after 1 hour of growth (see row 2 in a matrix arrangement Figure 6.2a). The yield of these wires is limited by the sliding of gold droplets under the mask during premature stages of growth, consequently, leading to missing wires or non-homogeneous wire dimensions within one NW array (see Appendix Figure 6.7). This non-uniformity occurs because the droplet is sometimes split, leading to different NW growth rates.
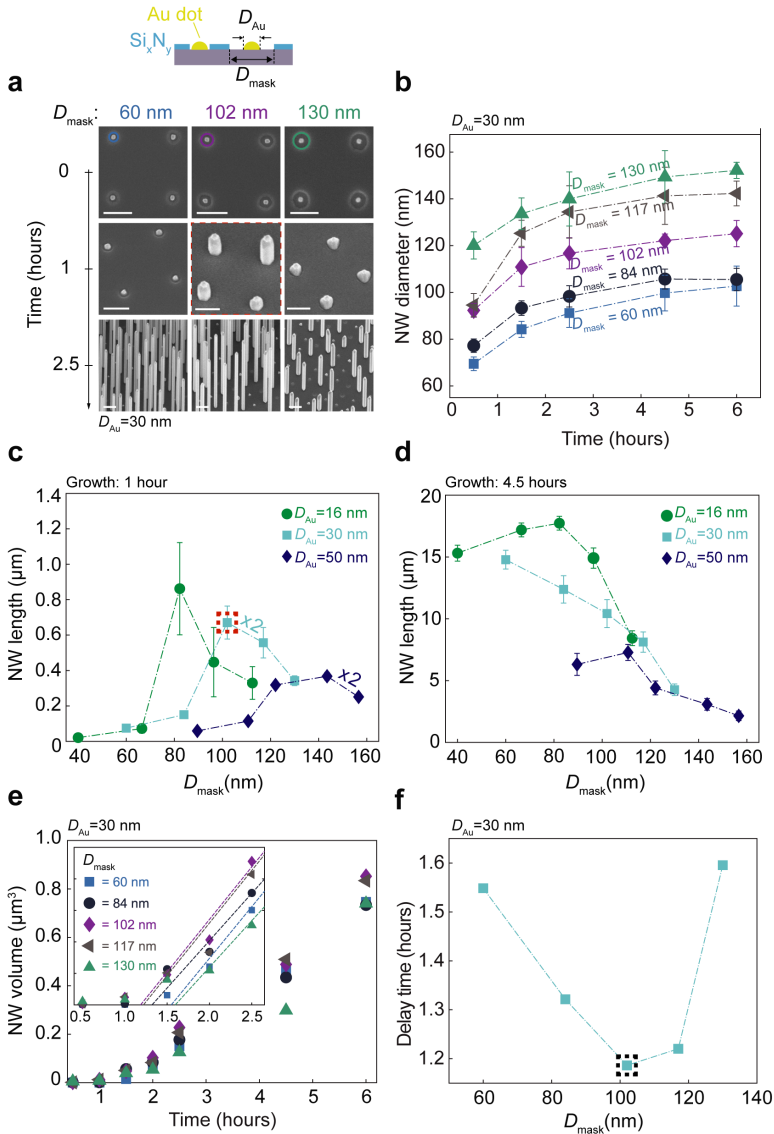
Figure 6.2 | Effect of gold catalyst diameter (D_{Au}) and mask opening (D_{mask}) on NW growth. a, SEM images for a fixed D_{Au}=30 nm, are organized in a matrix. D_{mask} increases along a row (left to right) and time increases along a column (top to bottom). The scale bar is 0.25 μm for row 1 and 2, and 0.5 μm for row 3. **b**, NW diameter increase with time and D_{mask}. The NW diameter exceeds D_{mask} after 1.5 hours. The gold catalyst diameter is D_{Au} = 30 nm. **c**, NW length dependence on D_{mask} for different D_{Au} after 1 hour of growth (curves for D_{Au} = 30 nm and 50 nm are multiplied by two for display purposes). **d**, The same dependent variables as in panel **c** after 4.5 hours of growth. **e**, NW volume increase with time for various D_{mask}. The gold catalyst diameter is D_{Au} =30 nm. Inset: Evolution of NW volume proceeds non-linearly with time during the first 1.5 hours, after which the growth rate becomes linear, as fitted by dashed lines in the inset. The linear fit that intersect the x-axis first, indicates the fastest crossover to the linear regime. **f**, The x-axis intercepts from **e** are shown as a function of D_{mask}, yielding the fastest crossover (minimum) for D_{mask} = 102 nm, which corresponds to the peak in panel **c** and SEM image in panel **a** indicated by the red dashed rectangle.

Furthermore, we observe that the NW diameter increases with mask opening size and growth time. In addition, regardless of the mask opening size, after 1.5 hours of growth, the NW diameter already exceeds D_{mask} (Figure 6.2b). These observations indicate the presence of radial InSb growth. The complete absence of tapering in these wires together with the atomically at side facets, however, signifies that if a new layer is formed it fully grows along the length of the NW. The low probability of nucleation on (110) side-walls commonly known for InSb NWs,[20,21] implies that the formation energy for a new step-edge is very high. With regards to length, after one hour of growth, we observe that NWs grown from medium-sized openings (D_{mask} = 102 nm) grow the longest (≈ 350 nm) (see row 2 – column 2 in a matrix arrangement Figure 6.2a). Wires growing from the smallest opening (D_{mask} = 60 nm), however, barely outgrow the mask thickness, as shown in a row 2 – column 1 of Figure 6.2a. We would have expected wires grown from the smallest opening to have yielded the tallest NWs for a given growth time, for a diffusion limited growth process where the wire volume is constant. Accordingly, we propose a different mechanism governing the nucleation and growth of these wires, causing NWs arising from small openings to experience an axial growth delay.

We further investigate this delay by including different gold sizes, D_{Au} = 16 nm and D_{Au} = 50 nm, respectively (Figure 6.2c). After one hour of growth, a delay in axial growth indeed exists for all gold particle sizes, manifested by a peak in NW length for wires originating from medium-sized openings as visible in Figure 6.2c. In particular, for D_{Au} = 16 nm, NWs grown for an hour from D_{mask} < 82 nm have a length of around 72 nm, while those arising from D_{mask} = 82 nm are ~0.86 nm long. After 4.5 hours of growth (see Figure 6.2d), this peak becomes less distinguishable and uniquely shifts towards smaller openings for different gold dot diameters. More specifically, this shift is observed for wires grown from D_{Au} = 30 nm and D_{Au} = 50 nm, as shown in Figure 6.2d. In contrast, NWs catalyzed by D_{Au} = 16 nm gold dots maintain a peak for the same mask opening after 4.5 hours, albeit the difference in NW length between wires growing from smaller D_{mask} becomes much less with time. Whether the peak in NW length shifts or persists, could be resulting from an interplay between two competing effects: the difference in NW length (ΔL) originating from the axial growth delay; and, the volume effect, which results in a slower axial growth rate for thicker wires (see Appendix Figure 6.8). Therefore, a peak towards smaller D_{mask} implies that as the growth time extends longer, the volume effect dominates, yielding the shortest wires from the biggest openings. A peak persistence, on the other hand would mean that ΔL was too large, causing the effect of the axial growth delay to linger longer.

This delay is captured in more detail in the Figure 6.2e where nanowire volume is plotted as a function of time for varying D_{mask} and constant D_{Au} = 30 nm. The NW growth rate is non-linear in the first ≈ 1.5 hours. After that, the volume increases linearly with time as visible in the inset of the Figure 6.2e. A linear fit of these data points shows that all NWs (irrespective of D_{mask}) grow with more or less the same

rate (slope: 0.159 ± 0.0093 μm^3). The point at which these linear curves intersect the x-axis, thus, reflects which opening diameters yield the least axial growth delay (see Figure 6.2f for those data points). The linear fit for D_{mask} = 102 nm intersects the x-axis the earliest, coinciding with the peak in NW length of Figure 6.2a and Figure 6.2c (data point encircled with the red dashed rectangle).

These unique growth dynamics could be attributed to the distinct droplet response to different mask openings. Particularly, during the early stages of nucleation, the gold particle needs to uptake precursors in order reach an optimum alloy content and thus volume. Due to the limited space available to the particle in small mask openings, it cannot reach a stable alloy structure and an optimum wetting configuration (contact angle) as fast as its counterparts from bigger mask holes. Thereby, delaying axial growth, as depicted in Figure 6.2.

6.2.2 The effect of the trimethyl-antimony flow

After capturing the effect of substrate patterning on InSb NW growth kinetics, we turn our attention to the impact of growth parameters on these wires. Thus, in what follows we will discuss the effects of precursor flows on NW growth kinetics, more specifically the impact of *trimethyl*-antimony (TMSb) flow on the NW growth dimensions and adatom diffusion. We vary the TMSb molar fraction, while keeping the TMIn flow constant and note the evolution of NW dimensions accordingly. As outlined in Figure 6.3a, a slight increase in TMSb molar fraction causes significant change in both NW diameter and length. In accordance with these plots one could argue that there is a threshold amount of TMSb flow required beyond which InSb wires grow with a high aspect ratio. The considerable difference in NW length between low and high TMSb flows can possibly be attributed to the axial growth rate being group-V limited, which is unique to antimonide-based NWs and has been reported for InSb NWs on stems and gallium antimonide (GaSb) NWs on GaAs segments[21,27] on bare substrates. Predominantly, for other III-V NWs, group-III precursors are the rate-limiting elements. Nonetheless, we would like to propose a different mechanism, which could be governing the growth kinetics of SAG-VLS InSb NWs. We observe, that if the sample is heated to the growth temperature, under a flow of hydrogen (H_2), parasitic growth islands appear on the SA mask. If, however, we heat up the sample under a flow of TMSb, we notice that these parasitic islands are completely suppressed and selectivity is enhanced (see Figure 6.3b). Different experiments have been performed to ensure that the parasitic islands are not due to surface contamination, including varying the TMSb molar fraction of the heat-up flow. In fact, we do observe a reduction in nucleation points on the mask with increased TMSb flow during heat up. This observation would indicate that TMSb has a direct influence on the diffusion length of indium (In) precursor. More generally, TMSb increases the diffusion length of In, inhibiting the formation of In droplets on the Si_xN_y mask. Parasitic islands are also observed if the sample is heated up under H_2 and the TMIn is opened 30 seconds before growth starts. In contrast, if

the sample reaches the growth temperature under a flow of TMSb, parasitic growth on the mask is absent, thus confirming that parasitic deposition is initiated by In droplets on the SA mask. Accordingly, no or low flows of TMSb cause In to more readily stick to the SA mask and reduce selectivity of the amorphous mask.
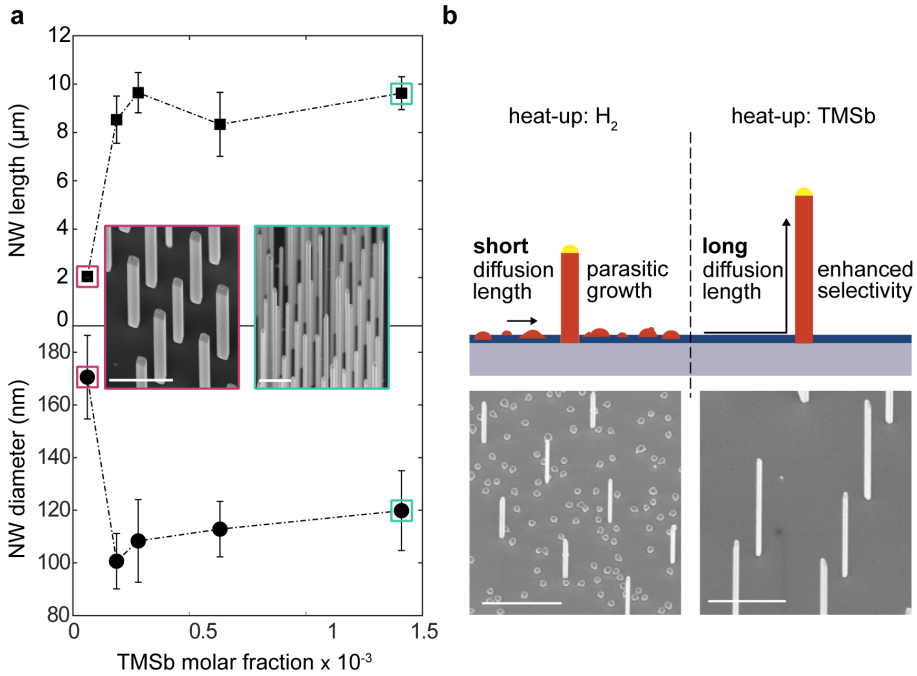
Figure 6.3 | Effect of TMSb molar fraction on InSb NW growth. a, A reduction in NW diameter and an increase in NW length are achieved in response to higher TMSb flow. Representative 30°-tilt SEM images at the lowest and highest TMSb molar fractions reflect the improved aspect ratio (length/diameter). Scale bars corresponds to 1 μm. **b**, Schematic depiction and 30°-tilt SEM images of a TMSb flow effect on precursor diffusion length. Left, heat-up under hydrogen leads to a short diffusion length reflected in parasitic growth on the SA mask. Right, sample heat-up under TMSb flow enhances selectivity by entirely suppressing nucleation on the mask. The growth time was 3 hours. Scale bars are 2 μm.

These observations stand in stark contrast to reports on InSb NWs on stems grown on bare substrates, where layer growth is always present. Actually, these studies even report that an increase in V/III ratio eventually reduces the NW growth rate, because of favored parasitic growth on the substrate surface.[21] The growth parameter window seems to be much larger for SA-VLS stemless InSb NWs.

Based on these observations, we thus conclude that In is the rate limiting precursor. The slight increase in diameter for the highest examined TMSb molar fraction in comparison with the minimum observed diameter for a molar fraction of 1.87×10^{-4} could be allotted to excess Sb reducing the nucleation barrier on NW side-facets, resulting in radial growth without compromising NW length. Upon examining the NW volume dependence on pitch, we extract a surface diffusion length on the Si_xN_y to be $\approx 2 \, \mu m$ (see Appendix Figure 6.9). The complete absence of tapering, however,

indicates rather large diffusion lengths for incoming adatoms on the smooth 110 side-facets.[19,21]

6.2.3 Atom probe tomography of stemless nanowires

In terms of crystal structure both types of InSb NWs, stemmed and stemless, are comparable, demonstrating pure zinc blende crystal structure without defects, as verified by transmission electron microscopy (see Appendix Figure 6.10). The chemical purity of stemless and InSb wires on stems is studied by atom probe tomography (APT) analysis. As indicated in Figure 6.4, APT data shows four orders of magnitude reduction in arsenic (As) incorporation, going from $5.5 \pm 0.49\%$ in InSb NWs on stems to $0.00063 \pm 0.000216\%$ in the stemless wires. With these high levels of As in the NWs on stems, these wires are rather an alloy of $InSb_{1-x}As_x$ than As being merely an impurity contaminant. The presence of As in the wires is due to the growth of short segment of indium arsenide (InAs) NW (~200 nm) before growing InSb. Reduction in phosphorus (P) contamination is also evident for stemless wires, showing two orders of magnitude less in P incorporation. Particularly, a decrease from $0.107 \pm 0.015\%$ in InSb on stems to $0.00126 \pm 0.000535\%$ in stemless wires is deduced. The extreme low concentrations of P and As present in the stemless NWs are likely ascribed to background levels in the reactor chamber.

6
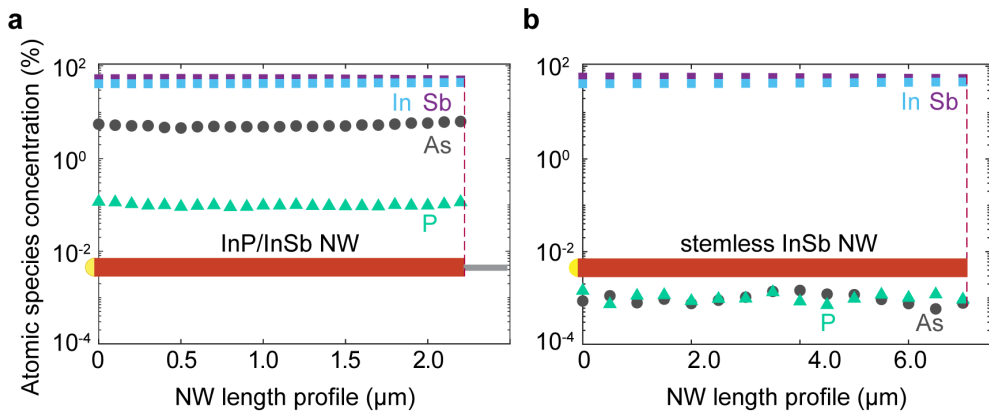
Figure 6.4 | Atomic species concentration along an InSb NW for **a**, stemmed and **b**, stemless growth using atom probe tomography. A 50:50 concentration of In:Sb is observable in both graphs in accordance with the 1:1 ratio of III-V compounds. Significant reduction in arsenic (As) and phosphorus (P) incorporation in the stemless wires is realized.

6.2.4 Mobility measurements

To quantify the effects of impurity incorporation on the electronic properties of the NWs, we extract the electron mobility, quantized conductance, Landé g-factor and the spin-orbit energy. To obtain the electron mobility μ of the nanowire devices, a field-effect transistor (FET) measurements are conducted (inset Figure 6.5a) by accurately reproducing the conditions used in Reference 28. We fabricated 15 nanowire-FET devices (nanowire diameter in the range of 130 nm – 190 nm) with Ti/Au leads on heavily p-doped Si/SiO$_2$ substrates to enable back-gate functionality. The source-drain contact separations are either $L = 1$ µm or 2 µm in order to ensure the diffusive long-channel transport regime. Hence the current I as a function of back-gate voltage V_{BG} and DC-bias voltage V_{DC} can be modelled by:

$$I(V_{BG}, V_{DC}) = \frac{V_{DC}}{\frac{L^2}{\mu C (V_{BG} - V_{th})} + R_c} \tag{6.1}$$

The saturation current is limited by the series resistance R_c, which includes the contact, filter and line resistances. The current pinch-off is reached at the threshold voltage V_{th}. The capacitance C is evaluated via a 3D Laplace solver including a correction factor due to quantum confinement (as described in Reference 28).

Gate-voltage sweeps $I(V_{BG})$ for both channel lengths are depicted in Figure 6.5a. Field-effect mobilities are extracted from fits of the pinch-off curves (red dashed lines). The weighted average of the mobility for the 15 devices yields μ = 44000 cm^2/Vs, accounting for the average of forward and reverse sweep directions. The obtained mobilities vary between ~ 34000 cm^2/Vs and 57000 cm^2/Vs (details are in Appendix Table 6.1), independent of the employed channel length. The mobilities are significantly higher than obtained in previous studies on InSb nanowires[28] and InAs nanowires[29,30] where the average lies around 25000 cm^2/Vs for ≈ 100 nm nanowire diameters. The lower mobility measured in InAs NW devices is likely attributed to surface electron accumulation, which enhances surface scattering. Surface adsorbates are thus known to strongly impact the field effect mobility. In this work, adsorbates are efficiently removed from the nanowire surfaces by evacuating the sample space for 65 hours before measurements, similar to Reference 28.

The highest mobilities in the order of 10^5 cm^2/Vs are measured for InSb in conventional two-dimensional electron gases (2DEGs)[31,32], where the InSb quantum is protected by epitaxial barrier layers. However, these barrier layers are incompatible with superconductor-semiconductor hybrid devices because they impede the exchange of carriers between the quantum well and the superconductor. Moreover, spin-orbit coupling, which is crucial for applications in spintronics and topological quantum computing, is generally more pronounced in bottom-up III-V nanowires compared with their 2DEG counterparts.[33]

The high mobilities reported for our nanowires translate into particularly long mean free paths over which the transport is ballistic. Accordingly, the conductance is expected to vary in quantized steps of e^2/h as a function of top-gate voltage at finite magnetic field, which indicates the stepwise depopulation of the one-dimensional subbands.[30,34,35] This can be seen for instance in Figure 6.5c and Figure 6.5d, where a 170-nm-wide top gate is used to form a local quantum point contact (QPC).
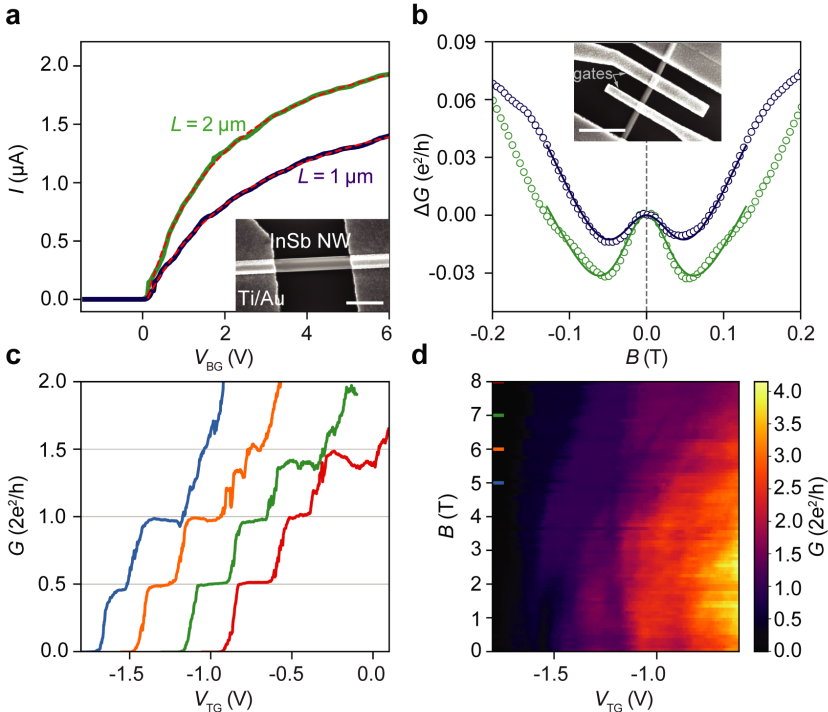
Figure 6.5 | **Quantum transport characterization. a**, FET measurements at $V_{DC} = 10$ mV for two nanowires of different lengths L. The red dashed lines are fits according to Equation (6.1), which yield $\mu = 41000$ cm²/Vs (blue trace) and $\mu = 45600$ cm²/Vs (green trace). The inset shows an exemplary nanowire device and the scale bar is 500 nm. **b**, WAL magnetoconductance correction (G) at $T = 0.3$ K (excitation voltage $V_{AC} = 20$ μV) with data for both sweep directions being averaged. The fits (solid curves) are performed by utilizing the quasi-classical WAL model[36]. The back-gate voltage range for the blue curve is 2 V to 6 V and for the green curve 6 V to 10 V. The inset shows an exemplary nanowire device and the scale bar is 1 μm. **c**, QPC conductance at $V_{dc} = 1.0$ mV. Due to the contact and line resistances and the unmodulated nanowire segments a series resistance of $R_c = 13.5$ kΩ is subtracted, so that the conductance plateaus align with multiples of e^2/h. Here, the back-gate voltage is $V_{BG} = 7.5$ V and the temperature is $T = 6$ K. The gate traces are shifted in V_{TG} for clarity and the corresponding field values where the linecuts are taken are indicated by the colored dashes in panel **d**. At $B = 5$ T (blue curve) the degeneracy between two subbands with opposite spin is evidenced by the fact that the plateau at $1.5 \cdot 2e^2/h$ vanishes. **d**, QPC conductance (G) as a function of V_{TG} and B.

The evolution of the conductance plateaus as a function of the applied magnetic field corresponds to the Zeeman splitting $E_Z = g\mu_B B$ (with the Bohr magneton μ_B) and the magnetic confinement causes a shift in the one-dimensional subband energies.

The extracted Landé g-factor for the first subband is 38, in agreement with previous reports for InSb nanowires.[34,37]

An important prerequisite for realizing topological quantum computing in one-dimensional NWs is a large Rashba spin-orbit parameter. Superconductivity and a uniaxial spin-orbit coupling in conjunction with an external magnetic field perpendicular to the spin-orbit field allow for the formation of quasiparticle excitations, so-called Majorana bound states, at the opposite nanowire ends.[5,6] The magnitude of the topological energy gap that protects these zero-energy states from poisoning by higher energy quasiparticles is enhanced by increasing the spin-orbit energy. Here, we extract the Rashba parameter (α_R) from phase-coherent transport measurements by investigating the weak antilocalization effect (WAL). In Figure 6.5b, the magnetoconductance correction at temperature $T = 0.3$ K is presented for two different back-gate voltage intervals. The blue trace refers to the back-gate voltage range from 2 V to 6 V, while the green trace corresponds to higher voltages between 6 V and 10 V. The solid lines represent the fits using the quasi-classical WAL model from Kurdak et al.[38] The model parameters for magnetic and spin dephasing were introduced for hexagonal nanowires in Reference [36] (see Appendix Subsection 6.4.6). Upon increasing the back-gate voltage, the spin-orbit energy is slightly enhanced from $E_{SO} = 0.17$ meV to 0.18 meV, which corresponds to a change in the Rashba parameter from $\alpha_R = 0.43$ eVÅ to 0.45 eVÅ. The spin-orbit energy derived from the weak antilocalization effect is quantitatively in line with previous studies on InSb nanowires grown from InP stems.[36] The extracted phase coherence length l_φ is approximately 480 nm and is nearly identical for the two curves. A second device is presented in the Appendix Figure 6.12 yielding a comparable l_φ and a higher Rashba parameter of $\alpha_R = 0.64$ eVÅ. For both devices, the Rashba parameters exceed α_R extracted for two-dimensional InSb heterostructures by more than one order of magnitude.[38]

6.3 Conclusions

We demonstrated a method to grow stemless InSb nanowire with high aspect ratios. Moreover, these InSb NWs grown by SAG-VLS technique wires are of exceptional chemical purity, which is reflected by the measured high mobilities and quantized conductance – the hallmark of one-dimensional transport. These nanowires can be used for MZM experiments utilizing multi-island configurations in Majorana assisted qubits.

6.4 Appendix

6.4.1 Substrate fabrication recipe

InSb(111)B substrates prepatterned using e-beam lithography were used for the growth of InSb stemless nanowires.

Processing steps are listed:
- Plasma-enhanced chemical vapor deposition (PECVD) of 20 nm Si_xN_y mask (300 °C, Oxford Instruments Plasmalab System 100);
- Spin coat the wafer with primer AR 300-80 at 4000 rpm for 60 seconds, bake at 180 °C for 2 minutes;
- Spin coat the wafer with resist AR-P 6200.04 at 4000 rpm for 60 seconds, bake at 150 °C for 3 minutes;
- Write dot patterns using e-beam lithography varying the dot size (16 – 50 nm) and pitch (0.25 – 4 μm) (dose 1650 – 2750 μC/cm²);
- Developing in AR 600-546 for 60 seconds, stopper AR 600-60 for 30 seconds, rinse IPA for 60 seconds;
- Opening the holes in Si_xN_y mask with buffered oxide etch (NH_4F:HF=7:1) for 14 – 25 seconds;
- Rinse with ultra-pure water (UPW);
- Evaporation of 8 nm Au with an evaporation rate of 1 Å/s (Electron-beam evaporator);
- Lift-off in PRS3000 at RT for 1 hour, ultrasonic agitation in acetone for 10 minutes, rinse in IPA for 10 minutes;
- Organic residues removal by O_2 plasma (10 minutes, 55 sccm O_2, 300 W plasma power).

6

6.4.2 MOVPE growth of stemless InSb nanowires

Growth in this work was done using a horizontal Aixtron 200 metal-organic vapor phase epitaxy (MOVPE) reactor. The samples were heated to the desired growth temperature of 495 °C by infrared lamps. The used precursors were trimethyl-indium (TMIn) and trimethyl-antimony (TMSb), where the TMIn molar fraction was kept constant at 1.95×10^{-7} and the TMSb was varied from 6.17×10^{-5} to 1.41×10^{-3}. The samples were heat up and cooled down under a flow of TMSb. The growth time was varied from 5 minutes to 6 hours. The carrier gas was H_2 and during growth the reactor pressure was kept constant at 50 mbar and a total volume of 6000 liters.

6.4.3 Growth and additional analysis of stemless InSb nanowires

Growth of SA-VLS wires is consistent with selective-area seeding, where nucleation is preferred at edge sites. Therefore we observe the Au particles being consistently pushed to the edge of the mask opening, as shown in Figure 1. Once the opening is completely filled with precipitated InSb, the Au droplet is centered with respect to the mask opening, showing InSb NW diameters larger than the Au diameter.
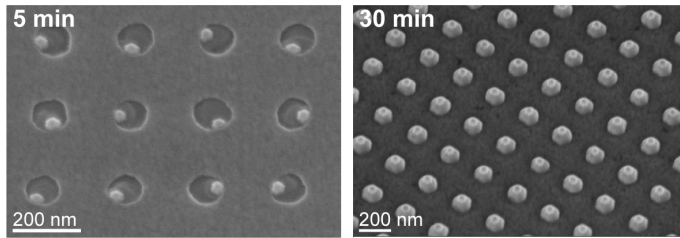
Figure 6.6 | Selective-area seeding at the Si$_x$N$_y$ edge sites. 30°-tilt SEM images showing different growth stages of InSb NWs from 5 to 30 minutes of growth. The growth is performed for samples with the biggest examined openings in the Si$_x$N$_y$ mask (~130 nm). The gold catalyst particle size D_{Au} is approximately 30 nm in diameter prior to growth. After half an hour of growth, the gold droplet seems to take the stable configuration of being positioned on top of the growing wires.

The yield of these wires is sometimes limited by gold dots sliding under the mask during early growth stages, apparent in Figure 6.7. The sliding is confirmed by closer examination yielding a brighter spot next to the holes with missing gold. This is observed for bigger inter-opening spacing. We believe that the gold sliding is caused by the Au-substrate reaction at the elevated temperatures (495 °C) during the heat up under a flow of TMSb.
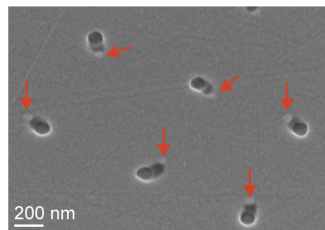
Figure 6.7 | Gold sliding. 30°-tilt SEM image of Au catalyst particles sliding under the selective-area mask, apparent by a bright dot next to the opening and empty holes and indicated by red arrows. The growth time was 5 minutes.

The volume effect refers to the fact, that if two objects have to grow to the same volume, the one with the smaller width (diameter) will grow higher. The schematic in Figure 6.8 serves as a visualization of the volume effect.

InSb NW
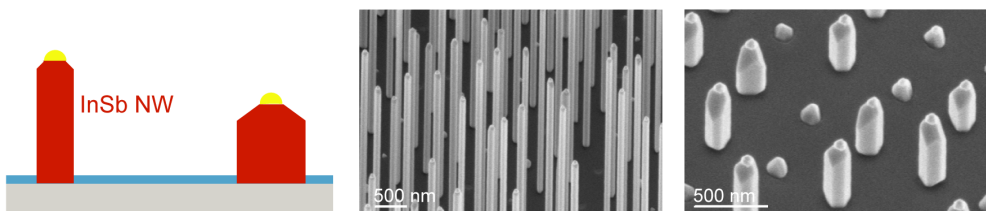
Figure 6.8 | Volume effect. Visualization of the volume effect, reflecting lower (higher) axial growth rates for bigger (smaller) diameter wires for a given volume.

Dependence of NW dimensions on pitch and extraction of surface diffusion length are discussed here. The data are collected from a growth run with low TMSb flow (χ_{TMSb} = 8.2 ×10^{-5}). Observing NW volume as a function of pitch (see Figure 6.9a), an increase in volume is barely discernible at a pitch of 2 μm. Thus, we can thus extract a surface diffusion length of about 2 μm. The plot of Figure 6.9b shows that the NW diameter is more or less independent of pitch, whereas the NW height is pitch dependent. More generally, the NW height slowly saturates with pitch.
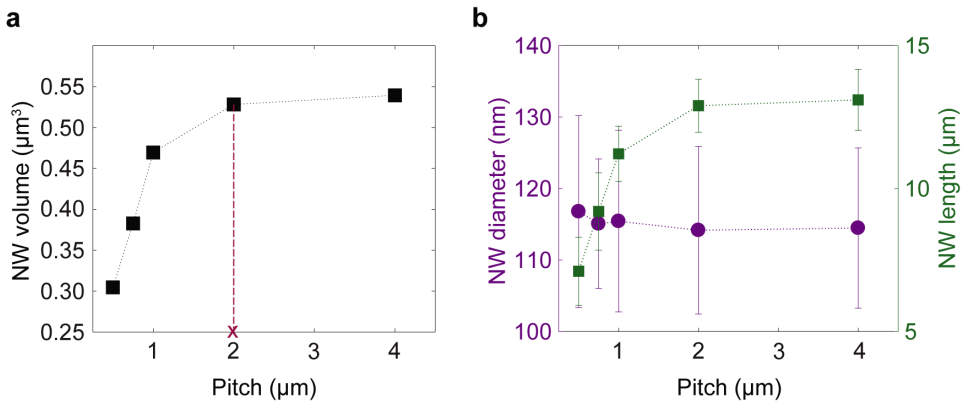
Figure 6.9 | Diffusion length. Dependence of NW dimensions on pitch. **a**, NW volume increases with pitch up until an inter-wire spacing of 2 μm. At this pitch, the NW volume saturates where a surface diffusion length is concluded. **b**, Plot of NW diameter and length against pitch. NW diameter is almost pitch-independent as opposed to NW length.
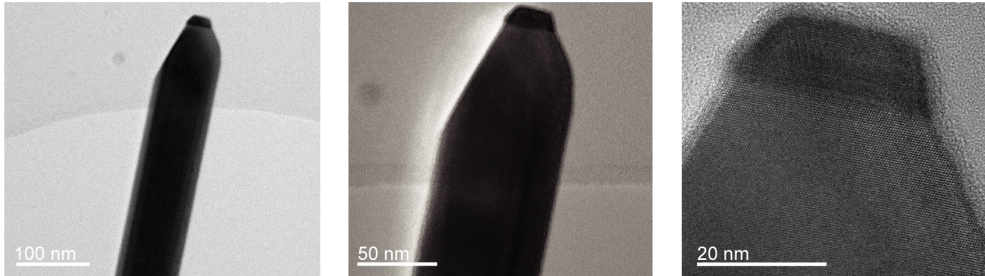
Figure 6.10 | TEM analysis. Bright-field TEM images and HR-TEM of stemless InSb NW with a gold catalyst on top. HR-TEM confirms pure zinc blende crystal of InSb NWs.

6.4.4 Device fabrication steps and measurement

The fabrication of mobility devices and QPC devices coincides in the first part. The substrates are made out of heavily p-doped Si covered by 285 nm of thermal SiO$_x$ via dry oxidation, onto which Ti/Au alignment markers are defined. The substrates are cleaned with 10 minutes of remote oxygen plasma at a pressure of 2 mbar and a power of 100 W.

- Nanowires are deterministically transferred by means of a nanomanipulator from the growth chip onto the substrate. Optical images are taken in order to facilitate the design of the device with respect to the alignment markers.
- A double layer of resist (PMMA 495K A6 and PMMA 950K A2) is spin-coated on the substrate and each layer is baked for 10 minutes at 175 °C.
- The pattern of the contacts is defined by e-beam lithography. Source and drain contacts are designed to be separated by a 'long' InSb channel of length 1 or 2 μm.
- Development in a solution of MIBK:IPA (1:3) for 1 minute, and in IPA for 1 minute.
- Prior to the metal deposition, the chip is cleaned with 2 minutes of remote oxygen plasma at 2 mbar and a power 100 W, and left for 30 minutes in a sulphur-rich ammonium polysulfide solution diluted in water with a ratio of 1:200 at 60 °C.
- The chip is rinsed thoroughly with water and quickly loaded in an e-gun evaporator. Here it is exposed to 30 seconds of helium (He) ion milling at a pressure of 1.6×10^{-2} mbar to facilitate the Ohmic contact between InSb and metal, which is then evaporated in the sequence of 10 nm of Ti, and 170 nm of Au.
- Lift-off in acetone for 2 hours at 50 °C.

Additional steps for QPC devices:

- 40 nm of SiN_x gate dielectric are sputtered onto the entire chip.
- Resist (PMMA 495K A4) is spin-coated and baked for 10 minutes at 175 °C.
- The pattern of the top gates is defined by e-beam lithography; the designed gate widths are in the range of 120-270 nm , comparable to the expected electron mean free path.
- Development in a solution of MIBK:IPA (1:3) for 1 minutes, and in IPA for 1 minutes.
- 20 nm of Ti and 210 nm of Au are deposited in an e-gun evaporator.
- Lift-off in acetone for 2 hours at 50 °C.

The chips are diced and mounted in a chip carrier. Transport measurements of the mobility devices are performed in a dip-stick in helium at $T = 4.2$ K , while QPC devices are loaded in a He-3 fridge with a base temperature of 300 mK. Prior to cooldown, the sample space with chips hosting mobility devices is pumped for about 65 hours similarly to Reference 28, in order to efficiently desorb adsorbates from the nanowires surface. The chips were imaged via SEM only after the measurement to minimize carbon contamination, in order to evaluate diameter and length of the nanowires.

We present here in Table 6.1 the detailed summary of all devices measured to evaluate the electron mobility in the stemless InSb nanowires. Two chips (which we call experimental runs 1 and 2) have been fabricated and measured. Prior to the cool down, the sample space was evacuated at room temperature for 48 and 65 hours for run 1 and 2, respectively. Onto these chips, nanowires grown from two different growth batches (RB2252 and RB2669) were transferred. We did not observe any significant difference between both evacuation times, and both growth chips. The mobility and threshold voltage values presented in Table 1 are weighted averages of the parameters extracted from the up and down back-gate sweep at 10 mV bias. The mobility values are between 3.42×10^4 Vs/cm^2 and 5.7×10^4 Vs/cm^2, with an average value of 4.37×10^4 Vs/cm^2.

Table 6.1 | **Summary of FET devices.**

Experimental run	NW batch	Diameter (nm)	Channel length (μm)	V_{th} (V)	$\mu \pm \delta\mu$ (cm²/Vs)
1	RB2252	191	1.92	-1.50	44430 ± 260
1	RB2252	168	1.90	-1.13	43640 ± 220
1	RB2252	182	1.96	-1.21	42740 ± 200
1	RB2669	175	1.87	-1.24	41240 ± 250
1	RB2669	169	1.89	-1.40	42900 ± 260
1	RB2669	159	1.94	-1.20	43910 ± 210
1	RB2669	171	1.92	-1.06	47960 ± 180
1	RB2669	166	1.92	-1.20	44150 ± 220
1	RB2669	165	1.87	-0.99	39820 ± 270
1	RB2669	183	1.75	-1.71	40000 ± 290
1	RB2669	186	1.92	-1.12	47760 ± 450
1	RB2669	189	1.93	-1.21	57000 ± 410
2	RB2252	141	1.94	0.10	41040 ± 190
2	RB2252	180	1.02	0.17	45590 ± 150
2	RB2252	138	1.95	0.45	34280 ± 90

6.4.5 Additional QPC data

Here, we present data of a QPC device different from the one reported in the main text. Similarly, the QPC is defined in a nanowire segment by means of a 215-nm-wide top gate (Figure 6.11a), while an electric field can be applied by the global back gate across the entire nanowire. The magnetic field is applied perpendicularly to the substrate and breaks the spin degeneracy of the subbands. In case of ballistic transport, this translates in the conductance rising in steps of e^2/h versus top-gate voltage. From the Zeeman splitting ($E_Z = g\mu_B B$) of the first subband (see Figure 6.11b), we extracted a value of the g factor of 38, comparable to what was reported in References [34,37].
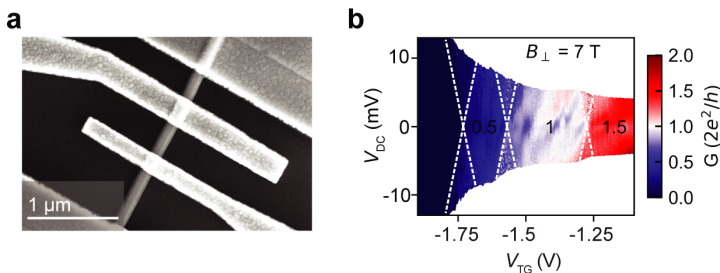
Figure 6.11 | **Additional QPC analysis. a**, InSb nanowire device comprising two top gates placed between two normal contacts that can be used to electrostatically create QPCs. **b**, Conductance as a function of bias voltage V_{DC} and top-gate voltage V_{TG} at $B = 7$ T. The top gate is 215-nm-wide and the measurement is performed at $T = 5$ K with $V_{BG} = 9$ V. The bias voltage is corrected for the voltage drop occurring due to additional series resistances.

6.4.6 Additional WAL data

Here, the weak antilocalization effect in the magnetoconductance data is modeled using the one-dimensional WAL formula of Kurdak *et al.*[38] given by:

$$\Delta G(B) = -\frac{e^2}{h}\frac{1}{L}\left[3\left(\frac{1}{l_\varphi^2} + \frac{4}{3l_{so}^2} + \frac{1}{l_B^2}\right)^{-1/2} - \left(\frac{1}{l_\varphi^2} + \frac{1}{l_B^2}\right)^{-1/2} \right.$$
$$\left. - 3\left(\frac{1}{l_\varphi^2} + \frac{4}{3l_{so}^2} + \frac{d}{l_e^2} + \frac{1}{l_B^2}\right)^{-1/2} + \left(\frac{1}{l_\varphi^2} + \frac{d}{l_e^2} + \frac{1}{l_B^2}\right)^{-1/2}\right] \tag{6.2}$$

The diffusion in the nanowire with the scattering length l_e has the dimensionality $d = 3$. Here, $l_e = v_F \tau_e$ is extracted from the threshold voltage V_{th}, which yields the Fermi velocity v_F, and the mobility μ, providing the characteristic scattering time τ_e, that are both determined from FET traces. The magnetic dephasing length l_B and the spin relaxation length l_{so} are given by[36]:

$$l_B = \sqrt{\frac{C_m}{d}\frac{l_m^4}{w_f^{\gamma_m}l_e^{2-\gamma_m}}} \tag{6.3}$$

$$l_{so} = \sqrt{\frac{C_s}{d}\frac{l_R^4}{w_f^{\gamma_s}l_e^{2-\gamma_s}}} \tag{6.4}$$

respectively, with $C_m = 22.3$, $\gamma_m = 3.174$ and $C_s = 8.7$, $\gamma_s = 3.2$ determined from Monte Carlo simulations of the dephasing along closed-loop electron trajectories in a hexagonal nanowire.[36] Here, w_f refers to the facet-to-facet nanowire diameter and $l_R = \hbar^2/m^*\alpha_R$ is the Rashba spin precession length.

Before fitting the magnetoconductance correction model of Equation (6.2) to the low-temperature transport data, the conductance background needs to be subtracted. To this end, for every magnetoconductance trace the average conductance at field values $|B| > 0.5$ T is subtracted. In Figure 6.12 the weak antilocalization effect is shown for another device different from the one in the main text, which is depicted in Figure 6.12a. Here, the magnetoconductance correction is averaged for a back-gate voltage interval from -1.5 V to 13.5 V. The orange curve in Figure 6.12 is the fit of the quasiclassical model in Equation (6.2), which yields a phase coherence length of $l_\varphi = 510$ nm, comparable to the device presented in the Figure 6.5. The extracted spin-orbit energy is $E_{so} = 0.37$ meV. This corresponds to a Rashba parameter of $\alpha_R = 0.64$ eVÅ.
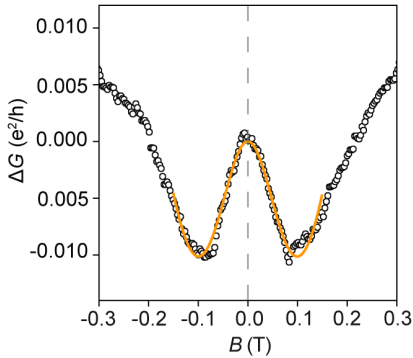
Figure 6.12 | **Additional WAL analysis.** Magnetoconductance correction for the nanowire device depicted in Figure 6.11a at $T = 0.3$ K. For the fit (solid line) the quasiclassical WAL model from Equation (6.2) is utilized.[36]

6.5 References

1   Mourik, V. *et al.* Signatures of Majorana Fermions in Hybrid Superconductor-Semiconductor Nanowire Devices. *Science* **336**, 1003-1007, doi:10.1126/science.1222360 (2012).

2   Deng, M. T. *et al.* Majorana bound state in a coupled quantum-dot hybrid-nanowire system. *Science* **354**, 1557, doi:10.1126/science.aaf3961 (2016).

3   Zhang, H. *et al.* Quantized Majorana conductance. *Nature* **556**, 74, doi:10.1038/nature26142 (2018).

4   Kitaev, A. Y. Unpaired Majorana fermions in quantum wires. *Physics-Uspekhi* **44**, 131 (2001).

5   Oreg, Y., Refael, G. & von Oppen, F. Helical Liquids and Majorana Bound States in Quantum Wires. *Physical Review Letters* **105**, 177002, doi:10.1103/PhysRevLett.105.177002 (2010).

6   Lutchyn, R. M., Sau, J. D. & Das Sarma, S. Majorana Fermions and a Topological Phase Transition in Semiconductor-Superconductor Heterostructures. *Physical Review Letters* **105**, 077001, doi:10.1103/PhysRevLett.105.077001 (2010).

7   Stern, A. & Lindner, N. H. Topological Quantum Computation—From Basic Concepts to First Experiments. *Science* **339**, 1179, doi:10.1126/science.1231473 (2013).

8   Nadj-Perge, S., Frolov, S. M., Bakkers, E. P. A. M. & Kouwenhoven, L. P. Spin–orbit qubit in a semiconductor nanowire. *Nature* **468**, 1084, doi:10.1038/nature09682 (2010).

9   Nadj-Perge, S. *et al.* Spectroscopy of Spin-Orbit Quantum Bits in Indium Antimonide Nanowires. *Physical Review Letters* **108**, 166801, doi:10.1103/PhysRevLett.108.166801 (2012).

10   Petersson, K. D. *et al.* Circuit quantum electrodynamics with a spin qubit. *Nature* **490**, 380, doi:10.1038/nature11559 (2012).

11   van den Berg, J. W. G. *et al.* Fast Spin-Orbit Qubit in an Indium Antimonide Nanowire. *Physical Review Letters* **110**, 066806, doi:10.1103/PhysRevLett.110.066806 (2013).

12   Madelung, O. *Semiconductors - Basic Data*. 2 edn, (Springer-Verlag Berlin Heidelberg, 1996).

13   Vurgaftman, I., Meyer, J. R. & Ram-Mohan, L. R. Band parameters for III–V compound semiconductors and their alloys. *Journal of Applied Physics* **89**, 5815-5875, doi:10.1063/1.1368156 (2001).

6

14   Deng, M. T. *et al.* Anomalous Zero-Bias Conductance Peak in a Nb–InSb Nanowire–Nb Hybrid Device. *Nano Letters* **12**, 6414-6419, doi:10.1021/nl303758w (2012).

15   Gazibegovic, S. *et al.* Epitaxy of advanced nanowire quantum devices. *Nature* **548**, 434, doi:10.1038/nature23468 (2017).

16   Aasen, D. *et al.* Milestones Toward Majorana-Based Quantum Computing. *Physical Review X* **6**, 031016, doi:10.1103/PhysRevX.6.031016 (2016).

17   Karzig, T. *et al.* Scalable designs for quasiparticle-poisoning-protected topological quantum computation with Majorana zero modes. *Physical Review B* **95**, 235305, doi:10.1103/PhysRevB.95.235305 (2017).

18   Domínguez, F. *et al.* Zero-energy pinning from interactions in Majorana nanowires. *npj Quantum Materials* **2**, 13, doi:10.1038/s41535-017-0012-0 (2017).

19   Borg, B. M. & Lars-Erik, W. Synthesis and properties of antimonide nanowires. *Nanotechnology* **24**, 202001 (2013).

20   Caroff, P. *et al.* High-Quality InAs/InSb Nanowire Heterostructures Grown by Metal–Organic Vapor-Phase Epitaxy. *Small* **4**, 878-882, doi:10.1002/smll.200700892 (2008).

21   Caroff, P. *et al.* InSb heterostructure nanowires: MOVPE growth under extreme lattice mismatch. *Nanotechnology* **20**, 495606 (2009).

22   Daniele, E. *et al.* InAs/InSb nanowire heterostructures grown by chemical beam epitaxy. *Nanotechnology* **20**, 505605 (2009).

23   Plissard, S. R. *et al.* From InSb Nanowires to Nanocubes: Looking for the Sweet Spot. *Nano Letters* **12**, 1794-1798, doi:10.1021/nl203846g (2012).

24   de la Mata, M. *et al.* Twin-Induced InSb Nanosails: A Convenient High Mobility Quantum System. *Nano Letters* **16**, 825-833, doi:10.1021/acs.nanolett.5b05125 (2016).

25   Pan, D. *et al.* Free-Standing Two-Dimensional Single-Crystalline InSb Nanosheets. *Nano Letters* **16**, 834-841, doi:10.1021/acs.nanolett.5b04845 (2016).

26   Dalacu, D., Kam, A., Austing, D. G. & Poole, P. J. Droplet Dynamics in Controlled InAs Nanowire Interconnections. *Nano Letters* **13**, 2676-2681, doi:10.1021/nl400820w (2013).

27   Jeppsson, M. *et al.* GaAs/GaSb nanowire heterostructures grown by MOVPE. *Journal of Crystal Growth* **310**, 4115-4121, doi:10.1016/j.jcrysgro.2008.06.066 (2008).

28   Gül, Ö. *et al.* Towards high mobility InSb nanowire devices. *Nanotechnology* **26**, 215202 (2015).

29   Ford, A. C. *et al.* Diameter-Dependent Electron Mobility of InAs Nanowires. *Nano Letters* **9**, 360-365, doi:10.1021/nl803154m (2009).

30   Heedt, S., Prost, W., Schubert, J., Grützmacher, D. & Schäpers, T. Ballistic Transport and Exchange Interaction in InAs Nanowire Quantum Point Contacts. *Nano Letters* **16**, 3116-3123, doi:10.1021/acs.nanolett.6b00414 (2016).

31   Thompson, P. E. *et al.* Use of atomic layer epitaxy buffer for the growth of InSb on GaAs by molecular beam epitaxy. *Journal of Applied Physics* **69**, 7166-7172, doi:10.1063/1.347608 (1991).

32   Lehner, C. A. *et al.* Limiting scattering processes in high-mobility InSb quantum wells grown on GaSb buffer systems. *Physical Review Materials* **2**, 054601, doi:10.1103/PhysRevMaterials.2.054601 (2018).

33   Kallaher, R. L., Heremans, J. J., Goel, N., Chung, S. J. & Santos, M. B. Spin-orbit interaction determined by antilocalization in an InSb quantum well. *Physical Review B* **81**, 075303, doi:10.1103/PhysRevB.81.075303 (2010).

34   Kammhuber, J. *et al.* Conductance Quantization at Zero Magnetic Field in InSb Nanowires. *Nano Letters* **16**, 3482-3486, doi:10.1021/acs.nanolett.6b00051 (2016).

35   van Weperen, I., Plissard, S. R., Bakkers, E. P. A. M., Frolov, S. M. & Kouwenhoven, L. P. Quantized Conductance in an InSb Nanowire. *Nano Letters* **13**, 387-391, doi:10.1021/nl3035256 (2013).

36   van Weperen, I. *et al.* Spin-orbit interaction in InSb nanowires. *Physical Review B* **91**, 201413, doi:10.1103/PhysRevB.91.201413 (2015).

37   Nilsson, H. A. *et al.* Giant, Level-Dependent g Factors in InSb Nanowire Quantum Dots. *Nano Letters* **9**, 3151-3156, doi:10.1021/nl901333a (2009).

38   Kurdak, Ç., Chang, A. M., Chin, A. & Chang, T. Y. Quantum interference effects and spin-orbit interaction in quasi-one-dimensional wires and rings. *Physical Review B* **46**, 6846-6856, doi:10.1103/PhysRevB.46.6846 (1992).

6

7

Chapter

Bottom-up grown two-dimensional InSb nanostructures

Abstract *Low-dimensional high-quality InSb materials are promising candidates for next-generation quantum devices due to the high carrier mobility, low effective mass and large g-factor of the heavy element compound InSb. Various quantum phenomena have been demonstrated in InSb 2DEGs and nanowires. A combination of the best features of these two systems (pristine nanoscale and flexible design) is desirable to realize e.g., the multi-terminal topological Josephson device. Here, we demonstrate controlled growth of two-dimensional nanostructures, nanoflakes, on an InSb platform. An assembly of nanoflakes with various dimensions and morphologies, thinner than the Bohr radius of InSb, were fabricated. Importantly, the growth of either nanowires or nanoflakes can be enforced experimentally by setting growth and substrate design parameters properly. Hall bar measurements on our nanostructures yield mobilities up to ~20.000 cm²/Vs and detect quantum Hall plateaus. This allows us to see our system as a viable nanoscale 2D platform for future quantum devices.*

7.1 Introduction

Realizations of topological quantum computing require low dimensional structures, where quantum mechanical phenomena are observed. Both two-dimensional (2D) and one-dimensional platforms are being researched for their potential to host topological phases of matter. Among the III-Vs, the heavy-element system InSb is the most suitable for topological quantum computing applications thanks to its high electron mobility, large Landé *g*-factor, and strong Rashba spin-orbit interaction.[1,2] InSb has a very small effective electron mass and thus a large Bohr radius of ~65 nm. As a result, quantum confinement energies are large and signatures of Majorana Zero Modes have been observed.[3-5] Moreover, the aforementioned characteristics make InSb a promising material for spintronics, infrared detectors, and thermoelectric power generation. However, synthesis of InSb devices with nanoscale perfection is not straightforward. The growth of high-quality thin films on insulating, crystalline substrates is difficult due to the large lattice parameter of InSb. A common workaround is to implement a buffer layer to moderate the lattice mismatch between the insulating, crystalline substrate and the InSb film.[6-10] Even though InSb quantum wells host two-dimensional electron gases (2DEGs) with high carrier mobility, these mobilities are usually not conserved in nanoscale devices due to fabrication damage (*e.g.*, from ion-beam etching and processing residues) of the complex structure of 2DEGs. High quality nanoscale devices have been fabricated based on bottom-up grown nanowires (NWs),[11-15] albeit with the obvious limitations in device complexity. Envisioned future quantum devices should combine the best of both worlds: the freedom of layout choices from quantum wells with the pristine nanoscale surfaces of NWs. A pathway to such devices is the combination of the latest *in-situ* shadowing techniques[14] with "free-standing" 2D systems, often referred to as "nanosails", "nanosheets" or "nanoflakes".[16,17] Growth of InSb nanoflakes on InP and InAs stem NWs has been reported.[16,17] In these works, a foreign material stem NW was used as a support for the growth, and the formation of either NWs or nanoflakes happened to a large extent at random. Based on the demonstrated growth of different nanoflake morphologies, we envision a large variety of possible device layouts based on smart inter-shadowing of nanoflakes and NWs grown at dedicated positions on the substrate. Examples are Josephson junction sets with

varying junction width or double-sided multi-terminal devices with both superconducting and Ohmic contacts – see Appendix Subsection 7.4.6 for examples. The main technological challenge for such devices is at the heart of this work: The deliberate growth of InSb nanoflakes and NWs at dedicated substrate positions *in the same growth run*.

In this chapter I will report the controlled bottom-up (epitaxial) growth of InSb nanoflakes directly on an InSb substrate platform without a foreign material stem. We show that with the appropriate growth parameters, the growth of nanoflakes or NWs can be triggered by fine tuning external parameters (droplet size and pitch). A nearly 100% yield of nanoflakes has been achieved from a carefully chosen parameter set. Additionally, we demonstrate a three-fold symmetric orientation between the nanoflakes and the substrate and provide an estimate of the statistical formation likelihood of example layouts (see Appendix). We perform low-temperature Hall measurements and find Quantum Hall plateaus, confirming the two-dimensionality of the system.

7.2 Results

7.2.1 Growth of InSb nanoflakes

We use e-beam lithography to pattern fields of gold catalyst droplets with varying diameter (D_{Au}) and pitch on InSb (111)B substrates. Additionally, a Si_xN_y mask promotes the selective-area vapor-liquid-solid growth. Further details on substrate fabrication and growth are given in Appendix Subsection 7.4.1. Samples have been analysed by scanning electron microscopy (SEM), (high-resolution) transmission electron microscopy (HR-TEM) and high-resolution scanning TEM (HR-STEM). In Figure 7.1a, we show an exemplary run where the yield of nanoflakes is high and the layer growth on the masked area is completely suppressed (see Chapter 6 for information on the selective growth method of InSb NWs). The regular pattern allows the implementation of an automated image analysis routine on SEM images to quantify the formation of nanoflakes *vs.* NWs, as shown in Figure 7.1b. The red asterisk and blue circle indicate a nanoflake and NW position, respectively. We have quantified the nanoflakes formation as function of total In- and Sb-precursor flow (Figure 7.1c), for different pitches (from 0.5 μm to 2 μm, Figure 7.1d), and for different D_{Au} (from 16 to 50 nm, Figure 7.1e). An increase of the nanoflake fraction with the total gas flow is evident from Figure 7.1c, and is shown quantitatively in Figure 7.1d. From Figure 7.1d, it is also clear that the nanoflake fraction increases with an increase of the pitch as an extra precursor supply is coming from the material diffusing over the Si_xN_y surface. Both parameters, a higher total flow and a larger pitch yield a similar trend implying that an increase in material availability per Au particle favors nanoflake formation. Therefore, we can infer that a high supersaturation of the Au particle is promoted due to an excess of precursors and is

responsible for the nanoflake formation. The data point highlighted by the square in Figure 7.1d (~ 90% yield of nanoflakes, the other 10% being NWs) corresponds to Figure 7.1a and Figure 7.1b - the highest total gas flow and largest pitch studied here.
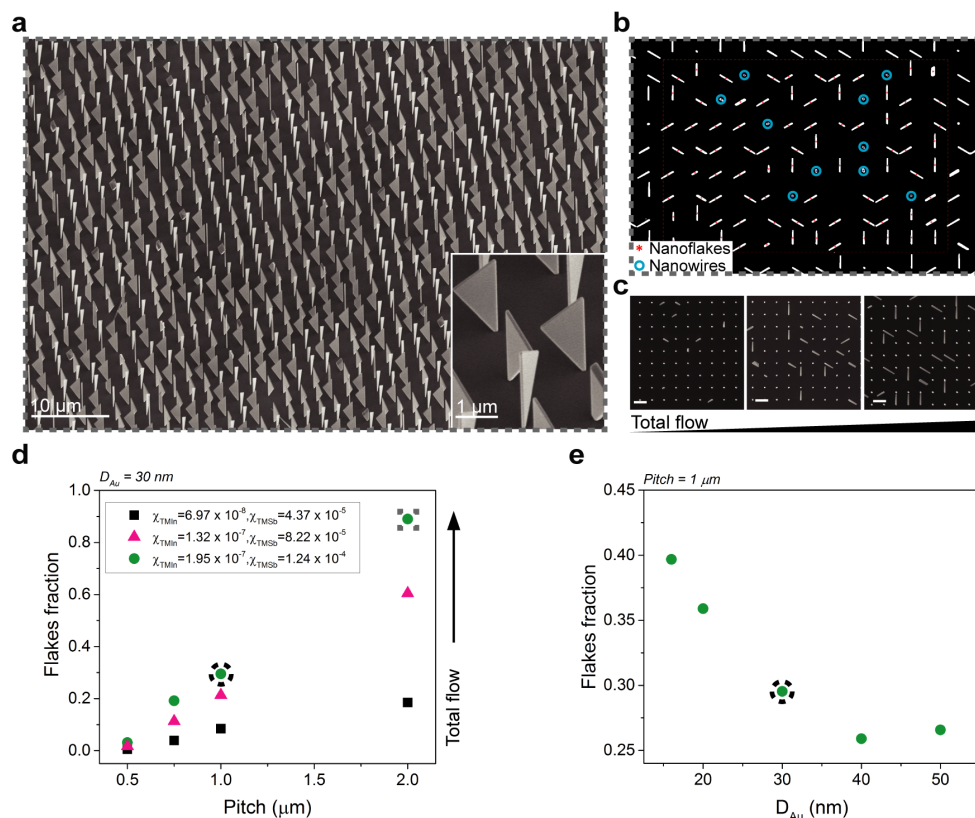
Figure 7.1 | Growth of InSb nanoflakes under high catalyst particle supersaturation. a, A 30°-tilted SEM image of InSb nanoflakes. Inset: magnified area shows the facetted morphology of the structures. **b**, Top view SEM image illustrating the image analysis script and flake counting method. Red asterisks and blue circles correspond to nanoflake and NW structures, respectively. **c**, Flake occurrence with increasing total gas flow of In and Sb species. The scale bar is 1 μm. **d**, Dependence of InSb nanoflake formation on pitch and total gas flow. (V/III ratio ~ 600 in all cases). Molar fractions are specified in the legend. The dashed square corresponds to images in panels **a** and **b**. **e**, Flake percentage as a function of the gold catalyst diameter (D_{Au}). For panels **d** and **e** the dashed circle indicates the same data point. For panels **a**-**d** the gold catalyst diameter is D_{Au} = 30 nm.

Finally, Figure 7.1e shows that the fraction of flakes decreases with increasing D_{Au}, which is in line with the above-mentioned hypothesis on the dependence of flake formation on supersaturation, since a smaller Au droplet will supersaturate faster.[18] We want to emphasize the implications of Figure 7.1d and Figure 7.1e: With the appropriate *in-situ* parameters (total precursor flow, substrate temperature), we can – within statistical uncertainty limits – locally choose whether nanoflakes and NWs are formed, simply by smart tailoring of the *ex-situ* parameters pitch and D_{Au}.

To study the relationship between the nanoflakes and the substrate, a top view SEM image is overlaid with a grid indicating the e-beam patterned Au particle positions in Figure 7.2a and Figure 7.2b. Three distinct InSb nanoflake orientations are visible, all belonging to the <112> family of directions with respect to the projection on the substrate. The angular distribution of the flakes is shown in the histogram in Figure 7.2c. Firstly, the data shows narrow peaks of equal height at 30, 150, and 270°, confirming epitaxial growth on the underlying (111)B substrate, having a three-fold symmetry. The fact that we find three orientations rather than six implies that no rotational twin boundaries are formed perpendicular to the axial [-111] growth direction, at or close to the substrate-nanoflake interface. Secondly, the frequency of the three orientations seems to be arbitrary. In other words, there is no clear preference for a specific orientation over the others. These observations demonstrate the epitaxial relation of the InSb nanoflakes to the growth substrate, and facilitate the design of more complex shadowing schemes, since the probability that a flake grows in the desired direction is 1/3 in the stemless approach. In contrast, because of the high density of twin defects in InP stems, we expect a six-fold symmetry in stem-based approaches, and consequently a statistical drop in device yield by a factor two. In addition, we obtain three-fold symmetric growth of InSb nanoflakes also on InP (111) B, (see Appendix Figure 7.7) showing the possibility to integrate InSb nanoflakes with other, insulating, III-V substrates.
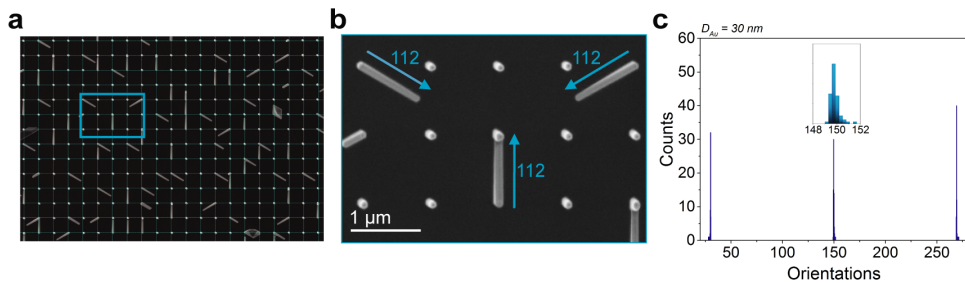
Figure 7.2 | Three-fold symmetry. a, Top view SEM image with an overlaid grid of the e-beam pattern. Blue rectangle magnified in **b**. Each flake has a <112> orientation in a direction indicated by an arrow demonstrating the epitaxial connection to the three-fold symmetric (111)B substrate. **c**, Count histogram of angular distributions. The inset magnifies the 150⁰ orientation. The histogram bin size is 0.3°. The gold catalyst diameter is D_{Au} = 30 nm and the pitch is 1 μm.

7.2.2 Nucleation point – structural analysis

Having demonstrated that our nanoflakes grow epitaxially, we now investigate the crystalline quality and the nucleation mechanism. Figure 7.3a shows a typical nanoflake, its side facets and the growth direction ([-111]). The HR-TEM images in Figure 7.3b and Figure 7.3c show that the nanoflakes are pure zinc-blende (ZB), in line with other low-dimensional InSb structures.[12,13,19] Importantly, a single twin boundary runs along the (11-1) facet, inclined with respect to the vertical [-111] growth axis (dashed line in Figure 7.3b and Figure 7.3c). This twinned section

persists along the entire length of that facet and is usually around 10 nm thick. A similar twin has been observed by de la Mata *et al.*[16] In that work, a mechanism is proposed in which this twin is formed close to the InAs stem/InSb flake interface and induces the formation of the flake. Even though the presence of the twin is confirmed by HR-TEM in our structures, the origin of the twin cannot be deduced from the nanoflake base in Figure 7.3b, since it is not known at which position the stemless flake is broken from the substrate. To clarify the nucleation mechanisms and the twin formation, we prepared a cross-sectional TEM lamella (see Appendix Subsection 7.4.3 for lamella preparation details).
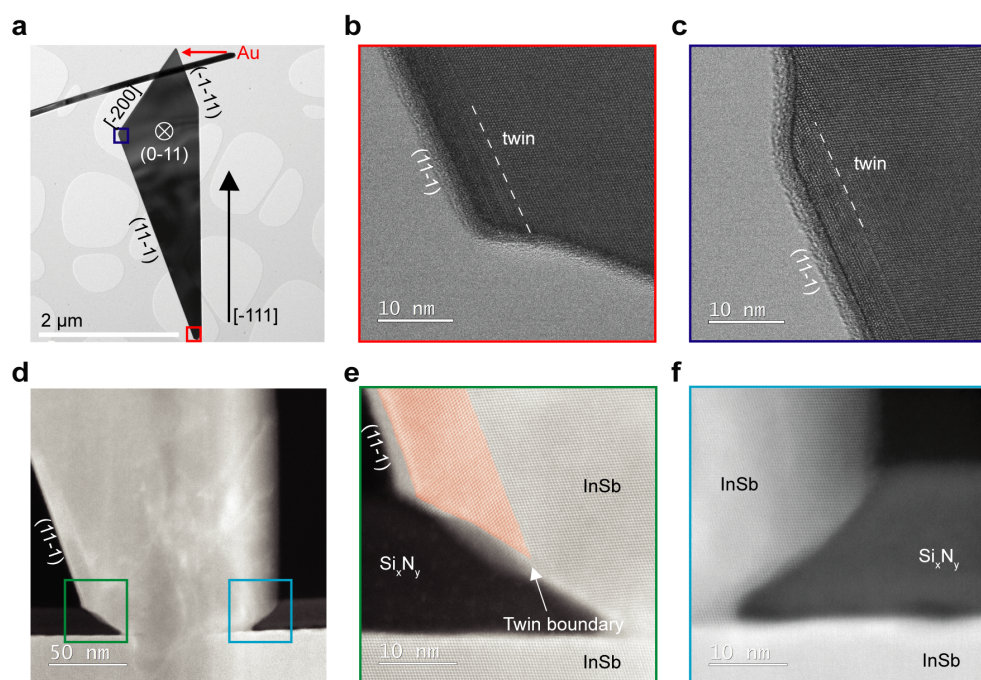
Figure 7.3 | Flake nucleation and twin formation. a, Low resolution TEM image of an InSb nanoflake. The growth direction is [-111] indicated by the black arrow. The large front and back facets correspond to {110} planes. The various facets are indicated. The red arrow indicates the position of the gold catalyst particle. (**b**) HR-TEM image of the InSb nanoflake near-base from panel **a**. The InSb phase is pure zincblende. A single twin boundary runs parallel to the (11-1) facet. **c**, HR-TEM image of the top of the (-111) facet where the twin boundary is present. The thickness of the twinned section is constant. **d**, Low resolution cross-sectional HAADF-STEM image of the InSb nanoflake base. **e**, HR-STEM image of the left side of the base showing a twin boundary starting nearby the substrate-flake interface and the edge of the Si_xN_y mask. The twinned section (pseudo-coloured red) is around 10 nm thick and borders the edge of the (11-1) facet. **f,** HR-STEM image of the right side of the base showing the pure zincblende phase of InSb and no presence of a twin boundary.

We focus on the base of the nanoflake, grown from the opening in the Si_xN_y mask. In total, we analysed 7 cross-sections (Appendix Figure 7.8 for additional cross-sectional lamella), with similar results as presented here: Figure 7.3d shows images of the both left and right bottom of the base, acquired by HR-STEM. The left side of

the base (Figure 7.3e) confirms the presence of the twin boundary along the (11-1) facet already within the Si_xN_y mask, developing in the first tens of nanometers of growth. The right side of the base in Figure 7.3f affirms a pure zinc blende crystal structure of the nanoflake without a twin.

It is well known for III-V NWs that both the supersaturation and the contact angle of the catalyst particle affect the formation of twin planes *perpendicular* to the NW growth direction,[20] and define which phase, wurtzite (WZ) or ZB, is most likely to nucleate.[21] Also, it has been observed for the growth of InSb NWs, that the increasing supersaturation in the Au/In/Sb particle drives the transition from ZB towards WZ in the growing wire.[22]

We think that at the early stages of the growth at the point where the highly supersaturated catalyst is in contact with the first few monolayers of precipitated InSb, the inclined twin is formed. The formation of the twin is a compensation for the high energy of the system due to the high supersaturation. Also, for the formation of this *inclined* defect, the contact angle of the catalyst particle at this point is considered essential. This contact angle is dependent on the supersaturation, which in turn is dependent on the total flow, the pitch and the primary catalyst diameter (D_{Au}), as evident from Figure 7.1.

7.2.3 Growth directions and morphology

To understand the growth mechanism of the flakes after nucleation of the twin and to be able to tune their final shape, we perform a time series, which allows us to monitor the evolution of different nanoflake morphologies. Figure 7.4a-c present the evolution of nanoflake morphologies with time. A distinctive nanoflake morphology is already observed after 15 min of growth (Figure 7.4a). Longer growth (Figure 7.4b and Figure 7.4c) results in nanoflakes with similar shape and aspect ratios. We propose a flake growth mechanism illustrated in Figure 7.4d. We argue that the growth of the nanoflakes results from nucleation at two growth fronts: 1) VLS growth in the [-111] direction via the Au catalyst particle and, 2) layer-by-layer growth in the [1-10] direction. The second process nucleates at a high energy point, in this case at the twin boundary, and is responsible for the lateral extension of the flake, leading to the formation of the (11-1) lower facet and the inclined (-200) top facet. The top-view schematic in Figure 7.4e indicates the side faceting of the nanoflake. Similar to InSb NWs, all side facets belong to the {110} family, with two extended (02-2) and (0-22) side facets as the front and the back of the nanoflake, respectively. The relative growth rates of the two growth fronts determine the size of the facets and the resulting flake morphology. Diverse nanoflake morphologies, observed in one field with constant D_{Au} and pitch, are shown in panels Figure 7.4f-i. Morphologies with the highest yield, observed when $D_{Au} > 30$ nm, are presented in Figure 7.4f and Figure 7.4g whereas morphologies in Figure 7.4h and Figure 7.4i, develop when $D_{Au} < 30$ nm. We propose that the nanoflake shape in Figure 7.4f corresponds to a growth regime where the VLS growth in [-111] direction is

dominating. The area between the two growth fronts is filled by forming {110} and {111} facets with low surface energy. The nanoflake shape observed in Figure 7.4g occurs when the relative growth rates of the two growth fronts are equal.
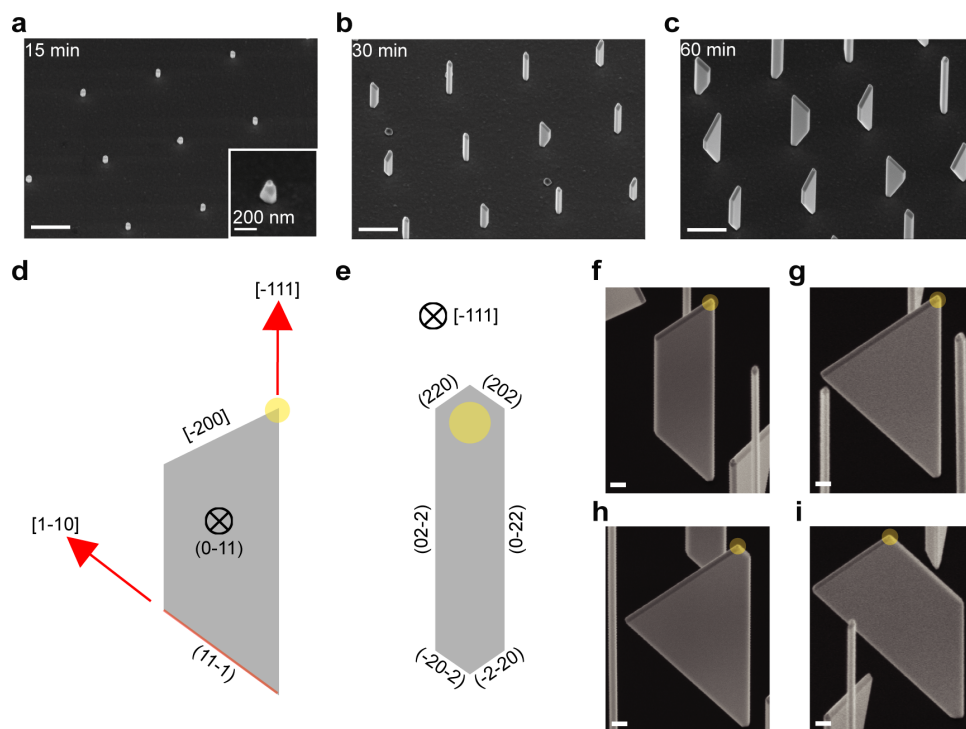
Figure 7.4 | Growth of flakes. a-c 30°-tilted SEM images of the evolution of InSb nanoflake morphologies with time. The molar fractions are χ_{TMIn} = 5.02 × 10^{-7}, χ_{TMSb} = 3.10 × 10^{-4}. The gold catalyst diameter is D_{Au} = 50 nm and the pitch is 2 μm. The scale bar is 1 μm. **d,** Schematic representation of the nanoflake growth mechanism. Growth of the flake occurs from two nucleation points indicated by red arrows, [-111] and [1-10]. The front and the back nanoflake facets are (0-11) and (01-1), respectively. **e,** Schematic illustration of a top view of a nanoflake. The [-111] is pointing upwards. **f-i** Diverse nanoflake morphologies sharing similar facet families. The growth time was 6 hours. The molar fractions are χ_{TMIn} = 1.32 × 10^{-7}, χ_{TMSb} = 1.23 × 10^{-4}. The gold catalyst diameter is D_{Au} = 30 nm and the pitch is 2 μm. Scale bars are 200 nm. The Au particle is indicated by a transparent yellow dot.

Shapes observed in Figure 7.4h and Figure 7.4i can be explained by the rapid formation of the top (-1-11) facet. The Au particle can wet this additional plane of the nanoflake, and thereby change the particle contact angle[19]. As a consequence, a (-1-11) facet is formed at the right side of the catalyst particle. Starting with a morphology similar to the one in Figure 7.4g, Au wetting of the additional top facets terminated with the edge pointing upwards [-200] direction leads to a development of the morphology in Figure 7.4h. Further evolution of that morphology can be recognized in Figure 7.4i, with a pronounced (-1-11) facet. It is important to mention that these additional facets form without the introduction of another twin, as verified with HR-TEM (see Appendix Figure 7.9). The nanoflake dimensions can

thus be tuned by the growth time, which determines the size (Appendix Figure 7.10), and the relative growth rates, which determine the shape. The nanoflake thickness increases with the gold particle size. The minimum thickness of nanoflakes observed in this study was ~ 60 nm, for a D_{Au} = 16 nm (Appendix Figure 7.11), lower than the value of the Bohr radius. This allows the growth of very large InSb "free-standing" systems as a platform for functional bottom-up 2D devices to study topological quantum phenomena.

To verify the growth mechanism discussed in Figure 7.3 and Figure 7.4, we investigated the growth of nanoflakes for an order of magnitude higher total gas flow for both precursors. Figure 7.5 shows nanostructures resulting from these conditions. In contrast to the low-flow conditions, we notice parasitic island growth on the Si_xN_y, which we believe to be primarily In droplets. Consequently, the growth conditions studied here are equivalent to an extremely high Au particle supersaturation regime.

7
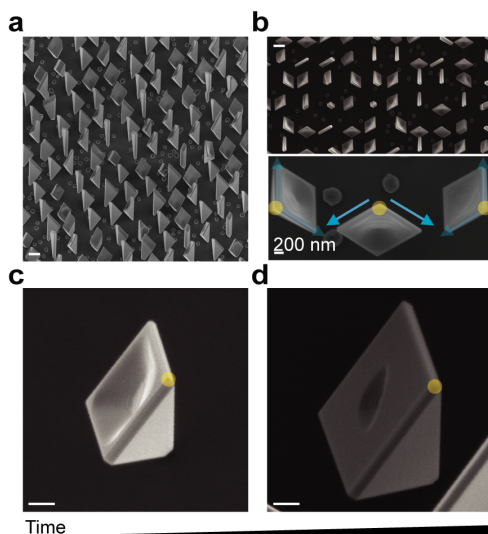
Figure 7.5 | Double-twinned structures. a, A 30°-tilted SEM image of InSb double-twinned structures. **b**, Top view SEM images with different magnifications. <112> directions are indicated by blue arrows. Scale bars for (a-b) are 1 μm. **c-d**, Evolution of double-twin structures with time. The molar fractions are χ_{TMIn} = 1.95 × 10^{-7}, χ_{TMSb} = 1.23 × 10^{-4}. The growth time is 3 and 12 hours, respectively. The Au particle in **b-d** is indicated by a yellow dot. The gold catalyst diameter is D_{Au} = 30 nm and the pitch is 2 μm. Scale bars for **c** and **d** are 200 nm.

The top view SEM image in Figure 7.5b demonstrates the same three-fold growth symmetry as observed for nanoflakes. Compared to the nanoflakes, the nanostructures observed here each exhibit lateral extension in two out of the three distinct <112> orientations discussed in Figure 2. These peculiar structures most likely are formed by two separate inclined twin boundaries. The time series study in this growth regime reveals a favourable [1-10] growth direction that nucleates at two

high energy points, in this case at two twin boundaries, resulting in the formation of the given shape. To form the base of the double-twinned structure, an additional fourth facet was formed during the growth. The concave shape of the additional facet is reduced with time by a filling process based on the reduction of the total surface energy as shown in Figure 7.5c and Figure 7.5d for 3- and 12-hours growth, respectively.

7.2.4 Quantum Hall effect

The quantum Hall effects is an effect that occurs in 2DEGs cooled to low temperatures and placed in a high magnetic field.[23] In this regime the transport occurs due to edge states. If a current in the longitudinal direction of a rectangular sample is fixed, the electrons will start moving a Lorentz force will deflects them in the perpendicular directions. This creates an electric force in the perpendicular direction. If we measure the voltages in both directions of a perpendicular sample, we will get an information on the resistance. The perpendicular resistance is called "Hall resistance" (R_{XY}) and in the quantum regime it shows as a number of plateaus as a function of magnetic field. The longitudinal resistance (R_{XX}) appears as peaks of the resistance at the transition between plateaus.

We perform low-temperature (4 K) magnetoresistance measurements on a Hall-bar device to study the electronic material properties of our nanoflakes. The device is shown in the Figure 7.6a. A nanoflake is deposited on a p-Si/SiO$_x$ substrate, which serves as a backgate. The flake thickness is ~80 nm, the active area within the voltage probes is 1 μm wide and 0.7 μm long. The classical Hall effect is used to obtain the carrier density (n) and mobility (μ) as function of bottom gate voltage (V_{BG}), as presented in Figure 7.6a. The carrier density is extracted from the linear fit of the longitudinal resistance (R_{XY}) for the magnetic field (B) ranging from -1 T to 1 T (inset of the Figure 7.6c). A mobility of around 20 000 cm^2/Vs is measured for an electron density of 1.9 x 10^{12} cm^{-2}, which is the highest mobility reported for InSb bottom-up nanoflakes to our knowledge. The mobility is comparable to the highest reported low-temperature mobilities found in InSb NWs[2] and is an order of magnitude lower than that of a quantum well structure[7,9], which is most likely due to the absence of any protective barrier layer. For increased bottom gate voltages the mobility decreases slightly, which might be due to the population of higher sub-bands[9]. At larger magnetic fields quantum Hall plateaus emerge, as seen in the Landau-level fanchart shown in Figure 7.6c.
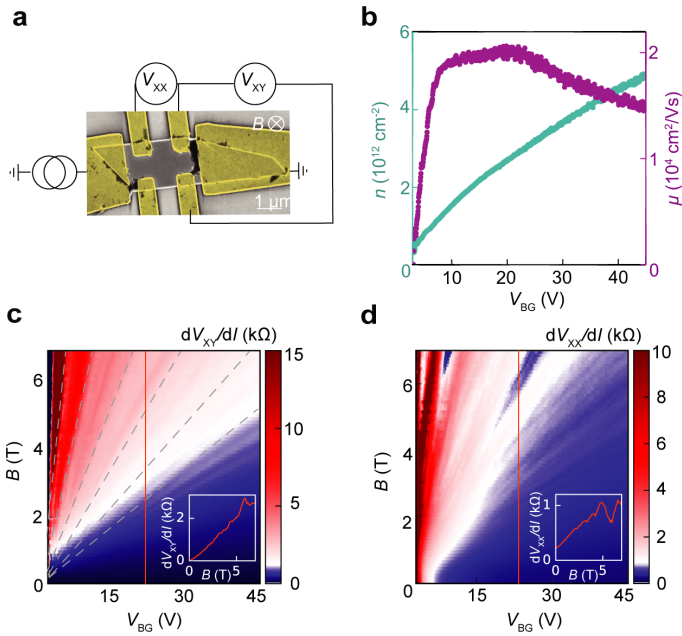
Figure 7.6 | **Quantum Hall measurements. a**, A SEM image of the measured Hall bar device with illustration of the four terminal current bias measurement setup. **b**, Hall electron density (n) and mobility (μ) as a function of global bottom gate voltage (V_{BG}). **c**, Differential resistance transverse to the current direction R_{XY} as a function of magnetic field (B) and V_{BG}. The resistance plateaus are indicated with the grey dashed lines. **d**, Differential resistance along the current direction R_{XX} as a function of magnetic field (B) and V_{BG}. Linecuts in the inset of panels **c** and **d** are taken at V_{BG} = 22.5 V. All measurements are performed at a temperature of 4 K.

Even though we can clearly spectrally resolve the two-dimensional subbands, the conductance plateaus do not reach quantized values. This is due to the non-ideal Hall-geometry of our device (the width of the voltage probes is larger than their separation) which gives rise to an intermixing of Hall- and longitudinal resistances (Figure 7.6d). Nonetheless, if one were to replace the current and voltage terminals in our poor Hall device by superconducting contacts, one would readily arrive close to an ideal device for topological multi-terminal Josephson experiments[24], since the mean-free path in our device (0.45 µm) is in the same range as the contact separation.

7.3 Conclusions

In conclusion, we have presented a method to grow high quality "free-standing" 2D InSb nanoflakes. We have demonstrated that the growth of a nanoflake is connected to the formation of an inclined twin at its base. To trigger this twin formation, a high droplet supersaturation is crucial. Since the magnitude of supersaturation depends on both *in-situ* and ex-situ growth parameters, we can tweak the likeliness of nanoflake formation by smart template design. The flakes show three-fold symmetric growth due to an epitaxial relationship with the substrate. Signatures of quantum Hall plateaus – the fingerprint of confinement-driven 2D subband formation – are clearly seen in a back-gated six-terminal Hall-bar device. The carrier mobility corresponds to mean-free paths in the same range as the contact separation, setting our device on the edge of a fully ballistic multi-terminal junction. We foresee that our structures have the potential to be used as "free-standing" devices with metal contacts deposited *in-situ* from both sides of the structures with our smart-shadowing technique (see Appendix Subsection 7.4.6). Such devices can be used to study *e.g.*, new quantum phenomena or phonon confinement for thermal rectifiers[25]. Next step is to design substrates and grow envisioned structures.

7.4 Appendix

7.4.1 Substrate fabrication recipe

InSb(111)B substrates prepatterned using e-beam lithography were used for the growth of InSb nanoflakes and NWs.

Processing steps are listed:
- Plasma-enhanced chemical vapor deposition (PECVD) of 20 nm Si_xN_y mask (300 °C, Oxford Instruments Plasmalab System 100);
- Spin coat the wafer with primer AR 300-80 at 4000 rpm for 60 seconds, bake at 180 °C for 2 minutes;
- Spin coat the wafer with resist AR-P 6200.04 at 4000 rpm for 60 seconds, bake at 150 °C for 3 minutes;
- Write dot patterns using e-beam lithography varying the dot size (10 – 50 nm) and pitch (0.25 – 4 μm) (dose 1650 – 2750 μC/cm^2)
- Developing in AR 600-546 for 60 seconds, stopper AR 600-60 for 30 seconds, rinse IPA for 60 seconds;
- Opening the holes in Si_xN_y mask with buffered oxide etch (NH$_4$F:HF = 7:1) for 14 – 16 seconds;
- Rinse with H_2O;
- Evaporation of 8 nm Au with an evaporation rate of 1 Å/s (Electron-beam evaporator);
- Lift-off in PRS3000 at RT for 1 hour, ultrasonic agitation in acetone for 10 minutes, rinse in IPA for 10 minutes;
- Organic residues removal by O_2 plasma (10 minutes, 55 sccm O_2, 300 W plasma power).

7.4.2 MOVPE growth of nanoflakes

For the growth of InSb nanoflakes and NWs a horizontal Aixtron 200 metal-organic vapor phase epitaxy (MOVPE) reactor with infrared lamp heating was used. InSb nanoflakes and NWs were grown at 495°C using *trimethyl*-indium (TMIn) and *trimethyl*-antimony (TMSb) with precursor molar fractions ranging from:
χ_{TMIn} = 7.0 x 10^{-8} to 1.95 x 10^{-6}, and χ_{TMSb} = 4.4 x 10^{-5} to 1.2 x 10^{-3}. Growth times were varied from 15 minutes to 12 hours. During growth the reactor pressure was 50 mbar, total flow 6000 sccm and H_2 was used as a carrier gas.

7.4.3 Focused Ion Beam TEM lamella preparation

TEM lamellas are prepared in a FEI Nova Nanolab 600i. Initially the bottoms of selected nanoflakes were embedded using an electron-beam induced TEOS (Tetraethyl orthosilicate) deposition in order to minimize the ion beam damage in the following truncation step. Next, the tops of the flakes are truncated using Ga ion beam in order to limit the size of the nanoflake to a few hundred nanometer and simplify the following lift-out and thinning procedures. The truncated nanoflakes are then further embedded by electron-beam induced Platinum and ion-beam induced Platinum depositions. The Platinum is used as a sacrificial layer for the thinning procedure. A TEM lamella is cut from the truncated nanoflakes and transferred to a half-moon TEM grid for thinning. Finally, thin windows are cut into the lamella using Ga in beam milling steps at 30 kV, 16 kV and finally 5 kV to create

7

windows with a thickness of less than 100 nm and minimize damage induced by the ion beam.

7.4.4 Quantum Hall device fabrication and measurement

InSb thin nanoflake (~80 nm) is contacted by Au/Cr.

Device fabrication recipe:
1. Transfer InSb nanoflakes using nanomanipulator onto a p-doped Si substrate covered by 285 nm SiO_2 layer, serving as a back-gate dielectric.
2. E-beam lithography: resist + bake + write designed contacts + resist development
3. Wet etch with saturated ammonium-sulphide solution[26]
4. Gentle He-ion milling[27]
5. Evaporate normal contact Au/Cr (150 nm/10 nm).
6. Lift off in acetone.

The sample is evacuated for 5 days before cooling down, in order to desorb water residues from the flake surface[2]. The measurements are performed in a Janis cryostat at the liquid Helium temperature of 4 K.

7.4.5 Growth and additional analysis of InSb nanoflakes
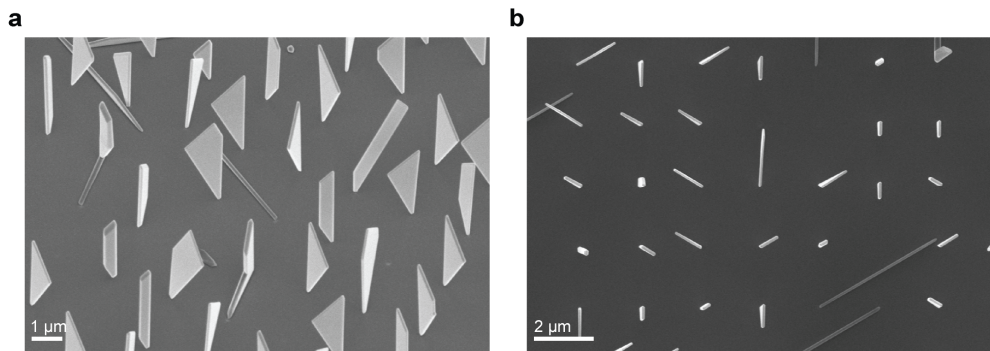
Figure 7.7 | Three-fold symmetric growth of InSb nanoflakes on InP (111)B substrate. **a**, A 30°-tilted SEM image of InSb nanoflakes grown on an InP (111)B substrate. Morphologies comparable to the ones discussed in the main text can be recognized. **b**, Top view SEM image showing three distinct projected in-plane <112> orientations of nanoflakes suggesting the three-fold crystal symmetry with the substrate.
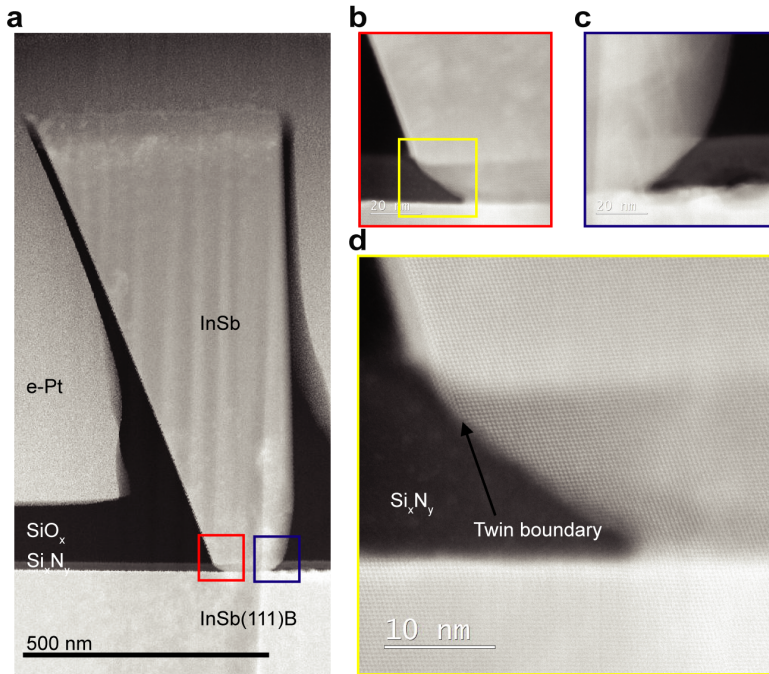
Figure 7.8 | **Additional cross-sectional TEM analysis. a**, Low resolution cross-sectional HAADF-STEM image of an InSb nanoflake embedded in SiO_x/e-Pt/i-Pt, required prior to focused ion beam (FIB) milling. The red and blue (left and right) rectangles indicate the HR-STEM analysis regions of the nanoflake base, **b**, and **c**, respectively. **d**, Magnified region from panel **b** showing a twin boundary present nearby the substrate-flake interface and the edge of the Si_xN_y mask. The twinned section is around 3 nm thick and heavily oxidized due to the SiO_x evaporation prior to FIB lamella preparation. The twin is situated on the edge of the (11-1) facet.
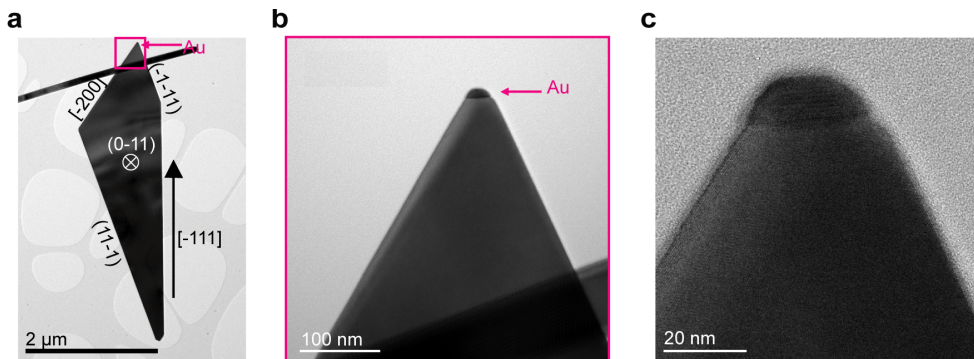
Figure 7.9 | **TEM analysis of the nanoflake morphology similar to the Figure 7.4h-i. a**, Low resolution TEM image of an InSb nanoflake on the holey carbon film. The growth direction is [-111]. The large front and back facets of the flake correspond to the (0-11) and (01-1) planes, respectively. The various facets are indicated. The arrow (pink) indicates the position of the gold catalyst particle. **b**, HR-TEM image of the InSb nanoflake top from the magnified area indicated by a rectangle (pink) in panel **a**. **c**, InSb shows the pure zincblende phase and no presence of a twinned section along the top (-1-11) facet.
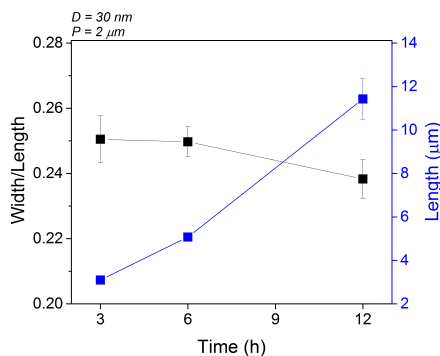
Figure 7.10 | **Time series.** Evolution of InSb nanoflakes width/length (black data points) and length (blue data points) with growth time. Molar fractions for samples grown for 3 and 6 hours are: $\chi_{TMIn} = 1.32 \times 10^{-7}$, $\chi_{TMSb} = 1.23 \times 10^{-4}$ (parameters corresponding to data points from Figure 4 (e-j), V-III ~ 930). Molar fractions for the sample grown for 12 hours are: $\chi_{TMIn} = 1.95 \times 10^{-7}$, $\chi_{TMSb} = 1.24 \times 10^{-4}$ (parameters corresponding to green circular data points from Figure 7.1d, V-III ~ 630). The gold catalyst diameter is $D_{Au} = 30$ nm and the pitch is 2 μm.
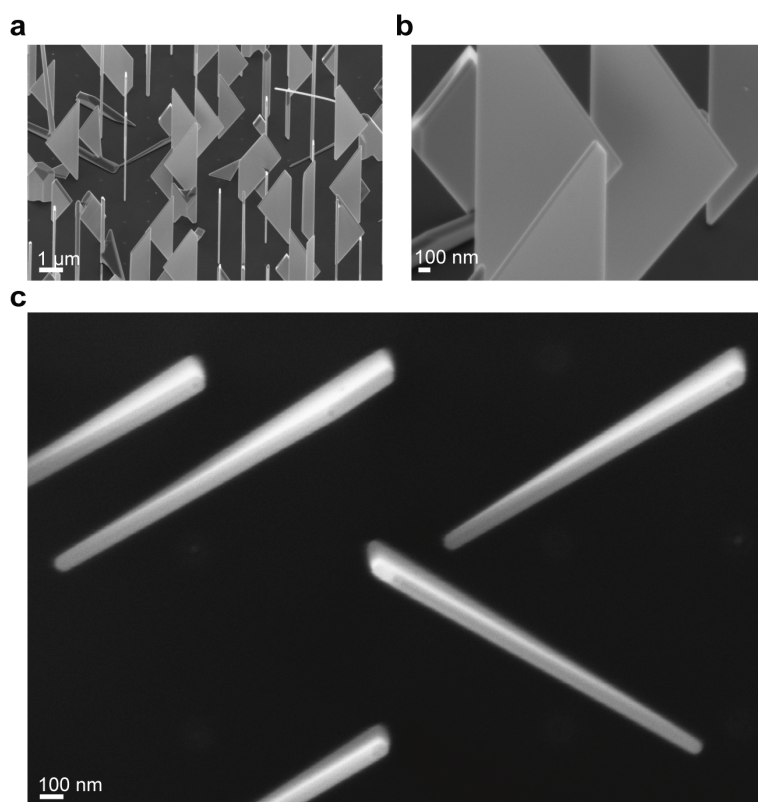
Figure 7.11 | **Thin InSb nanoflakes. a-b** A 30°-tilted SEM image of InSb nanoflakes. The rotation angle of the sample in the SEM was aligned with one of the in-plane <112> orientations of the nanoflakes. Nanoflakes appear as large and thin "free-standing" objects. **c**, Top view SEM image displaying thin nanoflakes, with a measured thickness of ~60 nm. The gold catalyst diameter is $D_{Au} = 16$ nm and the pitch is 1 μm.

7.4.6 Smartly designed shadowing structures

In this section, we show how our site-controlled nanoflake/NW growth process can be used to design novel nanoscale all *in-situ* quantum devices by using our smart shadowing technique[14]. We envision two distinct approaches where the nanoflake is either a) the active device object (Figure 7.12), or b) the shadowing object to define a junction on a NW (Figure 7.14). Approach a) results in *in-situ* Josephson junctions on the nanoflake, with the junction width determined by the diameter of the shadowing NW. Approach b) can be used to manufacture *in-situ* Josephson junctions on NWs. This method is similar to our NW-NW self-shadowing method reported in Chapter 5,[14] with two advantages: One, the substrate fabrication is much easier, since no trenches have to be cut into the substrate, and the alignment of the catalyst into the trenches becomes obsolete. Two, since the width of the junction depends on the position of the flake in the shadowing path, devices with different width can be grown in the same run. This allows for *e.g.*, a detailed study of the length scale superconducting coupling in InSb NWs. An estimate of the probability for a successful device formation can be found in the Table 7.1 and Table 7.2 for approach a) and b), respectively. For additional clarification of the approach, SEM images in Figure 7.13 and Figure 7.15 are added.
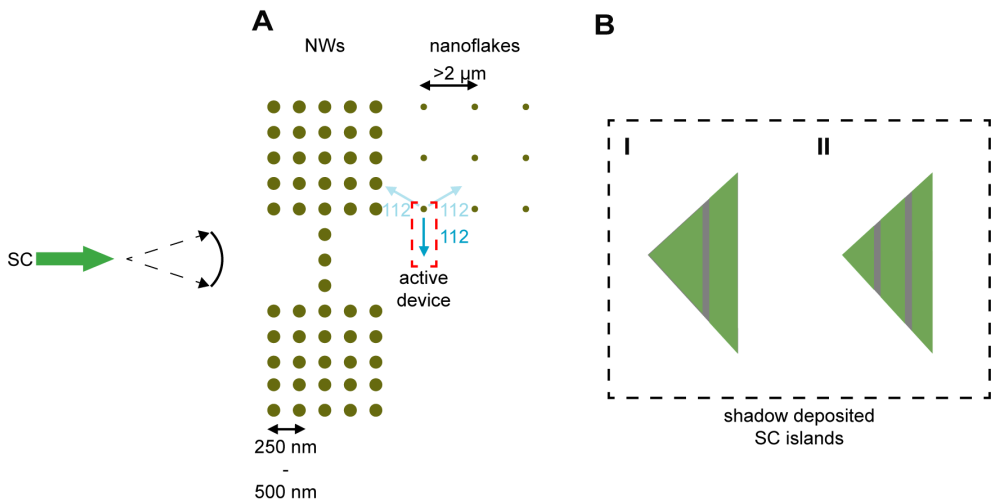
Figure 7.12 | Shadowed nanoflake. The flux source of a metal (SC) in ultra-high vacuum originates from the left to right (green arrow). **A,** Sketch of the field with grown NWs and nanoflakes where a nanoflake (encircled with a red dashed line) acts as the active device. The field with NWs is patterned with D_{Au} = 50 nm and pitch around 250 – 500 nm. The field for nanoflakes is patterned with D_{Au} = 30 nm and pitch greater than 2 µm (see data in the main text Figure 7.1d). The nanoflake can have three possible <112> orientations. Only one orientation can be an active device (encircled with a red dashed line). **B,** I and II: Sketch of the possible scenario for the active nanoflake device. Device I has been shadowed by one NW. Device II has been shadowed by two NWs.

Table 7.1 | **Probability calculation for "shadowed nanoflake" device.**

Probability NW growth P_{NW}	Probability flake growth (Figure 7.1d D_{Au}=30 nm, pitch 2 µm) P_{flake}	Probability flake angle P_{angle}	Total probability $P = P_{NW}$ x P_{flake} x P_{angle}	In 100 devices P_{100}
1	0.89	1/3	0.29	29
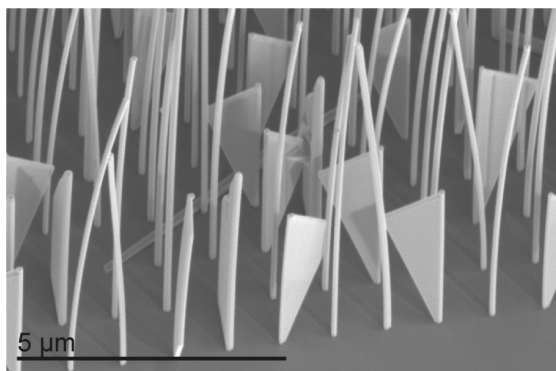
Figure 7.13 | **Shadow-deposited superconducting aluminum contacts on InSb nanoflakes.** A 30°-tilted SEM image of a field with InSb nanoflakes with ~10 nm superconducting aluminium deposited using molecular beam epitaxy (MBE) machine. NWs and nanoflakes act as shadow objects. Shadow and aluminium regions on nanoflakes can be clearly distinguished.
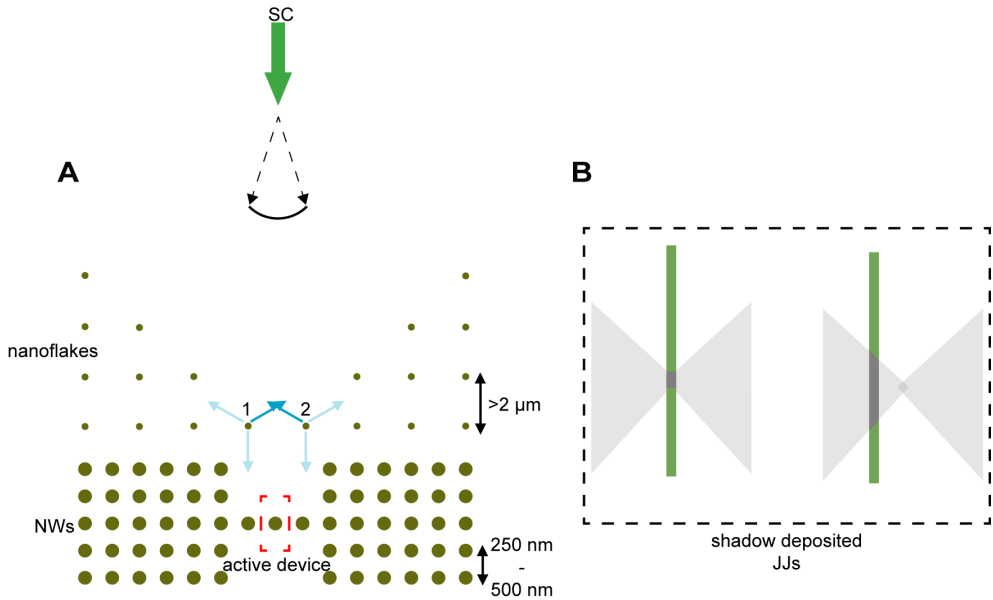
Figure 7.14 | Shadowed nanowire. The flux source of a metal (SC) in ultra-high vacuum originates from top towards the active device (green arrow). (A) Sketch of the field with grown NWs and nanoflakes where NW (encircled with a red dashed line) acts as the active device. The field with NWs is patterned with D_{Au} = 50 nm and pitch around 250 – 500 nm. The field for nanoflakes is patterned with D_{Au} = 30 nm and pitch greater than 2 μm (see data in the main text Fig. 1d). Nanoflakes 1 and 2 can have three possible <112> orientations. There are three positive scenarios to realize the active device: both 1 and 2 are nanoflakes, or either 1 or 2 is a nanoflake. (B) Sketch of the possible scenarios for the active Josephson Junctions (JJs) NW device depending on the incoming angle of the SC.

Table 7.2 | Probability calculation for "shadowed nanowire" device.

Probability NW growth P_{NW}	1	1	1
Probability flake 1 growth ~ (Figure 7.1d D_{Au}=30 nm, pitch 2 μm) P_{flake1}	0.89	0.89	
Probability flake angle P_{angle1}	1/3	1/3	
Probability flake 1 growth ~ (Figure 7.1d D_{Au}=30 nm, pitch 2 μm) P_{flake2}	0.89		0.89
Probability flake angle P_{angle2}	1/3		1/3
Total probability $P = P_{NW} \times P_{flake\ 1\ and/or\ 2} \times P_{angle\ 1\ and/or\ 2}$		2 x 0.29	2 x 0.29
In 100 devices P_{100}	8	58	58

7

117
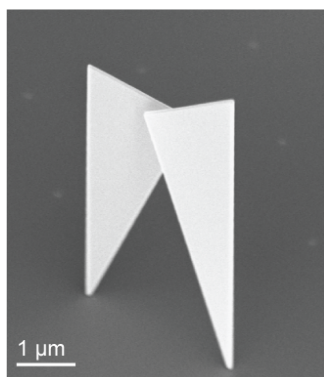
Figure 7.15 Greeting nanoflakes. A 30°-tilted SEM image of a two InSb nanoflakes facing towards each other while growing in two different <112> direction demonstrating feasibility of suggested approach b) for *in-situ* device fabrication.

7.5 References

1   van Weperen, I. *et al.* Spin-orbit interaction in InSb nanowires. *Physical Review B* **91**, 201413 (2015).

2   Gül, Ö. *et al.* Towards high mobility InSb nanowire devices. *Nanotechnology* **26**, 215202 (2015).

3   Mourik, V. *et al.* Signatures of Majorana Fermions in Hybrid Superconductor-Semiconductor Nanowire Devices. *Science* **336**, 1003-1007, doi:10.1126/science.1222360 (2012).

4   Zhang, H. *et al.* Quantized Majorana conductance. *Nature* **556**, 74, doi:10.1038/nature26142 (2018).

5   Deng, M. T. *et al.* Anomalous Zero-Bias Conductance Peak in a Nb–InSb Nanowire–Nb Hybrid Device. *Nano Letters* **12**, 6414-6419, doi:10.1021/nl303758w (2012).

6   Goldammer, K. J. *et al.* High-mobility electron systems in remotely-doped InSb quantum wells. *Journal of Crystal Growth* **201-202**, 753-756, doi:10.1016/S0022-0248(98)01526-7 (1999).

7   Lehner, C. A. *et al.* Limiting scattering processes in high-mobility InSb quantum wells grown on GaSb buffer systems. *Physical Review Materials* **2**, 054601, doi:10.1103/PhysRevMaterials.2.054601 (2018).

8   Orr, J. M. S. *et al.* Electronic transport in modulation-doped InSb quantum well heterostructures. *Physical Review B* **77**, 165334 (2008).

9   Yi, W. *et al.* Gate-tunable high mobility remote-doped InSb/In1−xAlxSb quantum well heterostructures. *Applied Physics Letters* **106**, 142103, doi:10.1063/1.4917027 (2015).

10   Goel, N. *et al.* Ballistic transport in InSb mesoscopic structures. *Physica E: Low-dimensional Systems and Nanostructures* **26**, 455-459, doi:10.1016/j.physe.2004.08.080 (2005).

11   Plissard, S. R. *et al.* From InSb Nanowires to Nanocubes: Looking for the Sweet Spot. *Nano Letters* **12**, 1794-1798, doi:10.1021/nl203846g (2012).

12   Caroff, P. *et al.* High-Quality InAs/InSb Nanowire Heterostructures Grown by Metal–Organic Vapor-Phase Epitaxy. *Small* **4**, 878-882, doi:10.1002/smll.200700892 (2008).

13   Caroff, P. *et al.* InSb heterostructure nanowires: MOVPE growth under extreme lattice mismatch. *Nanotechnology* **20**, 495606 (2009).

14   Gazibegovic, S. *et al.* Epitaxy of advanced nanowire quantum devices. *Nature* **548**, 434, doi:10.1038/nature23468 (2017).

15   Thelander, C., Caroff, P., Plissard, S. & Dick, K. A. Electrical properties of InAs1−xSbx and InSb nanowires grown by molecular beam epitaxy. *Applied Physics Letters* **100**, 232105, doi:10.1063/1.4726037 (2012).

16   de la Mata, M. *et al.* Twin-Induced InSb Nanosails: A Convenient High Mobility Quantum System. *Nano Letters* **16**, 825-833, doi:10.1021/acs.nanolett.5b05125 (2016).

17   Pan, D. *et al.* Free-Standing Two-Dimensional Single-Crystalline InSb Nanosheets. *Nano Letters* **16**, 834-841, doi:10.1021/acs.nanolett.5b04845 (2016).

18   Dubrovskii, V. G., Sibirev, N. V., Harmand, J. C. & Glas, F. Growth kinetics and crystal structure of semiconductor nanowires. *Physical Review B* **78**, 235301, doi:10.1103/PhysRevB.78.235301 (2008).

19   Plissard, S. R. *et al.* Formation and electronic properties of InSb nanocrosses. *Nature Nanotechnology* **8**, 859, doi:10.1038/nnano.2013.198 (2013).

20   Johansson, J. *et al.* Effects of Supersaturation on the Crystal Structure of Gold Seeded III−V Nanowires. *Crystal Growth & Design* **9**, 766-773, doi:10.1021/cg800270q (2009).

21   Jacobsson, D. *et al.* Interface dynamics and crystal phase switching in GaAs nanowires. *Nature* **531**, 317, doi:10.1038/nature17148 (2016).

22   Bernhard, M. *et al.* Crystal structure control in Au-free self-seeded InSb wire growth. *Nanotechnology* **22**, 145603 (2011).

23   Klitzing, K. v., Dorda, G. & Pepper, M. New Method for High-Accuracy Determination of the Fine-Structure Constant Based on Quantized Hall Resistance. *Physical Review Letters* **45**, 494-497, doi:10.1103/PhysRevLett.45.494 (1980).

24   Riwar, R.-P., Houzet, M., Meyer, J. S. & Nazarov, Y. V. Multi-terminal Josephson junctions as topological matter. *Nature Communications* **7**, 11167, doi:10.1038/ncomms11167 (2016).

25   Wang, Y. *et al.* Phonon Lateral Confinement Enables Thermal Rectification in Asymmetric Single-Material Nanostructures. *Nano Letters* **14**, 592-596, doi:10.1021/nl403773f (2014).

26   Suyatin, D. B., Thelander, C., Björk, M. T., Maximov, I. & Samuelson, L. Sulfur passivation for ohmic contact formation to InAs nanowires. *Nanotechnology* **18**, 105307 (2007).

27   Gül, Ö. *et al.* Hard Superconducting Gap in InSb Nanowires. *Nano Letters* **17**, 2690-2696, doi:10.1021/acs.nanolett.7b00540 (2017).

7
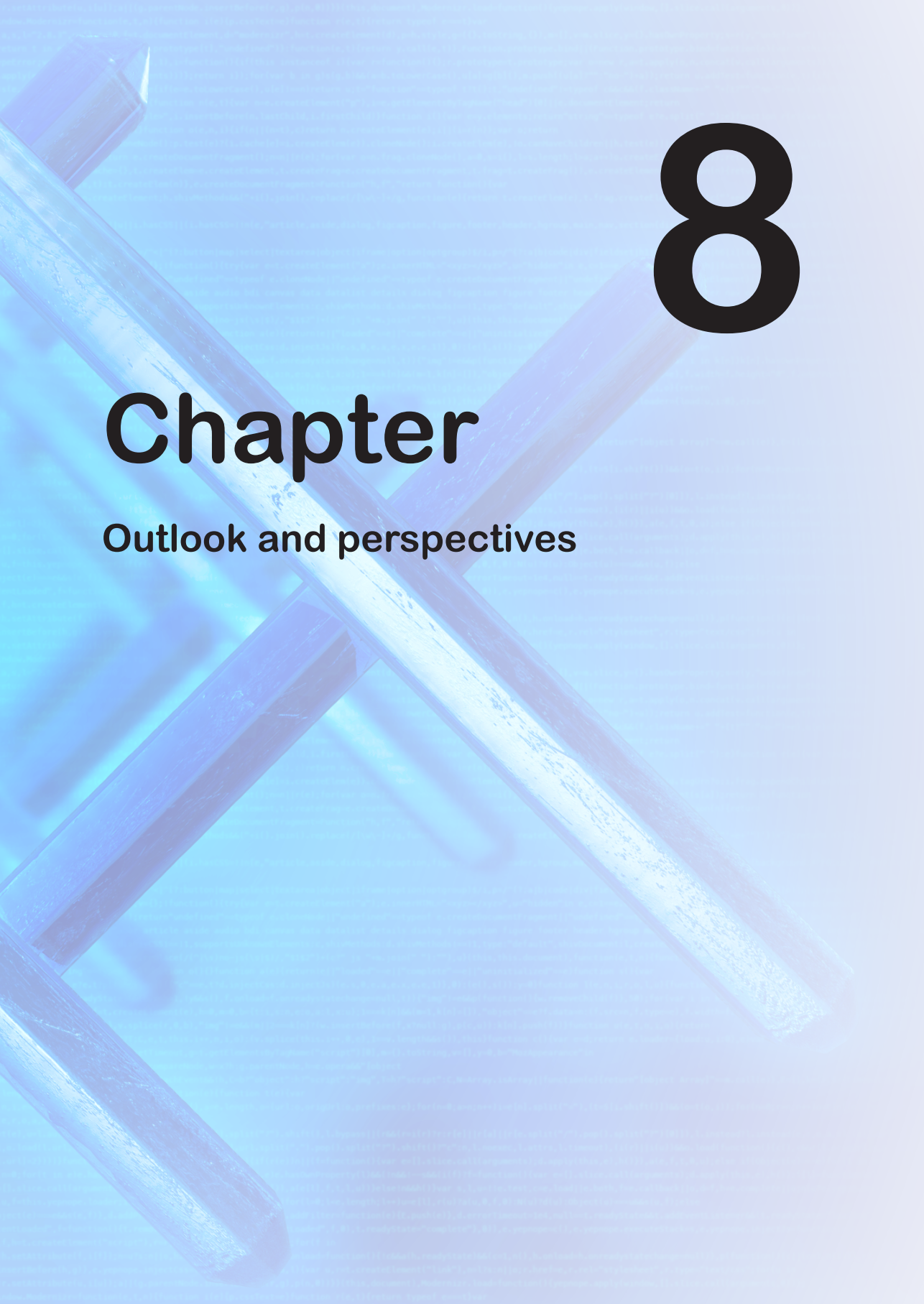
8

Chapter

Outlook and perspectives

Abstract This chapter briefly concludes and reflects on achieved and future pathways of the work studied in this thesis. This chapter is not detailed, it rather focuses on my vision towards future directions of the subject matter of this research, pragmatic development of quantum materials and topological quantum devices.

8.1 Conclusion

In the experimental chapters of this thesis, we have shown that by finely designing the substrate and tuning the growth parameters the bottom-up growth of high-quality InSb low-dimensional nanostructures (quantum nanowires and nanoflakes) is achieved. Growth of InSb material was continuously crafted and perfected to accommodate the quasiparticles that are the foundation for a universal topological quantum computer. We developed the growth of complete quantum devices by combining two epitaxy worlds; MOVPE for the growth of various InSb nanostructures, and MBE for the growth of superconducting Al contacts.

8.2 Perspectives of the research

Despite the fascinating progress of material properties using bottom-up grown nanowires two main challenges of this research still remain to be solved: decoherence caused by dissipation of Majoranas in the system and scalability of the system.

8.2.1 Choice of the material

Naturally, the next step is to realize reproducible Majorana devices. This still remains a major challenge, as hypothesized dissipation channels are likely to formed in current devices. Dissipation in Majorana NbTiN-InSb-based devices may potentially arise from the disorder in the material system.[1] Albeit the growth of Al on InSb is successfully realized, post-growth fabrication poses a great dispute as Al-InSb interface reactions occur at temperatures lower than the standard device processing temperatures (see Chapter 5). Interface reactions create a wide band gap AlInSb alloy layer that could lead to detrimental effects for Majorana devices. In addition, the large lattice mismatch between InSb ($a_{InSb} = 6.479 \text{ Å}$) and Al ($a_{Al} = 4.051 \text{ Å}$) could create strain at the interface contributing to disorder. The large lattice parameter of InSb makes it incompatible with many superconductor materials attractive for the application in Majorana devices (Pb, In, V, *etc.*). Superconducting Sn is an interesting candidate for InSb with matching lattice parameters, however the challenge is the rapid oxidation of Sn films. To prevent from oxidation a capping layer must be used. This could create a challenge for *in-situ* material growth as a suitable capping layer demands an additional growth step. Essentially, the material interfaces need to be improved for realizing more robust and reproducible Majorana devices.

Another very interesting material with outstanding properties matching the requirements for topological quantum computation is PbTe. Bulk PbTe has high carrier mobilities (~10^6 cm^2/Vs) at liquid He temperatures,[2] strong spin-orbit interaction and a large Landé g-factor (≈ 60).[3] From the limited number of existing growth reports it has been demonstrated that one-dimensional PbTe structures crystallize in the zincblende structure and the preferential growth direction is <001> with <100> side facets.[4-8] Here, we propose the growth of a new material system for ultimate Majorana devices made of PbTe quantum nanowire proximitized with superconducting Pb. The critical temperature (T_C) and critical magnetic field (B_C) of Pb is expected to be 7.2 K and 80 mT, respectively. When combined, a sharp interface is expected to be shared between the two materials creating an ideal candidate for a Majorana device. Our MBE cluster tool should be able to *in-situ* grow materials of high purity.

Group IV materials (Ge, Si, Ge-Si), most heavily investigated materials, also have a potential for application in topological quantum computer. Qubits made from these materials should show extremely long spin coherence times due to the absence of nuclear spin for even-number isotopes of Ge and Si.[9] The predicted strong Rashba spin-orbit coupling of these materials tunable by electric fields and induced lattice strain matches the requirement set for Majorana experiments.[10] Challenge is a relatively small, however gate-tunable, g-factor.[11,12] The growth of high quality core-shell Ge-Si nanowires is performed in our group using a MOVPE reactor.[13] The next goal for the growth in our group is assembling a dedicated group IV MBE chamber attached to the cluster tool. Superconductors Pb and Sn are group IV materials are promising candidates for induced superconductivity in these nanowires.

8.2.2 *Future topological quantum devices*

If Majoranas can be manipulated and their final states can measured in well controlled experiments, this could pave the way towards the realization of a topological quantum computer.[14] The bottom-up growth approach reported in this thesis offers high quality quantum nanowires optimal for development of prototype devices where quantum phenomena can be demonstrated. A major challenge for devices that are based on bottom-up grown nanowires is scalability. A topological quantum computer device chip requires a large number of high-quality nanowires in close proximity and predefined positions integrated on a single chip. The current device fabrication process includes a step where the quantum nanowires are transferred using a manipulator in SEM or optical microscope.

Recently, a novel approach to the growth of scalable InAs and InSb one-dimensional quantum devices is demonstrated.[15-19] The scalability issues were overcome by developing selective area growth of in-plane nanowires and nanowire networks on semi-insulating substrates. Challenges here are the crystal quality and purity that is limited by the substrate and the possibility to implement the required number of local gates for the realization of complex many-qubit devices. To increase the

scalability potential one may develop a substrate with an integrated buffer layer and bottom gates. This would allow to build a device with a three-dimensional integrated gate configuration, which enables better electrostatic control and a higher device density.

The scope of future experiments combines understanding the properties and physics of the new materials suggested above followed by their implementation in novel complex integrated schemes in substrates that can be fabricated in scalable automated fashion.

8.3 References

1   Liu, C.-X., Sau, J. D. & Das Sarma, S. Role of dissipation in realistic Majorana nanowires. *Physical Review B* **95**, 054502, doi:10.1103/PhysRevB.95.054502 (2017).

2   Springholz, G., Bauer, G. & Ihninger, G. MBE of high mobility PbTe films and PbTe/Pb1-xEuxTe heterostructures. *Journal of Crystal Growth* **127**, 302-307, doi:https://doi.org/10.1016/0022-0248(93)90626-8 (1993).

3   Schaber, H. & Doezema, R. E. Far-infrared spin—flip resonance in PbTe. *Solid State Communications* **31**, 197-199, doi:https://doi.org/10.1016/0038-1098(79)90434-4 (1979).

4   Fardy, M., Hochbaum, A. I., Goldberger, J., Zhang, M. M. & Yang, P. Synthesis and Thermoelectrical Characterization of Lead Chalcogenide Nanowires. *Advanced Materials* **19**, 3047-3051, doi:10.1002/adma.200602674 (2007).

5   Tai, G. a., Zhou, B. & Guo, W. Structural Characterization and Thermoelectric Transport Properties of Uniform Single-Crystalline Lead Telluride Nanowires. *The Journal of Physical Chemistry C* **112**, 11314-11318, doi:10.1021/jp8041318 (2008).

6   Yang, Y. *et al.* Synthesis of PbTe Nanowire Arrays using Lithographically Patterned Nanowire Electrodeposition. *Nano Letters* **8**, 2447-2451, doi:10.1021/nl801442c (2008).

7   Dziawa, P. *et al.* Defect Free PbTe Nanowires Grown by Molecular Beam Epitaxy on GaAs(111)B Substrates. *Crystal Growth & Design* **10**, 109-113, doi:10.1021/cg900575r (2010).

8   Volobuev, V. V. *et al.* Bi catalyzed VLS growth of PbTe (001) nanowires. *Journal of Crystal Growth* **318**, 1105-1108, doi:https://doi.org/10.1016/j.jcrysgro.2010.11.143 (2011).

9   Higginbotham, A. P. *et al.* Hole Spin Coherence in a Ge/Si Heterostructure Nanowire. *Nano Letters* **14**, 3582-3586, doi:10.1021/nl501242b (2014).

10   Kloeffel, C., Trif, M. & Loss, D. Strong spin-orbit interaction and helical hole states in Ge/Si nanowires. *Physical Review B* **84**, 195314, doi:10.1103/PhysRevB.84.195314 (2011).

11   Maier, F., Kloeffel, C. & Loss, D. Tunable g-factor and phonon-mediated hole spin relaxation in Ge/Si nanowire quantum dots. *Physical Review B* **87**, 161305, doi:10.1103/PhysRevB.87.161305 (2013).

12   Brauns, M., Ridderbos, J., Li, A., Bakkers, E. P. A. M. & Zwanenburg, F. A. Electric-field dependent g-factor anisotropy in Ge-Si core-shell nanowire quantum dots. *Physical Review B* **93**, 121408, doi:10.1103/PhysRevB.93.121408 (2016).

13   Conesa-Boj, S. *et al.* Boosting Hole Mobility in Coherently Strained [110]-Oriented Ge-Si Core-Shell Nanowires. *Nano letters* **17**, 2259-2264, doi:10.1021/acs.nanolett.6b04891 (2017).

14   Sarma, S. D., Freedman, M. & Nayak, C. Majorana zero modes and topological quantum computation. *Npj Quantum Information* **1**, 15001, doi:10.1038/npjqi.2015.1 (2015).

15   Vaitiekėnas, S. *et al.* Selective-Area-Grown Semiconductor-Superconductor Hybrids: A Basis for Topological Networks. *Physical Review Letters* **121**, 147701, doi:10.1103/PhysRevLett.121.147701 (2018).

16   Aseev, P. *et al.* Selectivity Map for Molecular Beam Epitaxy of Advanced III–V Quantum Nanowire Networks. *Nano Letters* **19**, 218-227, doi:10.1021/acs.nanolett.8b03733 (2019).

17   Krizek, F. *et al.* Field effect enhancement in buffered quantum nanowire networks. *Physical Review Materials* **2**, 093401, doi:10.1103/PhysRevMaterials.2.093401 (2018).

18   Friedl, M. *et al.* Template-Assisted Scalable Nanowire Networks. *Nano Letters* **18**, 2666-2671, doi:10.1021/acs.nanolett.8b00554 (2018).

19   Op het Veld, R. *et al.* In-plane selective area nanowire networks. *In preparation* (2019).

8

Summary

Summary

This thesis reports the progress of bottom-up growth of quantum materials based on semiconductor indium antimonide (InSb) nanowires towards the realization of a topological quantum computer. Since scientists from the Kavli Institute of Nanoscience Delft and Eindhoven University of Technology reported in 2012 the first observations of the mysterious Majorana quasiparticles in superconductor/nanowire devices the search for Majoranas in condensed matter has become one of the hottest topics in physics.

Chapter 1 introduces the concept of quantum computation and topological quantum computation with the key ingredient being a one-dimensional quantum nanowire that can host non-Abelian quasiparticles known as Majorana quasiparticles. In Chapter 2 a brief theoretical background to the Majorana experiments and quantum nanowire growth methods are given. Chapter 3 discusses the methods of crystal growth, materials characterization, quantum device fabrication and measurement techniques enabling the experiments in this dissertation.

In Chapter 4 and Chapter 5, a new approach in crystal growth is demonstrated, which enables to grow complete quantum devices from the bottom-up. InSb nanowires are grown from arrays of gold nanoparticles patterned on specially designed indium phosphide (InP) substrates using the vapor-liquid-solid method on InP stems in a metal-organic vapor phase epitaxy reactor. These devices directly address the two main challenges in this field of research. First of all, an accurate control over the nanowire position and growth direction enables the growth of complicated networks of up to four crossed junctions, such as closed loops of four interconnected nanowires (referred to as "hashtags"). These structures are single crystalline nanowire loops and exhibit coherent transport over long length scales demonstrated by an Aharonov-Bohm experiment. Integrated with superconductors these loops can be used for first Majorana braiding experiments. Secondly, due to the *in-situ* integration of superconductor with semiconductor materials, unprecedented device quality has been obtained. As a direct consequence of the improved interface quality, a hard-superconducting gap has been observed in these devices. The observation of a quantized conductance plateau strongly supports the existence of Majorana zero-modes, paving the way for future braiding experiments that could lead to topological quantum computing.

Furthermore, in Chapter 6 we investigate the growth of stem-free InSb nanowires. Using a selective-area mask in combination with gold as a catalyst allows us to completely omit the stem, thus demonstrating that nanowires can grow directly from the substrate. By this means, ultra-pure high aspect ratio nanowire are grown. The chemical purity of these nanowires by omission of the stem was investigated by atom probe tomography. The field electron mobility measurements show enhanced record electron mobility in contrast to InSb nanowires grown on stems.

Chapter 7 outlines another way towards providing design flexibility and enabling growth of superior devices by relying on "free-standing" two-dimensional systems. The epitaxial growth of InSb nanoflakes on an InSb substrate platform is performed with a nearly 100% yield of these nanostructures.

This dissertation is concluded with Chapter 8 which discusses the outlook and future directions for realizing an ideal material system for topological quantum computation.

Acknowledgments

Acknowledgments

I still cannot believe that the four years have passed and that I am writing the most difficult part of my thesis "the acknowledgments". It is challenging to put down the words that should describe these years since my experience during the PhD has been nothing short of amazing. I have been given unique opportunities and challenges and I have taken advantage of them. The work presented in this dissertation is the result of a team work and different collaborations and it could not have been done without united passion for the research and the hard work and support of many people.

First and foremost I wish to thank my supervisor Erik Bakkers. You have been supportive since the day one. I remember very well my first cleanroom days and growths. I used to come by your office multiple times per day to inform you about the amazing InSb growth. I know I can talk a lot… And since I am aware of it I would like to thank you for your time, patient listening, engaging in the conversation and for the constructive feedback. I always left your office feeling more confident and inspired about our work. You are a brilliant supervisor, scientist and the most optimistic and positive person. Without your guidance I would not be the same person I am today.

My work could not be carried out without the collaboration with the group of Leo Kouwenhoven. Leo, I am pleased to have you as my co-promoter. Furthermore, I want to thank members of your group: Stijn Balk, Hao Zhang, Di Xu, Michiel de Moor, Jie Shen and Fokko de Vries for the effortless work and transport measurements on my nanostructures.

Another vital collaboration for my research was with Chris Palmstrøm's group. Thank you Chris for letting me come to your lab on the beautiful coast of Santa Barbara. I enjoyed the work, nature and shopping (I must admit). I admire your passion for the work in the lab and I have learned a lot from you about MBE and crystal growth. Special thanks goes to Jay Logan, Joon Sue Lee and Mihir Pendharkar from your lab.

I would like to acknowledge my colleagues and friends at TU/e.
Many of you left a year or two after I started my PhD at TU/e: Alessandro Cavalli, Diana Car, Dick van Dam, Ikaros Hauge and Simone Assali. Thanks for all the joy in the office and for allowing me to feed you. I am deeply grateful to Simone who has been my source of inspiration in the first year of my PhD. Your passion and excellent feeling for the growth motivated me to explore beyond limits of InSb growth.

The best memories I have with the group members that I shared with my last years of my PhD: Alain Dijkstra, Daniel Vakulov, Elham Fadaly, Ghada Badawy, Ilya

Kolpakov, Jason Jung, Jim Quik, Ksenia Korzun, Luca Gagliano, Max Hoskam, Marco Rossi, Philipp Leubner, Roy Op het Veld, Sander Schellingerhout, Sebastian Kölling, Yizhen Ren, Qing Zhao. Thank you guys for letting me take you to Bosnia. I am so happy that I have been given the opportunity to share my culture, wonderful group outings, dinners and tough hours in the sports center with you.

Roy and Ghada, my PhD brother and sister. I appreciated to get to know you and work with you. We are such a good team! We were the three musketeers of quantum materials. Roy, maybe you do not know it, but I learned so much from you. Thanks for making our life much easier with your excellent problem solving and optimization skills. Ghada, you are so sweet and kind. I enjoyed to work with you more than you can imagine. You were an excellent colleague you can count on with any issue and you kindly offered your support whenever you felt that I needed it. Thank you guys!

Philipp, you were the best MBE postdoc and essential to our group. Thanks for staying at TU/e with us and for being so eager to help me with everything. I have learned a lot from you and enjoyed skating and sporting together. Thanks for reading and correcting this thesis. Good luck with your new career and life in Munich, you will do amazing and I will come to visit.

I am also grateful to Sebastian for the challenging FIB and APT experiments and constant complains about fancy cars and highway speed limits.

Sander and Marco, I was fortunate to be your master thesis supervisor and I enjoyed our months together. I am super happy that you decided to continue with PhD in our group.

TEM analysis is a large part of the work in this thesis. Marcel Verheijen you spent infinite amounts of time analyzing my samples. I am grateful for your patience and for allowing me to join your TEM sessions. I will never forget our karaoke evening in Bosnia when you made me "think to myself what a wonderful world". I am also deeply thankful that you invested your time to give me comments on the Chapter 3 of this thesis.

Jos Haverkort, thank you for letting me teach your course at TU/e, it was fun. Although I did not directly work with you, I am glad that you joined the "Bosnia trip" where I got to know you better and learned to appreciate the kind person that you are. Thanks for encouraging me to finish-up my thesis on time.

This cleanroom-heavy dissertation could not have been completed if there were no NanoLab@TU/e staff members that did a great job: Barry Smalbrugge, Erik Jan Geluk, Frank van Otten, René van Veldhoven.

Barry, I am very very grateful that you did not give me a fine when doing "illegal stuff" with chemicals. Frank, thanks for the MBE introduction in my first year of PhD. I am so lucky that I did not break anything. René, or may I say P. J., your knowledge on MOVPE was essential to my research. You did not only keep MOVPE

List of publications

List of publications

* Equal contributions*

High mobility stemless InSb nanowires
Ghada Badawy*, **Sasa Gazibegovic***, Sebastian Heedt, Francesco Borsoi, Sebastian Koelling, Marcel A. Verheijen, Leo P. Kouwenhoven, and Erik P. A. M. Bakkers
In review by Nano Letters, (2019)

Bottom-up grown two-dimensional InSb nanostructures
Sasa Gazibegovic*, Ghada Badawy*, Thijs L.J. Buckers, Philipp Leubner, Jie Shen, Folkert K. de Vries, Sebastian Koelling, Leo P. Kouwenhoven, Marcel A. Verheijen, Erik P.A.M. Bakkers. **Advanced Materials** 1808181, (2019)

Quantized Majorana conductance
Hao Zhang*, Chun-Xiao Liu*, **Sasa Gazibegovic***, Di Xu, John A. Logan, Guanzhong Wang, Nick van Loo, Jouri D. S. Bommer, Michiel W. A. de Moor, Diana Car, Roy L. M. Op het Veld, Petrus J. van Veldhoven, Sebastian Koelling, Marcel A. Verheijen, Mihir Pendharkar, Daniel J. Pennachio, Borzoyeh Shojaei, Joon Sue Lee, Chris J. Palmstrøm, Erik P. A. M. Bakkers, S. Das Sarma, and Leo P. Kouwenhoven. **Nature** 556, 74 (2018)

Epitaxy of advanced nanowire quantum devices
Sasa Gazibegovic*, Diana Car*, Hao Zhang*, Stijn C. Balk, John A. Logan, Michiel W. A. de Moor, Maja C. Cassidy, Rudi Schmits, Di Xu, Guanzhong Wang, Peter Krogstrup, Roy L. M. Op het Veld, Kun Zuo, Yoram Vos, Jie Shen, Daniël Bouman, Borzoyeh Shojaei, Daniel Pennachio, Joon Sue Lee, Petrus J. van Veldhoven, Sebastian Koelling, Marcel A. Verheijen, Leo P. Kouwenhoven, Chris J. Palmstrøm, and Erik P. A. M. Bakkers. **Nature** 548, 434 (2017)

Parity transitions in the superconducting ground state of hybrid InSb–Al Coulomb islands
Jie Shen, Sebastian Heedt, Francesco Borsoi, Bernard van Heck, **Sasa Gazibegovic**, Roy L. M. Op het Veld, Diana Car, John A. Logan, Mihir Pendharkar, Senja J. J. Ramakers, Guanzhong Wang, Di Xu, Daniël Bouman, Attila Geresdi, Chris J. Palmstrøm, Erik P. A. M. Bakkers, and Leo P. Kouwenhoven. **Nature Communications** 9, 4801 (2018)

Electric field tunable superconductor-semiconductor coupling in Majorana nanowires
Michiel W.A. de Moor, Jouri D.S Bommer, Di Xu, Georg W. Winkler, Andrey E. Antipov, Arno Bargerbos, Guanzhong Wang, Nick Van Loo, Roy L.M. op het Veld, **Sasa Gazibegovic**, Diana Car, John A. Logan, Mihir Pendharkar, Joon Sue Lee, Erik P.A.M. Bakkers, Chris J. Palmstrøm, Roman M. Lutchyn, Leo P. Kouwenhoven, Hao Zhang. **New Journal of Physics** 20 (10), 103049 (2018)

Selective-area superconductor epitaxy to ballistic semiconductor nanowires
Stephen T. Gill, Jeff Damasco, Blanka E. Janicek, Malcolm S. Durkin, Vincent Humbert, **Sasa Gazibegovic**, Diana Car, Erik P.A.M. Bakkers, Pinshane Y. Huang, and Nadya Mason. **Nano Letters** 18 (10), 6121 (2018)

Atmospheric plasma-enhanced spatial-ALD of lnZnO for high mobility thin film transistors
Andrea Illiberi, Ilias Katsouras, **Sasa Gazibegovic**, Brian Cobb, Elida Nekovic, Willem van Boekel, Corne Frijters, Joris Maas, Fred Roozeboom, Yves Creyghton, Paul Poodt, and Gerwin Gelinck. **Journal of Vacuum Science and Technology. A: Vacuum, Surfaces, and Films** 36, 04F401 (2018)

Mirage Andreev spectra generated by mesoscopic leads in nanowire quantum dots
Zhaoen Su, Azarin Zarassi, Jen Feng Hsu, Pablo San-Jose, Elsa Prada, Ramon Aguado, Eduardo J. H. Lee, **Sasa Gazibegovic**, Roy L. M. Op het Veld, Diana Car, Sebastien R. Plissard, Moira Hocevar, Mihir Pendharkar, Joon Sue Lee, John A. Logan, Chris J. Palmstrøm, Erik P. A. M. Bakkers, and Sergey M. Frolov. **Physical Review Letters** 121, 127705 (2018)

Atom-by-atom analysis of semiconductor nanowires with parts per million sensitivity
Sebastian Koelling, Ang Li, Alessandro Cavalli, Simone Assali, Diana Car, **Sasa Gazibegovic**, Erik P. A. M. Bakkers, and Paul M. Koenraad. **Nano Letters** 17 (2), 599 (2017)

About the author

Saša Gazibegović was born on 02-07-1990 in Doboj, Bosnia and Herzegovina. After finishing Gymnasium high school in 2009 at Mustafa Kamarić high school in Gračanica (Bosnia and Herzegovina) she studied Applied Physics at Faculty of Science - University of Sarajevo (Bosnia and Herzegovina). She did her Master thesis project in TNO/Holst Centre, Eindhoven (Netherlands) on the growth of InZnO thin films for thin film transistor application and graduated in November 2014. From February 2015 she started a PhD project at Technical Universities of Delft and Eindhoven (Netherlands) of which the results are presented in this dissertation. Since 2015 she is employed at Delft University of Technology. She obtained the scholarship from the Center municipality of Sarajevo city for the academic year 2012-2013. She obtained the Raith Micrograph Award in 2017.